CONSTANZE KALCHER

CREEP OF Cu–Zr METALLIC GLASSES AND METALLIC GLASS COMPOSITES: A MOLECULAR DYNAMICS STUDY

Zur Erlangung des akademischen Grades Doktor-Ingenieur (Dr.-Ing.)
genehmigte Dissertation vorgelegt
von M. Sc. Constanze Kalcher
geboren in Gießen

Fachgebiet Materialmodellierung
Fachbereich Material- und Geowissenschaften
Technische Universität Darmstadt

Referent: Prof. Dr. Karsten Albe,
Technische Universität Darmstadt

Korreferent: Prof. Dr. Erik Bitzek,
Friedrich-Alexander Universität Erlangen-Nürnberg

Tag der Einreichung: 10. Oktober 2018
Tag der Prüfung: 3. Dezember 2018

D17 – Darmstadt 2019

Kalcher, Constanze: Creep in Cu–Zr metallic glasses and metallic glass composites:
A molecular dynamics study
Darmstadt, Technische Universität Darmstadt,
Jahr der Veröffentlichung der Dissertation auf TUprints: 2019
URN: urn:nbn:de:tuda-tuprints-86102
Tag der mündlichen Prüfung: 03.12.2018

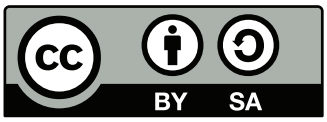

CREEP OF Cu–Zr METALLIC GLASSES AND METALLIC GLASS COMPOSITES: A MOLECULAR DYNAMICS STUDY

CONSTANZE KALCHER

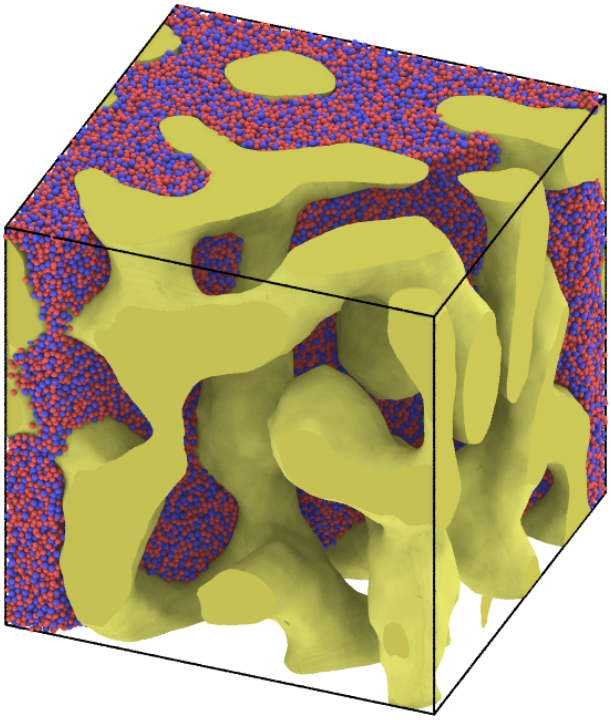

Dissertation

2018

On the cover: Metallic glass–crystal composite model studied in this thesis where the crystalline phase has the shape of an interpenetrating network.

CONTENTS

LIST OF FIGURES

LIST OF ABBREVIATIONS

BMGs	bulk metallic glasses
CNA	common neighbor analysis
CSRO	chemical short range order
FI	full icosahedral
GUMS	geometrically unfavored motifs
ISO	icosahedral short range order
MC	Monte-Carlo
MD	molecular dynamics
MG	metallic glass
NG	nanoglass
PEL	potential energy landscape
RDF	radial distribution function
SCL	super-cooled liquid
STZs	shear transformation zones
VFT	Vogel-Fulcher-Tamann

ABSTRACT

Creep is the time-dependent deformation of a material at elevated temperature and under stress-conditions below yield. This slow, time-delayed deformation can ultimately lead to the failure of an engineering component, especially in high-temperature applications. But even well before material failure, the elongation of an engineering component, e.g. a turbine blade, during service life can have catastrophic consequences. Thus, knowledge of the mechanism of creep deformation is of utmost importance for choosing a material for a specific engineering application.

While the phenomenon of creep is already well understood in metals and a large body of work exists on how to improve their creep resistance, this behavior is not exclusive to crystalline materials. Partly crystalline materials such as polymers and ceramics and even glasses can exhibit significant creep deformation as well. For the conventional soda-lime glass the possibility of creep seems irrelevant in its typical application window, but with the development of new glassy materials, such as metallic glasses, that are amorphous metals quenched from the melt and potential candidates for a wide application range of temperatures and stresses, the assessment of the creep behavior of amorphous materials has been taken beyond purely scientific interest.

In this thesis molecular dynamics simulations are used to understand the creep behavior of a homogeneous $Cu_{64}Zr_{36}$ metallic glass as well as glass-crystal composites. First, we treat the case of the homogeneous glass, and establish the temperature and stress parameter range necessary to observe creep in molecular dynamics simulations. Second, we will study the influence of the glass-crystal interface properties on the creep rates. The latter also critically depends on how realistic the computer composite model is. Third, we study a different microstructure of amorphous-crystalline composites which belong to the nanoglass family. We show how the glassy grain-boundary phase present in a nanoglass can be altered to have a reinforcing effect, both in the low temperature regime and under creep conditions.

ZUSAMMENFASSUNG

Unter Kriechen versteht man die zeitabhängige Verformung eines Materials bei erhöhter Temperatur und bei Spannungsbedingungen unterhalb der Streckgrenze. Diese langsame, zeitverzögerte Verformung kann insbesondere bei Hochtemperaturanwendungen zum letztendlichen Ausfall eines technischen Bauteils führen. Doch bereits vor dem Materialversagen kann die Dehnung eines technischen Bauteils im

Betrieb, z.B. einer Turbinenschaufel, katastrophale Folgen haben. Für die Auswahl eines geeigneten Werkstoffes ist die Kenntnis des Mechanismus der Kriechverformung daher von großer Bedeutung.

Für Metalle sind das Phänomen des Kriechens und Methoden zur Steigerung der Kriechfestigkeit größtenteils verstanden. Jedoch ist dieses Verhalten keineswegs auf kristalline Materialien beschränkt. Auch Polymere und Keramiken, die eine teilkristalline Struktur besitzen, sowie Gläser können signifikante Kriechverformungen aufweisen. Für das herkömmliche Kalk-Natron-Glas erscheint die Möglichkeit des Kriechens in seinem typischen Anwendungsfenster irrelevant. Mit der Entwicklung neuer glasartiger Materialien allerdings ist die Beurteilung des Kriechverhaltens von amorphen Werkstoffen nicht mehr zu vernachlässigen. Ein Beispiel sind metallische Gläser. Diese aus der Schmelze abgeschreckten amorphen Metalle sind potentielle Kandidaten für Anwendungen in einem breiten Temperatur- und Spannungsbereich.

In dieser Arbeit werden Molekulardynamik Simulationen verwendet, um das Kriechverhalten eines homogenen metallischen $Cu_{64}Zr_{36}$ Glases sowie von Glas-Kristall Kompositen zu verstehen. Zuerst wird der Fall des homogenen Glases betrachtet, um die Temperatur- und Spannungsparameter zu bestimmen die für das Beobachten von Kriechen in molekulardynamischen Simulationen nötig sind. Zweitens wird der Einfluss der Glas-Kristall-Grenzflächeneigenschaften auf das Kriechverhalten, d.h. auf die Kriechraten der Komposite, untersucht. Letzteres hängt auch entscheidend davon ab, wie realitätsnah das Komposit-Computermodell ist. Drittens wird eine weitere Mikrostruktur von amorph-kristallinen Verbundwerkstoffen behandelt, die zur Nanoglasfamilie gehört. Es wird gezeigt, dass die im Nanoglas vorhandene amorphe Korngrenzphase so verändert werden kann, dass eine verstärkende Wirkung sowohl im Tieftemperaturbereich als auch unter Kriechbedingungen erzielt wird.

Part I

INTRODUCTION

1

METALLIC GLASSES

Metallic glasses (MGs) are amorphous metallic alloys that are rapidly quenched from the melt such that crystallization is kinetically hindered. The discovery of this relatively new material class in 1960[1] has been met with much excitement because of its members' excellent mechanical properties, i.e. high strength and elastic moduli.[2–4] However, the prospect of MGs being used as structural materials faded quickly, because of their brittle failure mechanism carried by strongly localized shear bands. To date, overcoming the limited ductility of MGs remains a central research objective. Different strategies have been pursued to address the problem of brittleness, which typically involve inhomogeneous methods such as composite formation by introducing secondary phases[5–9] or homogeneous methods such as thermal or mechanical pretreatment.[10–13] Many of these attempts have been successful in improving the ductility under conventional loading conditions at moderate temperatures, but the deformation behavior outside this range did not receive much attention yet. This thesis aims to extend our understanding of the impact of long-time stress exposure at elevated temperatures, i.e. effectively creep conditions, on the mechanical properties of MGs and their derivates, such as glass–crystal composites and so-called nanoglasses. Hence, before explaining the fundamentals of creep deformation in Ch. 2, we will devote the following chapter to a short introduction into the topic of MGs.

1.1 THE GLASS TRANSITION

In principle not much different from conventional soda-lime glasses, MGs are produced by fast quenching from the melt such that an under-cooled liquid is obtained and crystallization is suppressed.* Given a high enough cooling rate to bypass the thermodynamic melting temperature T_M a so called super-cooled liquid (SCL) state can be achieved. Upon further cooling the SCL is vitrified, i.e. "frozen" into a glassy state. The temperature, at which the glass starts to deviate from the equilibrium SCL is called the glass transition temperature T_g.[15] Figure 1(a) schematically compares how volume and entropy evolve with temperature during crystallization and undercooling. In the case of crystallization a discontinuity in the volume/entropy

* Additive manufacturing methods like direct metal laser sintering only recently allowed the successful synthesis of a Fe-based bulk metallic glass with dimensions more than 15 times larger than its casting thickness.[14]

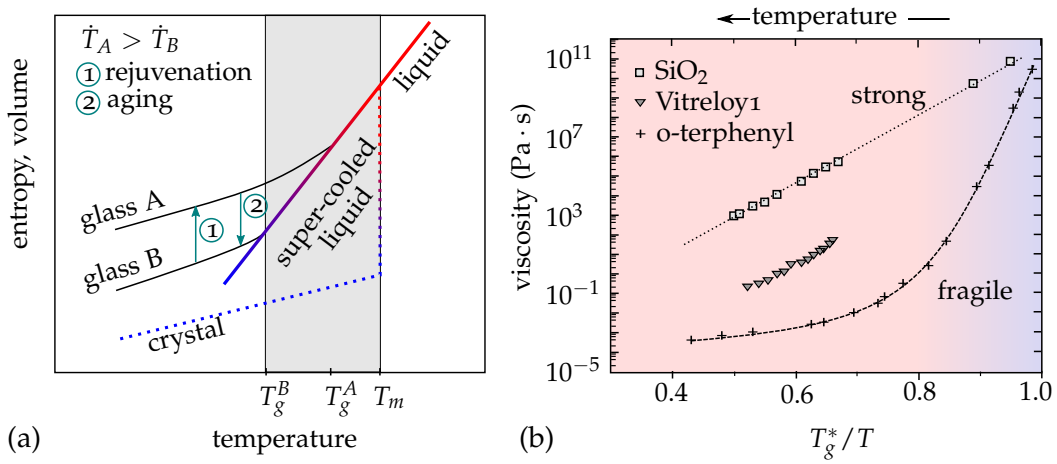

FIGURE 1: (a) Dependence of entropy and volume on temperature during crystallization and glass transition. While crystallization exhibits a discontinuity at the melting temperature T_M, which is characteristic for a thermodynamic phase transition of first order, the glass transition depends on the cooling rate $\dot{T}$. On long timescales glasses can undergo further relaxation towards the SCL, even below T_g. This is indicated by the green arrow ①. The reverse process ② is called rejuvenation and is discussed in section 1.2. (b) Angell plot: Viscosity evolution with temperature for strong and fragile glass formers. Data reproduced from Ref. 16.

curve occurs at T_M, when the latent heat is released, which is a typical feature of a first order thermodynamic phase transition. The glass transition, on the other hand, is not a true thermodynamic phase transition, since T_g depends on the cooling rate. Nonetheless, a broad peak in the temperature dependence of the heat capacity gives a good estimate of the glass transition temperature, just like for a second order phase transition.

From a technological viewpoint not only T_g but also the cooling rates necessary to achieve a sufficient undercooling are important key factors: A breakthrough in the MG production was achieved when multicomponent systems were found that allowed to reduce the required cooling rates by several orders of magnitudes from $\dot{T} = 10^6\,\mathrm{K/s}$ down to $100\,\mathrm{K/s}$ and thus the realization of geometries exceeding the millimeter range, so-called bulk metallic glasses (BMGs).[3,17,18] Ideal compositions are often eutectics, to keep T_g as low as possible. Commercially available MGs, such as the so-called Vitreoloy1™ ($Zr_{41.2}Ti_{13.8}Cu_{12.5}Ni_{10}Be_{22.5}$) require even lower cooling rates on the order of $1\,\mathrm{K/s}$.[19,20] In atomistic simulations, the physics of highly alloyed systems is more difficult to capture with interatomic potentials. For that reason, the binary Cu–Zr system, especially the $Cu_{64}Zr_{36}$ glass former, is a popular object of study[21–25] and will be described further in section 1.4.

Different theoretical frameworks for characterizing the glass transition have been established and will be explained in the following. In its simplest definition, the glass transition temperature is the temperature where the viscosity of the melt

exceeds the value of 10^{12} Pa · s.[26] The temperature dependence of the viscosity is often described by the Vogel-Fulcher-Tamann (VFT) law:[15,26,27]

$$\eta = \eta_0 \times \exp\left(\frac{D^* \cdot T_0}{T - T_0}\right), \tag{1.1}$$

where D^* is the kinetic fragility of the liquid[28,29] and describes the deviation from Arrhenius behavior. In that way, glasses are categorized as "strong" or "fragile" glass formers. The behavior of strong and fragile glass formers when approaching the glass transition temperature is depicted in the Angell-plot in Figure 1(b). BMGs usually exhibit kinetic fragilities $13 \leq D^* \leq 26$ and thus lie in the middle between the strong glass former SiO_2 ($D^* \approx 100$) and fragile polymeric glasses ($D^* \approx 2$).[16,30] These fragility parameters are usually obtained from viscosity measurements in the supercooled liquid state or by three-point beam bending tests at very small undercoolings.[16,27,31] Recently, Busch *et al*. have shown that VTF fits of the viscosity performed on the same system yield different fragility parameters D^* for data obtained far away or in the vicinity of T_g, see Ref. 31. The authors argue that this crossover from a fragile to strong liquid is indicative for a liquid-liquid phase transition of the supercooled liquid. Moreover, such an "isothermal phase transition"[27] has also been suspected at temperatures well below T_g and is connected to the phenomenon of physical aging presented in the next section.

Another widely embraced concept to describe the glass transition is the potential energy landscape (PEL),[32–35] which can be understood as the configurational phase space accessible to the MG. In general, the PEL of a MG is organized into larger megabasins composed of smaller sub-basins. The MG can access these energy basins by two different relaxation processes, so-called α- and β-relaxations.[32] Whereas the α-relaxations are associated with megabasin jumps and usually freeze below the glass transition temperature, the β-relaxations occur in sub-basins and continue even below T_g.[36,37] Dependent on the processing, e.g. the cooling rates, the final MG can thus end up in one of many isoconfigurational sub-basins, which explains that glasses processed in the same way can exhibit different properties.

The free volume model proposed by Turnbull and Cohen[38,39] states that atomic diffusion is possible only when the free volume in the vicinity of the atom surpasses a critical value. The model has been found unsuitable for describing the glass transition of MGs.[40,41] It also cannot reproduce low temperature structural relaxation.[42] However, the general trend, that the free volume is decreasing upon glass formation, is commonly accepted.[42] Moreover, more slowly quenched glasses, that are better relaxed, do generally exhibit less free volume.

1.2 AGING AND REJUVENATION

Metallic glasses are thermodynamically metastable and thus it comes at no surprise that certain properties, e.g. their enthalpy, viscosity and density, still show a time-dependence at temperatures far below T_g.[31,43–45] Depending on the direction of that evolution, the process is either called *physical aging* or *rejuvenation*. The time-scales

necessary to observe a change in properties increase strongly with decreasing temperatures, though, and often exceed laboratory time-scales. The difference between aging and rejuvenation can be understood in terms of decreasing or increasing enthalpy, or by again employing the picture of the PEL: During aging, the glass relaxes towards a lower potential energy configuration and is deeply trapped in its current sub-basin. Rejuvenation, in contrast, allows for a higher potential energy level to be reached.[45]

The problem of physical aging in glasses has already been treated in the context of polymer glasses more than 40 years ago,[46] since in these materials relaxation processes are relevant even at room temperature and lead to declining mechanical properties. In MGs aging causes embrittlement.[10,47–49] Gallino and Busch have described physical aging as process, where the glass can undergo an "isothermal" phase transition into a more relaxed glass state, closer to the equilibrium liquid.[27] In Figure 1(a) this is indicated by path ②. Aging or relaxation can occur in different temperature regimes. In the SCL state (between T_M and T_g) and down to temperatures in the vicinity of T_g the (isothermal) response to a perturbation is often described by the phenomenological Kohlrausch-William-Watts equation

$$\phi(t) = \phi_0 \exp\left[-\left(\frac{t}{\tau}\right)^{\beta^{\mathrm{KWW}}}\right], \tag{1.2}$$

where τ is the characteristic relaxation time, β^{KWW} the stretching exponent ($0 < \beta^{\mathrm{KWW}} < 1$) and $\phi(t)$ stands for materials properties like the viscosity, enthalpy or the energy. Furthermore, the diffusion trap model proposed by Philips links the β^{KWW} exponents to different microscopic processes and predicts $\beta^{\mathrm{KWW}} = 3/7$ for long-range and $\beta^{\mathrm{KWW}} = 3/5$ for short-range interactions.[50] The model prediction for β^{KWW} seems to fit well for various relaxation behaviors of network glasses,[51–53] but less so for MG's.[54–56] For temperatures far below T_g the applicability of Eq. 1.2 is still under debate. Zhu *et al*. were able to correlate the dynamics of β-relaxations and spatial heterogeneities during sub-T_g relaxation annealing of a Zr-based MG film between $0.68T_g$ and $0.8T_g$ using differential scanning calorimetry and amplitude-modulation atomic force microscopy.[57] They found that during annealing the β-relaxations slow down as the structural heterogeneities degenerate. Both processes exhibited KWW-behavior with very similar relaxation times τ and activation energies.[57] In contrast, Gallino *et al*. measured the enthalpy decay during aging of a AuCuSiAgPd BMG and found that the decay is better described by a sum of exponential decays rather than a stretched exponential.[55] These results suggests that the properties of the SCL state cannot directly be transferred to the glassy state to explain relaxation phenomena below T_g and we will further discuss this issue in the context of creep in Ch. 2.

In contrast to aging, rejuvenation is accompanied by an improvement of the mechanical properties, e.g., the ductility.[10,58,59] Several processing routes have proven successful at achieving structural rejuvenation in MGs: The obvious one is by annealing the glass above T_g in order to erase the memory of the previous thermal history, followed by quenching down to the glass state again. Saida *et al*. have calcu-

lated a rejuvenation map in terms of annealing temperature and quenching rate by means of MD-simulations of $Cu_{64}Zr_{36}$. It shows that the rejuvenation behavior of $Cu_{64}Zr_{36}$ is controlled by both the annealing temperature (ideally $\geq 1.2T_g$) and the subsequent cooling rate.[60] The authors pointed out though, that during annealing under laboratory conditions, crystallization is very likely to occur as a competing mechanism, especially at these elevated temperatures. Alternatively, sub-T_g rejuvenation of MGs has been achieved by ion irradiation,[58] shoot-peening,[61] inhomogeneous plastic deformation through high-pressure torsion[62] or homogeneous plastic deformation through uniaxial compressive deformation.[11,63] In the interest of practical applicability, however, less destructive methods would be preferable to tune the structural state of a MG. This has been realized recently in a Zr-based BMG through causing non-affine thermal strains by means of low-temperature thermal cycling between RT and 77 K.[13] Rejuvenation through low temperature cycling was, however, only possible when the sample had not been fully relaxed by annealing first. The authors promote the idea that rejuvenation introduces heterogeneities in the glass, so-called soft-spots,[12] which help to initiate flow and thus improve ductility. Conversely, the introduction of more heterogeneities is easier in less relaxed, i.e. less homogeneous glasses. Interestingly, there is evidence that applying a strain within the elastic limit and below T_g (which corresponds to creep conditions) can have a rejuvenating effect as well.[10,59] Such an isothermal, sub-T_g rejuvenation is schematically shown in Figure 1 as path ①, and will be treated in more detail in Ch. 2 and Ch. 5.

1.3 DEFORMATION BEHAVIOR OF THE HOMOGENEOUS GLASS

Classically, three different deformation regimes in terms of stress, temperature and strain rate are distinguished:[2,64] elastic deformation, homogeneous plastic deformation at high temperatures and low stresses, and heterogeneous plastic deformation (shear banding) at low temperatures and high stresses. All plastic deformation is carried by shear transformation zones (STZs),[2,40,65–67] only their localization is different. STZs are viewed as groups of a few atoms that experience discrete shear events, which are associated with activation energies typically on the order of 1 eV.[68,69]

The assumption that STZs trigger surrounding STZs in a cascade like manner and eventually combine to form shear bands stands to reason.[35,70–72] Shear band nucleation is then associated with the onset of yielding.[73] However, the proper atomistic mechanism behind shear band nucleation and propagation still remains elusive. Recently, Şopu *et al*. have shown using MD-simulations that STZ percolation involves the formation of strong rotation fields, so-called vortexes, that bridge and hence activate neighboring STZs.[74]

Although depicted as solid line in Figure 2, the transition between the elastic and the inelastic regime is not clear-cut. Schuh noted that there should be no regime where thermally activated homogeneous flow could be avoided, but suggested to neglect it at strain rates below $\dot{\epsilon} = 10^{-12}\,s^{-1}$.[2] In this work, we will reexamine

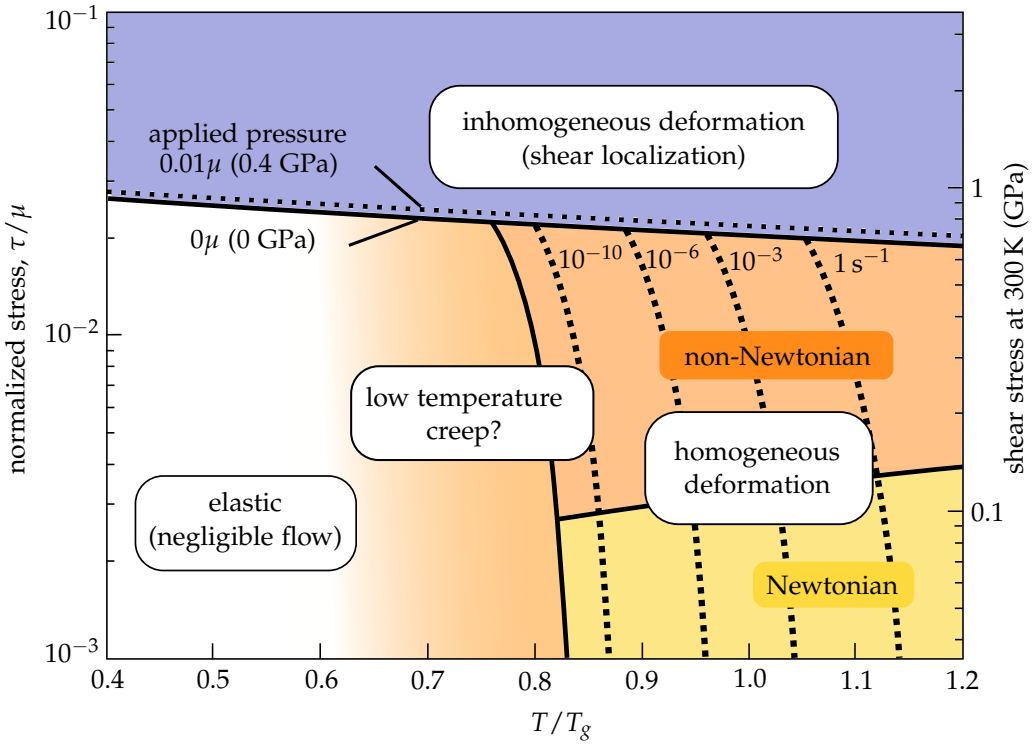

FIGURE 2: Deformation map of $Zr_{41.2}Ti_{13.8}Cu_{12.5}Ni_{10}Be_{22.5}$ adapted from Ref. 2. In the inhomogeneous deformation regime, shear banding prevails. Homogeneous deformation is carried by the homogeneous nucleation of STZs. In this thesis, we are interested in the low-temperature and low stress regime at the transition between elastic and homogeneous deformation, where creep might occur.

the low temperature $\approx 0.7T_g$ and low stress region, as sketched in Figure 2, and probe the transition between the elastic and homogeneous flow regime for possible creep deformation. Finally, it is believed that β-relaxations are closely linked to STZ activation, especially since the activation energies of an STZ and a β-relaxation have been found to be very similar.[75] Thus, the response of MGs to sub-T_g annealing or creep, is probably closely linked to processes described in the framework of STZs.

1.4 ATOMISTIC STRUCTURE OF THE AMORPHOUS CU-ZR SYSTEM

MGs uniquely combine metallic bonding and amorphous structure.[45] In contrast to a classical silica-based glass, MGs do not consist of a large network of tetrahedral units, but contain a large variety of a variety of structural motifs, also known as Voronoi polyhedra. Many structure-property relations in MGs have been established from results of atomistic MD simulations.[24,25] A common way of characterizing short-range order in Cu-Zr model glasses is to measure the fraction of icosahedral units, also called full icosahedra (FI), whose presence are taken as struc-

tural indicator for mechanical strength.[12,45,76–78] $Cu_{64}Zr_{36}$ is the composition that incorporates the highest fraction of Cu-centered icosahedral units[24] and thus it has become a popular model system. During MD simulations of long-time annealing close to T_g over a time period of 1.8 µs, it has been observed that the Cu self-diffusivity is an order of magnitude larger than self-diffusivity of the Zr atoms.[79] Moreover, diffusing atoms generally seem to avoid regions where icosahedral short range order dominates. This supports the idea that geometrically unfavored motifs (GUMS) prevail in the softer, liquid like regions within the glass.[12] It has been shown that icosahedral order can be tuned by pressure,[77,80] and the general idea prevails that an increase of icosahedral units also correlates with a low energy, i.e. relaxed, configuration of the glass. Recently, Ding *et al*. reported, however, an anomalous relationship between the icosahedral fraction and the total energy in glasses quenched under pressure. The pressure quenched glasses exhibit a raised number of icosahedral units and atomic density and at the same time an increased energy with respect to pressure-free quenched glasses.[80] It is debatable if the topological short range order is a sufficient parameter to characterize MGs.[80] In fact, at least changes in the chemical short range order (CSRO) should also be considered. Ding *et al.* suggested an alternative per-atom structural parameter, the "flexibility volume":[81]

$$\nu_{\text{flex}} = f \cdot \Omega_a, \tag{1.3}$$

where Ω_a is the atomic volume and $f = \left\langle r^2 \right\rangle / a^2$ is the vibrational mean squared displacement normalized by the average atomic spacing $a = \sqrt[3]{\langle \Omega_a \rangle}$. In that way, the flexibility volume not only takes into account how large the free volume around a certain atom is but also how rigid this cage built by its atomic neighborhood is. Thus, both an increased atomic volume and increased mean squared displacement of the atom are necessary for large values of the ν_{flex}. Furthermore, regions of high flexibility volume are the regions that undergo the highest shear transformation.[81]

1.5 NANOGLASSES AND NANOCOMPOSITES

A general strategy for improving the mechanical properties of MGs has been to introduce crystalline secondary phases in the glass that can lead to enhanced ductility by reducing shear localization.[5–7,82,83] These crystalline phases can occur in various topologies ranging from micrometer-sized dendrites[5,6] to spherical nanoprecipitates[8,83,84] and the composites composed thereof exhibit tensile ductility at room temperature. Both the volume fraction and geometry of the precipitates influence whether the precipitates participate in the deformation, e.g. through cutting or blocking mechanisms.[9] An amorphous/crystalline dual–phase nanostructure based on a Mg-Cu-Y glass with $MgCu_2$ nanocrystals embedded in the amorphous matrix has proven to be very effective at blocking and splitting shear bands into smaller sub-bands.[85] Alternative glassy composite microstructures exist in the form of nanoglasses (NG).[86–89] They can be seen in analogy to nanocrystalline metals, except that they consist of glassy nanometer-sized grains connected by glass-glass interfaces. The processing route of a NG involves cold compaction of nanometer

sized glassy particles, which are typically synthesized by inert gas condensation[86,90] or by magnetron sputtering.[91] In both NGs and MG-composites, the presence of interfaces, i.e. either glass–crystal or internal glass–glass interfaces, plays a crucial role in their overall mechanical behavior. Crystal-glass interfaces are often the weak spot of a MG-based composite.[83] While thin crystalline interlayers in a MG were found to be metastable or even unstable,[92,93] Ritter *et al*. have proven that glass-glass interfaces in a Cu–Zr NG are stable up to the glass transition temperature T_g.[24] These interfaces should rather be viewed as soft secondary glass-phase, or "interphase", in which the nucleation of STZs is promoted.[24,94,95] In consequence, plastic deformation is more delocalized in NGs,[90] as compared to their homogeneous MG counterparts, which allows for a more homogeneous deformation and increased ductility. The degree of delocalization is also dependent on the grain size: In molecular dynamics (MD) simulations it has been shown that smaller grain sizes lead to more homogeneous plastic deformation.[96,97] Furthermore, the precursor particles used for cold compaction can exhibit surface segregation effects. Since the particle surfaces constitute the amorphous grain boundary phase in the cold-compacted NG, the surface segregation strongly influences the properties of the glass-glass interfaces present in the resulting NG.[90,98] Not only does the interphase exhibit a disturbed short range order in that case, but also a different composition and density than the embedded amorphous particles.[98] NGs in which the particles have undergone such a surface segregation during preprocessing are often termed segregated NGs.[98] In metals and ceramics, phase formation at interfaces has been characterized in the form of complexions[99–103] and this concept may also be a valid approach for NGs. According to the definition of Dillon and Harmer,[99] the interface interphase falls in the complexion category V: a wetting film, separated from the abutting phases through complexions. However, all the above composite strategies are often limited by a trade-off between ductility and strength, an issue which might be even more critical at elevated temperatures in the creep regime.

2

CREEP DEFORMATION

The phenomenon of creep describes the fact that some materials deform plastically when subjected to prolonged static stresses below their yield stress. This slow, time-dependent deformation can ultimately lead to the failure of an engineering component, especially in high-temperature applications, where creep deformation is more pronounced. But even well before material failure, the elongation of an engineering component during service life can have catastrophic consequences, an example would be the elongation of a turbine blade causing the blade to touch the outer turbine housing. Thus, understanding the mechanism of creep deformation is of utmost importance for designing a material for a specific engineering application.

While the phenomenon of creep deformation in metals and (crystalline) alloys is certainly of great technological importance, it is not unique to these materials: Partially crystalline materials such as polymers and ceramics and even glasses can exhibit significant creep deformation. That being said, the mechanism behind creep deformation in amorphous materials and especially MGs clearly can not be the same as in crystalline metals, due to the lack of long-range order and thus the absence of dislocations and other defects that that govern creep in crystals. However, the composite materials we treat in this thesis contain both glassy and crystalline phases, so the following sections introduce the creep mechanisms ascribed to both these states.

2.1 CONVENTIONAL CREEP

For crystalline solids, such as metals and alloys, the mechanisms behind creep deformation are well described, see e.g. Reviews 104–108. Dependent on temperature and applied stress, different dominant mechanisms have been identified that either involve atomic diffusion or dislocation activity. For many materials, the temperature and stress ranges where a certain mechanism prevails have been documented in so-called deformation maps as proposed by Ashby and Frost.[109] Figure 3 shows an exemplary deformation map for pure copper with a grain size of 0.1 mm. At low stresses diffusional flow dominates at all temperatures. However, only for high homologous temperatures atoms can diffuse through the grains as first described by Nabarro and Herring.[110,111] At lower temperatures diffusion through the grain boundaries is facilitated, so-called Coble-creep.[112] Based on the Borisov

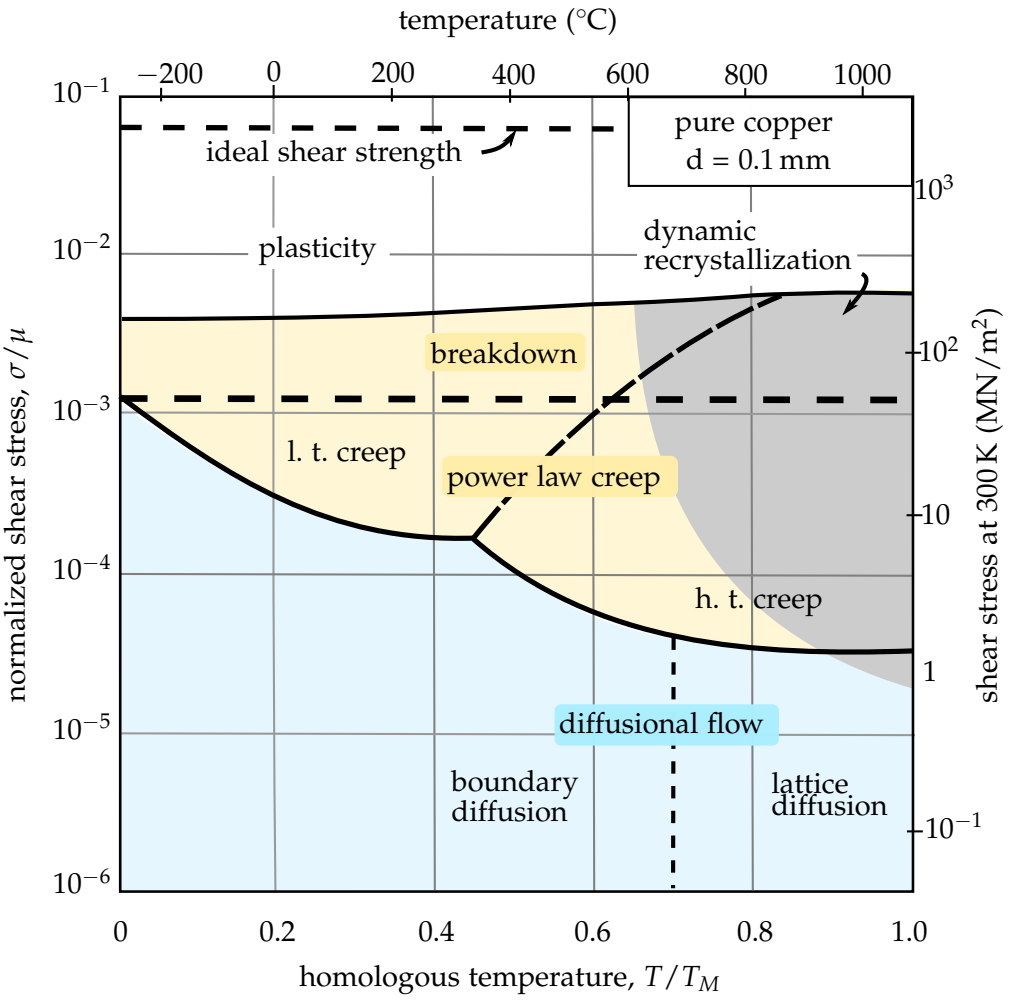

FIGURE 3: Deformation mechanism map for pure copper with a grain size of 0.1 mm reproduced from Ref. 109.

equation,[113] Gupta studied the influence of solute segregation in grain boundaries on the self-diffusion and found that the self-diffusion coefficient in the grain boundary, D_{GB}, and diffusion coefficient in the grain interior, $D_{lattice}$, relate with the excess grain boundary energy $\Delta\gamma$[114] as:

$$D_{GB} = D_{lattice} \cdot \exp\left(\frac{\Delta\gamma}{\rho k_B T}\right), \tag{2.1}$$

where ρ is a density factor. An increased excess energy $\Delta\gamma$ thus leads to an increase in grain boundary diffusion. In consequence, any excess energy introduced in the grain boundaries should also influence the creep compliance. The regime of

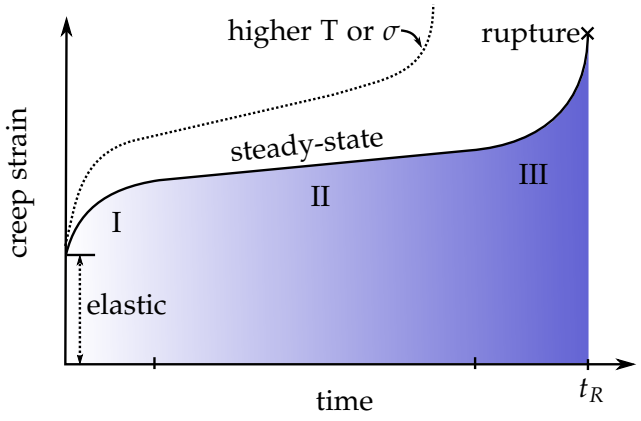

FIGURE 4: Evolution of the creep strain with time for constant stress and temperature conditions. The creep curve can be split into three regimes: The transient creep regime, followed by steady-state and eventually rupture.

diffusional flow is followed by the power-law-regime, which involves increased dislocation activity. In a generalized way, the creep rate $\dot{\epsilon}$ can then be expressed as

$$\dot{\epsilon} = B \cdot \sigma^n \exp\left(-\frac{Q}{kT}\right), \tag{2.2}$$

where $n > 1$ is the power-law exponent, B is a material constant and Q the activation energy for creep. For high temperatures and moderate stresses, dynamic recrystallization can occur as a competing mechanism reducing the flow stress. Eventually, with increasing stress, the power-law creep breaks down and the strain rates become high enough to observe "conventional" ductility.

To test the creep compliance of a certain material, it is usually subjected to a stress below yield (either maintaining constant stress or constant load conditions) at elevated temperatures. A typical creep curve depicting the mechanical response to such loading conditions is shown Figure 4. After an initial elastic response, three different creep regimes can be distinguished. In the transient creep regime I, the creep rate decreases fast and indicate strain hardening. Regime II is the so-called steady-state, where dislocation nucleation and annihilation are in equilibrium. In regime III, void and crack formation occur that finally lead to sample failure.

2.2 VISCOELASTIC CREEP

In literature on semi-crystalline and amorphous polymers, polymer-derived ceramics and metallic glasses, creep is mostly discussed in terms of viscoelasticity and often relevant at temperatures not too far from room temperature[49,115] - e.g. in Mg- and Ce-based MGs, where room temperature is greater than $0.7T_g$.[49,116]

In general, the response to a constant applied load of a viscoelastic material will contain an instant elastic part, a time-delayed anelastic part that can be recovered after the load is removed and an irreversible plastic deformation, see exemplary creep curves in Figure 5(a)-(c). Such a viscoelastic creep curve resembles more the form of the transient creep stage in Figure 4 without ever transitioning into the steady-state regime.

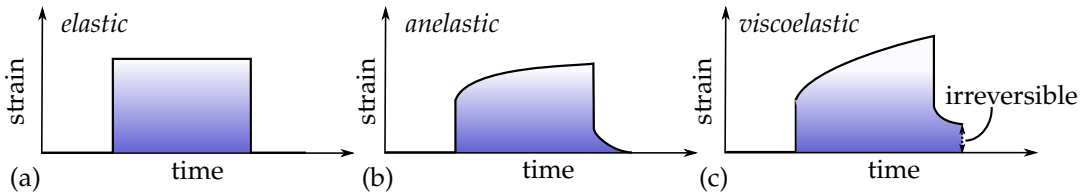

FIGURE 5: Possible strain responses to a constant applied load: (a) Pure elastic deformation, that is instantly recovered once the load is removed. (b) Anelastic deformation can be recovered after load removal and (c) Typical viscoelastic behavior, where an irreversible plastic deformation remains after load removal.

The creep compliance $J(t)$ describes how the strain ϵ evolves under an applied constant stress σ_0

$$\epsilon(t) = \sigma_0 \cdot J(t), \tag{2.3}$$

and following the schematics in Figures 5(a-c) is composed of an elastic, anelastic and viscous contribution

$$J(t) = \frac{1}{\mu} + \frac{1}{\mu}\phi(t) + \frac{t}{\eta}, \tag{2.4}$$

where μ is the shear modulus, $\phi(t)$ a retardation function and η the viscosity.

Furthermore, viscous flow and especially creep does not necessarily have to be Newtonian.[117–119] In early tensile creep tests on Ni-Fe MG plastic strains of up to 20% have been reached and a power-law creep behavior has been observed with stress exponents of $n = 7$ and $n = 10$ for higher temperatures.[117] In nanoindentation[49,66,120–123] and compression tests[124] on different glass alloy systems, homogeneous creep deformation has been observed and stress exponents have been measured. However, Li *et al*. have questioned the validity of the stress exponent extracted from nanoindentation data of MGs.[125] Many authors support the view that creep in metallic glasses resembles the homogeneous deformation as postulated by Argon.[65,126] The Argon model assumes temperatures $> 0.6T_g$ and occurrence of STZs that do not percolate the sample. The strain rate then depends on stress τ and temperature T as follows:

$$\dot{\epsilon}(\tau, T) = \alpha\nu_0\gamma_0 \cdot \exp\left(-\frac{Q}{kT}\right) \sinh\left(\tau \cdot \frac{\gamma_0\Omega}{kT}\right) . \tag{2.5}$$

Here, Q is the activation energy for plastic deformation (i.e. STZ activation), Ω is the volume of an STZ, γ_0 the characteristic shear strain of an STZ, ν its attempt frequency to flow and α a prefactor close to unity.[65]

Song *et al*. performed high temperature compression tests on Au-based MG micro-pillars[127] and comparison of their results with Argon's model for creep in metallic glasses allowed the extraction of activation energies. Molecular dynamics (MD) simulations of a 2D and 3D binary glass support this mechanistic picture of homogeneous deformation.[66,67] Interestingly, for CuZrNiAl MGs it has been found

that high-temperature mechanical creep has a positive effect on their room temperature ductility:[10] While an annealing treatment at 300 °C leads to brittleness, creep processing at room temperature was even able to restore ductility.

The literature on creep in polymers is mostly concerned with the physical aging of these materials, i.e. their relaxation towards structural and energetic equilibrium at temperatures below the glass transition temperature T_g. The creep behavior is often taken as a measure of how much a polymer has aged, see e.g. work by Struik[46] and Hutchinson[128] for an in depth treatment of the topic. The key results from Struik's work from over 40 years ago are still relevant today, in the sense that aging is a "basic feature of the glassy state" and should occur in all glasses. Moreover, Struik showed that for a wide range of materials (even including lead) the low strain creep response is very similar and only depends on the aging time. From the creep compliance data obtained for many polymeric materials, a master curve has been produced by vertical and horizontal shifts that follows the form

$$J(T) = J_0 \cdot \exp\left(\frac{t}{t_0}\right)^m \text{ where } m = \frac{1}{3}. \tag{2.6}$$

Although the mechanistic picture behind creep in polymers often remains elusive, the theoretical frameworks employed to explain the creep behavior is often the same, such as the potential energy landscape, free volume theory and the distribution of relaxation times. Interestingly, the whole discussion about rejuvenation and aging in glasses and the influence of the cooling rate on the structure is very similar.

Since polymer-derived glass ceramics have emerged as new potential candidate for high-temperature applications, creep is also being discussed in the context of amorphous ceramic matrix composites. It has been found that silicon oxide glasses[129–131] exhibit a high refractoriness with respect to creep. Several structure models have been proposed for these polymer derived ceramics – picturing a silica matrix and a secondary phase of excess carbon, either in the form of spherical graphitic nanodomains or a graphene-like network structure.[131,132] But information on the underlying mechanism of creep in these systems is still sparse.

For composites based on MG amorphous matrices, even less data is available. In metallic systems, the focus of recent efforts has been the improvement of ductility in the low-temperature regime, where shear banding is predominant.[5–9,82–84,133,134] While these composites are successful at modifying shear band propagation, few investigations on the role of the secondary crystalline phases in the high temperature, creep-like regime exist. A metallic glass composite of $Zr_{55}Al_{10}Cu_{30}Ni_5$ containing nanocrystalline tungsten particles has been synthesized, and found to exhibit an increased viscosity with increasing tungsten content.[135] The influence of spherical B2 precipitates on the viscous flow behavior of bulk metallic glass composites (Ti-Cu-Ni-Zr-Sn) has been studied in the SCL region.[136] Above a threshold value of 15% volume fraction, the presence of the secondary phase caused an increase in viscosity. The authors attributed this behavior to the high density of interface in the samples containing high volume fractions of secondary phase. During thermoplastic deformation heterogeneous flow behavior around the B2 particles and

lamella-like deformation flow in the surrounding matrix has been observed. If the presence of glass-crystal interfaces can influence the viscosity of the SCL, they very likely also play a large role in the deformation behavior at lower temperatures.

2.3 OPEN QUESTIONS

The work in this thesis builds on the $Cu_{64}Zr_{36}$-studies published by Ritter[24] and Brink,[25] who used MD computers simulations to understand plastic deformation in MGs with[25] and without[24] including structural heterogeneities. Our aim is to bridge the gap between the homogeneous elastic and inelastic regime in the deformation map (cf. Figure 2). We will treat the creep behavior of homogeneous MGs in Part I and then continue with different MG-composite models, including NG microstructures, in Part II. Generally, the research presented here has been motivated by the following questions:

Homogeneous glass

- On what time-scales can low-temperature creep be observed in the $Cu_{64}Zr_{36}$ system?
- How does creep influence the relaxation pathway in the PEL? Does it lead to rejuvenation or aging?

MG composites - Creep in the presence of interfaces

- Can the creep resilience be increased by the presence of secondary phases?
- How can we model interfaces / composite structures in MD and how does this affect the creep behavior?

Nanoglass composites

- Can nanoglasses be reinforced with crystalline phases?
- How does the presence of glass-glass or glass-crystal interfaces affect the creep behavior of nanoglasses?

3

METHODS AND MODEL SETUP

3.1 MOLECULAR DYNAMICS SIMULATIONS

In order to study the creep behavior of MGs and MG-composites, we need to be able to observe the underlying deformation mechanisms on the atomic scale. Atomistic simulations such as molecular dynamics (MD) are ideal for this task, since we can access the dynamic trajectories of the particles as well as all thermodynamic quantities that depend on the particle positions and velocities.[137,138] We are especially interested in the processes happening at the glass-crystal interfaces in the composite models, and the advantage of MD-simulations is that we do not require prior knowledge of the constitutive laws at the interfaces, except for the general description of the interaction between all atoms. The MD-simulation package LAMMPS developed by Sandia National Laboratories[139] has been used to perform all MD-simulations in this thesis.

In classical MD-simulations the atoms (in our solid) are typically treated as point masses $\{m_i\}$. The basic idea behind MD is then to evolve the ensemble of atoms in time by solving Newton's equation of motion:

$$m_i \frac{\partial^2 \boldsymbol{r}_i}{\partial t^2} = \boldsymbol{F}_i \left(\{\boldsymbol{r}_i\}\right), \; i = 1 \ldots N, \tag{3.1}$$

where $\boldsymbol{r}_i$ is the position and $\boldsymbol{F}_i$ the force acting on atom i. The forces are determined by the derivative of an appropriate interatomic potential $V\left(\{\boldsymbol{r}_j\}\right)$,

$$\boldsymbol{F}_i = -\boldsymbol{\nabla}_i V\left(\{\boldsymbol{r}_j\}\right) \;\; i,j = 1 \ldots \mathrm{N}. \tag{3.2}$$

3.1.1 *Interatomic potential*

Both the accuracy and computational efficiency of an MD calculation critically depend on the description of the interatomic interactions, already introduced as interatomic potential $V\left(\{\boldsymbol{r}_j\}\right)$ in Eq. 3.2. Technically, the interactions of atoms should always be treated quantum-mechanically. This is, however, computationally not feasible for systems containing more than a few hundred atoms. For the system sizes of up to 1.3 million atoms studied in this thesis, we need to resort to simpler descriptions of the atomic interactions, so-called empirical or semi-empirical potentials. Such a potential is a scalar function of all positions and often fitted to match both experimental and theoretical data, e.g. from density-functional theory.[140,141]

In simple pair potentials, like the Lennard-Jones or Morse[142] potentials, the potential energy is only a function of pair-wise distances r_{ij}, which is accurate enough to describe systems where van der Waals forces dominate, e.g. in monoatomic gases. The physics of metallic bonding, however, are better captured by many-body potentials like the embedded-atom-method (EAM) potential.[143,144] In addition to pairwise interactions $\phi(r_{ij})$ the EAM potential also includes an embedding energy, that depends on the electron density caused by the surrounding atoms. The EAM potential we use to simulate the amorphous $Cu_{64}Zr_{36}$ system and different Cu–Zr crystalline phases has been developed by Mendelev *et al.*[23] It follows the description by Finnis and Sinclair,[144] where the energy of an atom i of chemical species α is determined by pairwise interactions and an embedding energy F_α that takes into account the electron densities of all neighbor atoms j within the interaction cutoff. The chemical species of the neighboring atoms is denoted by the index β.

$$E_{\text{pot}} = \sum_i \left(\frac{1}{2} \sum_{j \neq i} \phi_{\alpha\beta}\left(r_{ij}\right) + F_\alpha \left[\sum_{j \neq i} \rho_{\alpha\beta}\left(r_{ij}\right) \right] \right). \tag{3.3}$$

In the non-Finnis-Sinclair form, ρ is insensitive to the chemical sort of atom i. The Finnis-Sinclair description uses electron density functions $\rho_{\alpha\beta}$ and is more suited for the description of alloys.

3.1.2 *Velocity-Verlet algorithm*

For the numerical time-integration of Eq. 3.1 an appropriate algorithm has to be chosen that is both numerically stable and efficient. The most common method, the so-called Verlet-algorithm, is based on summing up the Taylor expansion of the position at times $\boldsymbol{r}_i(t+\delta t)$ and $\boldsymbol{r}_i(t-\delta t)$ to arrive at

$$\boldsymbol{r}_i(t+\delta t) \quad = \quad 2\boldsymbol{r}_i(t) - \boldsymbol{r}_i(t-\delta t) + \frac{\boldsymbol{F}_i}{m_i}\delta t^2 \,. \tag{3.4}$$

Here, the calculation of the velocities $\boldsymbol{v}_i$ is not needed to update the particle positions. LAMMPS uses the velocity Verlet integrator, which is a slightly modified version of Eq. 3.4 and has the advantage that the new positions are formulated in terms of positions, velocities and forces, all at the same time step

$$\boldsymbol{r}_i(t+\delta t) \quad = \quad \boldsymbol{r}_i + \boldsymbol{v}_i(t)\delta t + \frac{1}{2}\frac{\boldsymbol{F}_i}{m_i}\delta t^2 \,, \tag{3.5}$$

$$\boldsymbol{v}_i(t+\delta t) \quad = \quad \boldsymbol{v}_i + \frac{1}{2m_i} \cdot \left(\boldsymbol{F}_i(t) + \boldsymbol{F}_i(t+\delta t)\right) \delta t. \tag{3.6}$$

The velocity at time $t+\delta t$ is then described according to Eq. 3.6, although typically an intermediate step is implemented where first

$$\boldsymbol{v}_i(t+\frac{1}{2}\delta t) = \boldsymbol{v}_i(t) + \frac{1}{2}\frac{\boldsymbol{F}_i(t)}{m_i}\delta t \tag{3.7}$$

is determined and then

$$\boldsymbol{v}_i(t+\delta t) = \boldsymbol{v}_i(t+\frac{1}{2}\delta t) + \frac{1}{2}\frac{\boldsymbol{F}_i(t+\delta t)}{m_i}\delta t. \tag{3.8}$$

3.1.3 *Boundary conditions*

Today's computational resources allow for MD simulations of system sizes of billions of atoms.[145] Although this is an enormous improvement as compared to systems that have been studied 60 years ago, this number still seems small when comparing to the number of atoms contained in one Mole, i.e. 6.02×10^{23}. To overcome this limitation of system sizes periodic boundary conditions are used in computer simulations. In that way, bulk systems can be represented and artefacts by the exaggerated number of surface atoms in these systems can be avoided. There is nonetheless a lower boundary to this method - finite size effects can occur for very small systems, when atoms interact with their own periodic images in the worst case. Figure 6 schematically explains the "key elements" of implementing periodic boundary conditions: (i) Atoms do not "leave" the simulation domain; whenever an atom surpasses a boundary it reenters the domain from the opposite side. (ii) This also means that atoms close to boundaries also interact with image atoms from "the other side". Thus, in Figure 6 the "real" distance between atom a and b is shorter than the apparent one.

More specifically, by controlling the boundary conditions in every dimension one can simulate (fully periodic) bulk samples or generate different surfaces. The surface properties of MGs play a major role in their deformation behavior, since in reality shear bands and cracks are nucleating at surface defects. Simulations of fully periodic samples are of course lacking these surface defects, but shear band nucleation can still be observed in such simulations: Ritter has studied the influence of $2d$- and $3d$-periodic boundary conditions on the deformation behavior of $Cu_{64}Zr_{36}$ and a detailed treatment can be found in Ref. 24. The key result is that shear band nucleation is facilitated at open surfaces. However, also MGs exhibiting fully periodic conditions can develop shear bands, but the simulation strain rates have to be slower than those used for shear band studies of $2d$-periodic samples.

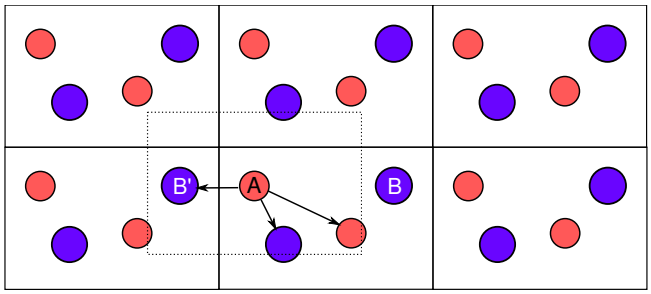

FIGURE 6: Schematic of how periodic boundary conditions work. Particle A interacts with particle B', which is the closest image of B.

3.1.4 *Pressure and temperature controls*

Equation 3.1 describes the many-body problem without any external influences, such as pressure P or temperature T induced by an external environment and samples the microcanonical ensemble (NVE). For the simulation of creep deformation, we need to be able to control the temperature and/or the external pressure and thus switch to the canonical (NVT) or isothermal-isobaric (NPT) ensembles. For that purpose we use the Nosé-Hoover thermo- and barostats, which are implemented in LAMMPS through the equations of motion proposed by Shinoda *et al.*[146] Both the thermo- and barostats require the input of a damping parameter that controls how fast the temperature or pressure is relaxed to the target value. In the creep simulations they are chosen as $T_{\text{damp}} = 0.1\,\text{ps}$ and $P_{\text{damp}} = 0.5\,\text{ps}$.

3.2 MOLECULAR STATICS

Static athermal relaxation of the system is sometimes necessary to obtain $0K$-properties, or before performing Voronoi analyses, as described below. This can also be done with LAMMPS, where the potential energy is minimized with respect to the particle coordinates.

$$\{\boldsymbol{r}_i^{\text{relaxed}}\} = \text{minarg}\; V\left(\{\boldsymbol{r}_i\}\right). \tag{3.9}$$

The atom coordinates are then iteratively adjusted towards the next local energy minimum by using a conjugate gradient minimization algorithm that is interrupted when the forces acting on the particles vanish.[147]

3.3 MODEL SETUP OF HOMOGENEOUS GLASS AND COMPOSITES

Setting up a MD-simulation not only requires an appropriate interatomic potential (cf. 3.1.1), but also the input of the initial particle positions (and velocities). Single-crystalline solids are fully described by their lattice parameters, basis and space-groups and can be built virtually by replication of their unit-cell. Amorphous materials lack such long-range order and computer models of glasses have to modeled using a different approach.

3.3.1 *Glass formation*

Indeed, the generation of virtual MGs is very similar to the experimental route, in the sense that they are quenched from the melt as schematically shown in Figure 1(a). In the work by Ritter the MD quenching parameters for the $Cu_{64}Zr_{36}$ system as well as their influence on the structure of the simulated glass have been established.[24] Following Ritter's quenching protocol, all MGs used in this thesis have been quenched from the melt from $T = 2000\,\text{K}$ to $T = 50\,\text{K}$ with a quenching rate of $\dot{T} = 0.01\,\text{K/ps}$. On MD-timescales such a quenching rate is rather slow,

performing the quenching with the before described parameters requires 97.5 million integration steps and force evaluations. To save computational resources, the quenched samples conventionally contain few tens of thousands of atoms, which are replicated later for mechanical testing. An additional equilibration step has to be performed after replication to avoid repeating patterns in the homogeneous glass.

3.3.2 *Composite formation*

In Ch. 7 we will treat MG-crystal composites and want to study the influence of the volume and interface fraction and the shape of the secondary phase. More specifically, we want to control all those parameters at the same time, such that for fixed volume fraction f and interface area A, the shape of the morphology of the secondary phase is varied, e.g. spheres, rods or a continuous network phase. Here it is useful to normalize the glass–crystal interface area A with respect to the overall composite volume and introduce the specific interface area ϕ,

$$\phi = \frac{A_{\text{interface}}}{V_{\text{composite}}}. \tag{3.10}$$

When controlling both Φ and f, the only degrees of freedom left are the number

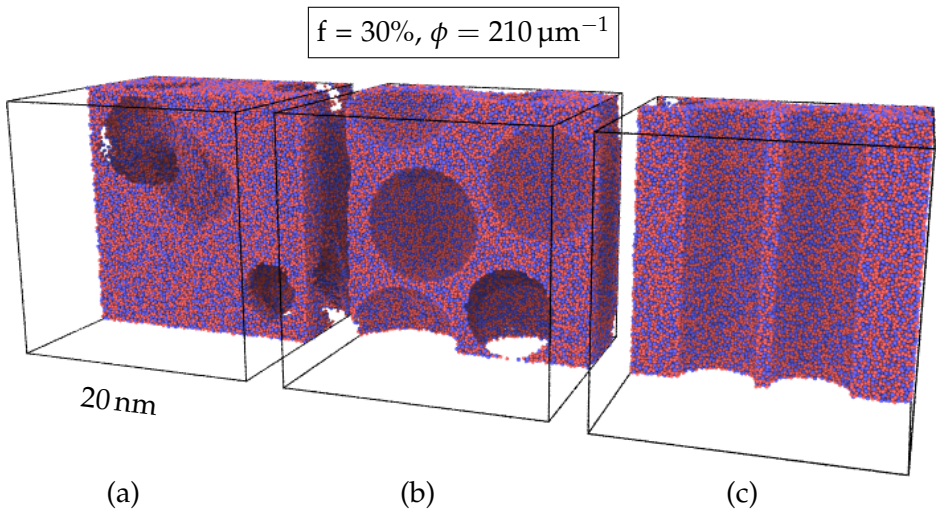

FIGURE 7: Glass matrix models for different secondary phase shapes, e.g. (a) continuous network, (b) spherical particles and (c) nanorods. The desired shape is cut out from the homogeneous glass and then later filled with single crystalline phase.

n and size d of inclusions. In the case of spherical inclusions, e.g., we need to solve the following system of equations for n and d,

$$n \cdot \frac{4}{3}\pi \left(\frac{d}{2}\right)^3 \cdot V_{\text{composite}}^{-1} = f, \tag{3.11}$$

$$n \cdot 4\pi \left(\frac{d}{2}\right)^2 \cdot V_{\text{composite}}^{-1} = \phi, \tag{3.12}$$

where n can only be an integer number. After the number of inclusions and their diameter have been determined, they are randomly distributed in the glass matrix while obeying periodic boundary conditions using the python scripting interface of OVITO.[148] All glass atoms that fall into these regions are then deleted. This is shown exemplarily in Figure 7. The glass matrix containing voids is then overlapped with a single crystalline cell of the same size and all crystal atoms that overlap with the glass atoms are deleted. Finally, the composites are statically minimized and subsequently equilibrated in the isothermal-isobaric ensemble for 1 ns at 300 K and zero pressure using MD.

3.3.2.1 *Spinodal composition via Monte Carlo*

The above described method is efficient but does not work for more physical secondary phase morphologies, such as continuous networks. In order to generate the latter we used a technique popular for modeling of nanoporous metals.[149] By means of kinetic Monte Carlo simulation[150] of a lattice based, 2-state Ising-Model we first simulate the spinodal decomposition of a binary alloy AB depicted in Figure 8. In that case the energy of a lattice site is given by

$$H_i = \sum_j J_{ij}, \tag{3.13}$$

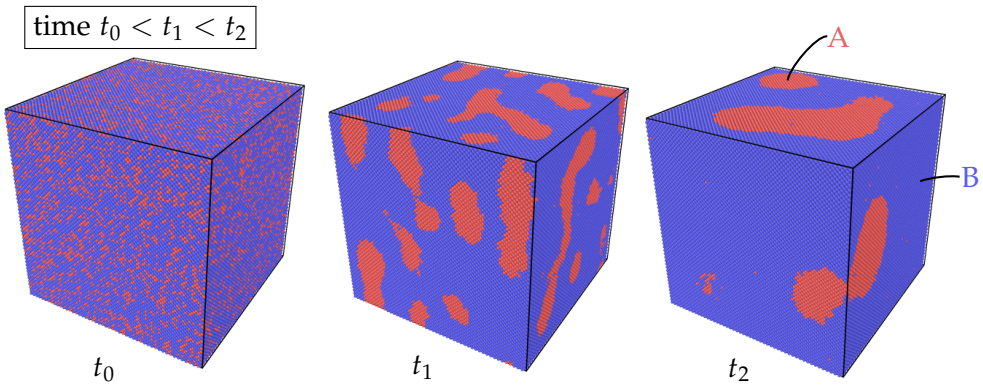

FIGURE 8: Spinodal decomposition of a binary alloy $A_{30}B_{70}$. In the initial configuration at t_0 atoms are randomly distributed. Then the system starts to demix. The longer the simulation time, the coarser is the network structure of phase A.

where j are the neighbors of i and J_{ij} is the Ising interaction parameter. After different simulation times, we extracted snapshots of the decomposed structure and removed the atoms of type B. What remains are porous microstructures with constant volume fraction but different ligament thickness and surface areas. With time the coarsening of the the network increases.

The simulations have been performed with the parallel Monte Carlo code SPPARKS developed by Sandia National Laboratories.[151] We used its on-lattice 2-state Ising application that restricts site exchanges to only take place between next-nearest neighbors, together with a kinetic Monte Carlo solver based on the implementation by Gibson and Bruck.[152] The box size was chosen to match that of the MG-samples and the Ising-parameters J_{ij} describing the interaction between next-neighbor atoms were set to 0.02 eV for unlike pairs and zero otherwise, as described in Ref. 149. The simulation has been performed at $T = 400\,\mathrm{K}$. During the early stages of the simulation, fine network structures with thin ligaments can be obtained, but the two phases still contain atoms of the other type. Thus, when extracting the network masks by removing the B-type atoms, the "free-floating" A-type atoms have to be removed as well. They can be identified using the cluster-analysis implemented in OVITO. These network structures are then used as masks to carve out a continuous network from the glass matrix and fill it with a secondary phase.

3.3.2.2 *Precipitation annealing*

The above presented method of using masks to delete overlapping atoms and subsequently equilibrating the composites is computationally efficient but bears the risk that rather unphysical high-energy glass–crystal interfaces might be created that are not well relaxed. As opposed to this masking method, we will also use composite samples, where the crystalline phase has been obtained through precipitation annealing. Using the Mendelev potential, Zemp and Brink have shown that the Cu_2Zr Laves phase is the primary forming crystal phase during simulations of long-time annealing of $Cu_{64}Zr_{36}$ close to T_g.[25,153,154] The short range order of the Laves phase is actually quite similar to the one exhibited by the energetically most favored motifs in amorphous $Cu_{64}Zr_{36}$ which will be explained further in Sec. 3.4.2. Brink studied the crystallization of the C15 and C14 Cu_2Zr phases during an annealing procedure at temperatures very close to T_g and simulation times of up to 4 µs. This procedure allowed to produce reinforced MG-crystal composites with different phase fractions and crystallite sizes.[25] It is important to note that the occurrence of this phase at temperatures below 1100 K is not predicted by the experimental phase diagram of Cu–Zr,[155,156] but the given interatomic potential stabilizes the Cu_2Zr Laves even at low temperatures.[157] In multicomponent systems such as Vitreloy1 or Vitreloy4, however, the occurrence of Laves phases has been confirmed.[158] In the context of this thesis we set aside the fact that Laves phases are not part of the equilibrium phase diagram of the $Cu_{64}Zr_{36}$ system. We rather use the samples produced by Brink[25] as a model system of a MG–crystal composite

with realistically grown interfaces as opposed to the artificially inserted secondary phases.

3.4 SIMULATION ANALYSIS AND VISUALIZATION WITH OVITO

The macroscopic creep curve of our samples is a direct output of the simulation runs as the strain can be obtained from the change in box length $\epsilon = \Delta l / l_0$. However, much more information can be extracted from snapshots of the atomic configurations taken during the course of the simulation, which is basically a list of the coordinates of all atoms. Thus, the bigger part of the work begins, when the simulation is done. For analysis and visualization of our data we mostly used the visualization and analysis tool OVITO.[148] In the following, important functions to characterize our MGs are introduced.

3.4.1 *Radial distribution function*

The beauty of the radial distribution function (RDF), or pair distribution function, is that this information is accessible to both simulations and experiments and can be directly compared. The RDF gives us information about the short range order in MGs, more specifically the probability of finding an atom at distance r in the neighborhood of another atom. For this purpose the space around each particle i is discretized into thin shells of width δr in which the number of neighbor atoms j

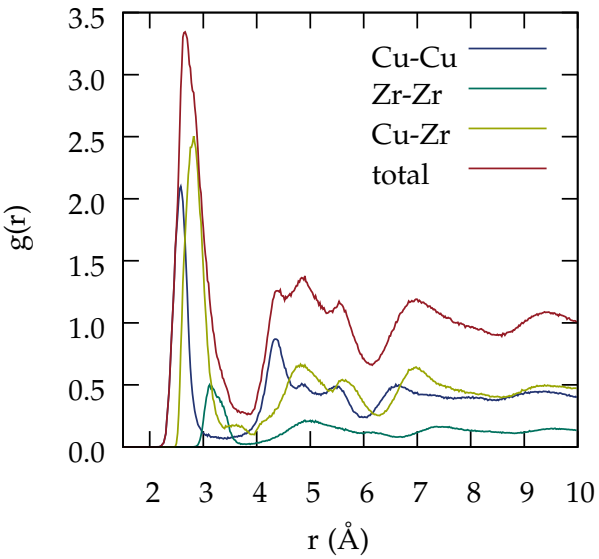

FIGURE 9: Partial and total radial distribution functions for $Cu_{64}Zr_{36}$ equilibrated at 50 K.

are counted. The total number of atoms, N, and the atomic number density, ρ_n, are needed for proper normalization.

$$g_{\mathrm{RDF}}(r) = \frac{1}{\frac{4}{3}\pi N \rho_n \left[(r+\delta r)^3 - r^3\right]} \sum_{i=1}^{N} \sum_{j \neq i}^{N} \begin{cases} 1 & r < r_{ij} < r + \delta r \\ 0 & \text{otherwise} \end{cases}, \tag{3.14}$$

In OVITO partial RDF's can also be calculated that take into account the chemical identities α and β of the atoms,

$$g^{\alpha\beta}_{\mathrm{RDF}}(r) = \frac{N}{\frac{4}{3}\pi N_\alpha N_\beta \rho_n \left[(r+\delta r)^3 - r^3\right]} \sum_{i \in \alpha}^{N} \sum_{j \in \beta}^{N} \begin{cases} 1 & r < r_{ij} < r + \delta r \\ 0 & \text{otherwise} \end{cases}, \tag{3.15}$$

where N_α and N_β are the number of atoms of each species.

As an example, Figure 9 shows the partial and total RDFs for a $Cu_{64}Zr_{36}$ sample equilibrated at 50 K using Mendelev's potential, where the total RDF (red) is the sum of the individual partial RDFs. The average nearest neighbor distance can be read from the position of the first peak in every curve and is 2.59 Å for Cu–Cu pairs, 3.13 Å for Zr–Zr pairs, and 2.83 Å for Cu–Zr pairs, which is in good agreement with experimental results.[23]

3.4.2 *Structure analysis*

Analysis of the crystal structure of the individual phases of the composite structures is realized through the adaptive common neighbor analysis (CNA)[159,160] in OVITO. For each atom, the local arrangement of the neighboring atoms is analyzed in terms of common neighbors, number of bonds between them and the number of bonds in the longest continuous chain of these bonds. The adaptive CNA automatically adjusts the cutoff radius for each particle. With the information of these

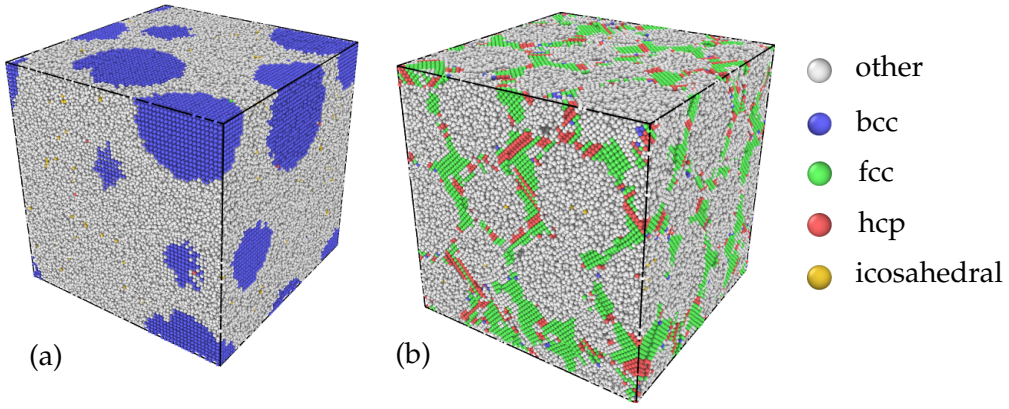

FIGURE 10: Snapshots of a (a) MG- and (b) NG-composite, where the atoms are color coded according to the common neighbor analysis method that identifies different crystalline structures. In the cases treated here, "other" means amorphous.

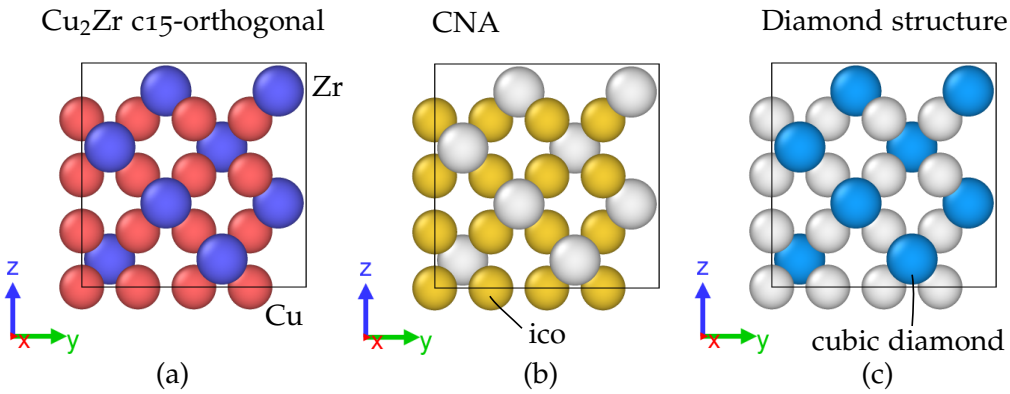

FIGURE 11: Structure identification of the (a) Cu_2Zr Laves phase. (b) Cu atoms, that reside in a Z12-Voronoi cluster are identified by means of CNA. (c) The Zr atoms are analyzed with OVITO's diamond structure analysis. Cu atoms, that are FI and neighbors to a Zr atom residing in a diamond-like superstructure are marked as Laves phase.

three values of all neighbors a structure type can be assigned. In that way we can distinguish between atoms in the fcc-Cu, bcc-CuZr and the amorphous $Cu_{64}Zr_{36}$ phase as shown in Figure 10.

As explained above, some composite models will contain C15 and C14 Cu_2Zr phases, for which we follow the two-step structure analysis described by Brink:[25] Since the Zr-atoms reside on a diamond-like super lattice, OVITO's diamond structure detection modifier can be used to identify Zr atoms belonging to the Laves phase according to that criterion. Furthermore, the Cu-atoms are known to be embedded in a 12-fold neighbor shell, that has the form of an icosahedron, which can be detected with the adaptive CNA or the Voronoi analysis as described below. Only if these Cu atoms are direct neighbors to the Zr atoms in the first neighbor shell, they are considered as part of the Laves phase. This is shown for the C15 Cu_2Zr structure in Figure 11.

3.4.3 *Voronoi analysis*

Another means to study the local atomic environment of an atom is the Voronoi analysis or tessellation method, during which the atomic cell is partitioned into small polyhedra, with each polyhedron enclosing an atom. This is realized by means of the Delaunay triangulation connecting the nearest neighbor atomic coordinates by line segments. In a next step, for each center point, the Voronoi cell is constructed from the intersections of all the planes that are bisecting each Delaunay line segment. This gives us information about the volume of the Voronoi cell, often referred to as atomic volume and the structural surrounding. In glasses, the short and medium range order is defined through the Voronoi indices of each atom, which contain information about the number of *i*-edged facets of that specific type

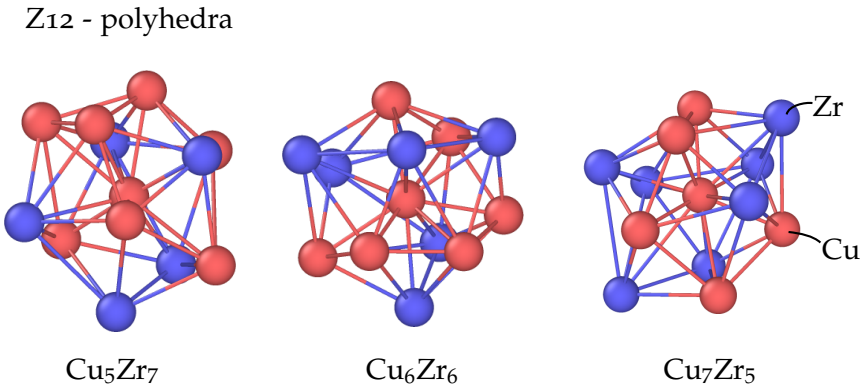

FIGURE 12: Cu centered Z12 polyhedra found in a $Cu_{64}Zr_{36}$ glass at 300 K. There are many types of Z12 clusters, since the chemical environment can vary. Shown are three representative examples ordered by increasing copper content: Cu_5Zr_7, Cu_6Zr_6 and Cu_7Zr_5.

$\langle n_3, n_4, n_5, n_6 \rangle$ and the coordination number. The signature motif of the $Cu_{64}Zr_{36}$ metallic glass is the $\langle 0, 0, 12, 0 \rangle$ dodecahedron, but more commonly called "icosahedron", since the cage formed by all the neighboring atoms is an icosahedron. In the literature this motif is often referred to as Z12-cluster. Their distorted versions are referred to as CN-12 clusters,[12] e.g., the $\langle 0, 2, 8, 2 \rangle$ polyhedron, which features two 4-edged and two 6-edged facets in addition to the 5-edged facets. One should add, however, that the Voronoi analysis does not take into account the chemical short range order (CSRO) of the polyhedra. Also, the same type of polyhedron can feature different bond lengths and facet sizes. Figure 12 illustrates this for the case of the Z12 cluster type. Three possible examples of Z12 clusters are presented in order of increasing Cu content. As a consequence of increasing Cu fraction, the potential energy of the center atom also increases, hence, the different Z12 clusters are energetically not equal.

3.4.4 *Shear localization*

The occurrence of STZs in MGs can be detected in the plastic von Mises shear strain field, where the homogeneous deformation has been eliminated.[161] First, an atomistic deformation gradient tensor J_i is calculated per atom which describes the deformation of a group of atoms in the neighborhood of the central atom i. Then, the Lagrangian strain tensor η_i is equal to

$$\eta_i = \frac{1}{2}\left(J_i J_i^T - I\right), \tag{3.16}$$

where I is the identity matrix. To translate that into a scalar atomic property the von local Mises shear invariant η_i^{Mises} is a useful quantity, with

$$\eta_i^{\text{Mises}} = \sqrt{\eta_{xy}^2 + \eta_{yz}^2 + \eta_{xz}^2 + \frac{\left(\eta_{yy} - \eta_{zz}\right)^2 + \left(\eta_{xx} - \eta_{zz}\right)^2 + \left(\eta_{xx} - \eta_{yy}\right)^2}{6}}. \tag{3.17}$$

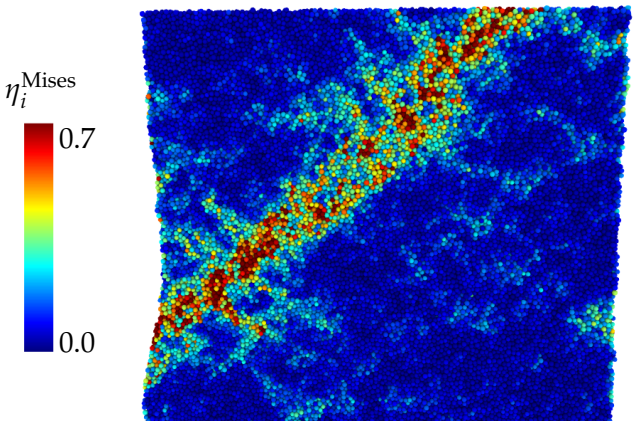

FIGURE 13: Snapshot of a deformed $Cu_{64}Zr_{36}$ MG, where the atoms are color coded according to the local von Mises shear strain η_i^{Mises}. A shear band has formed in the sample, visible as atoms that feature high values of the shear strain invariant, with respect to the surrounding matrix.

This per-atom information can then be used as to color code the atoms during deformation. Regions of high local von Mises shear strain η_i^{Mises} (a good threshold is $\eta_i > 0.2$) are usually associated with STZs. Sometimes, it can be useful to further condense the scalar atomic property η_i into one macroscopic parameter. For that purpose the strain localization parameter ψ was introduced by Cheng *et al.*. It basically captures the standard deviation of the mean local shear strain $\bar{\eta}^{\text{Mises}}$,

$$\Psi = \sqrt{\frac{1}{N}\sum_{i=1}^{N}\left(\eta_i^{\text{Mises}} - \bar{\eta}^{\text{Mises}}\right)^2}. \tag{3.18}$$

The values of the atomic shear strain of the atoms in a shear band are usually higher than in the matrix, i.e., they have a large variance with respect average value. Thus, the higher ψ, the more inhomogeneous is the deformation, which is a first indicator for the appearance of a shear band. Still, this has to be verified in the atomic von Mises strain field. Depending on the sample geometry, the shear band signal can be rather small, and the macroscopic Ψ then suggests homogeneous deformation. This problem is encountered in Ch. 5.

3.4.5 *Measuring surface/interface areas*

Characterization of composite models requires knowledge of the volume and interface fractions of the different phases. In MD-simulations the atoms are treated as point masses and they are conventionally visualized by drawing spheres around their coordinates, which do not form a continuous surface. How can we extract surface information from the coordinates of our point masses as sketched in Figure 14? OVITO uses a surface construction algorithm based on the α-shape method[162] that allows to reconstruct smooth surfaces from only the coordinates of the atoms in a specified phase. For that, the simulation box is first divided into tetrahedral elements via Delaunay tessellation of the simulation box.[163] Then, all those elements that have a circumsphere larger than a predefined probe-sphere radius R_α are cat-

egorized as empty. The "surface" is composed of the dividing facets between solid and empty tetrahedra. In case the surface resolution is still to detailed it can be further smoothed.[164] Note that this method is sensitive to its input parameters, the probe sphere radius R_α and the "smoothing" level, which should be kept fixed when comparing different structures. Throughout this thesis we use a $R_\alpha = 4\,\text{Å}$ and apply 11 iterations of the smoothing algorithm implemented in OVITO.

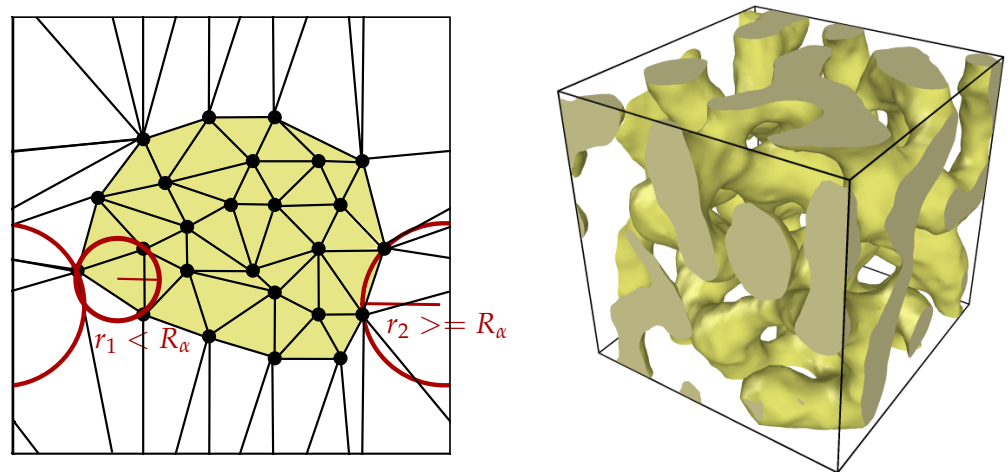

FIGURE 14: (a) Schematic of a 2d Delaunay triangulation and α-complex. (b) Surface representation of continuous network phase using the technique shown in (a) where the atoms are not shown.

Part II

HOMOGENEOUS METALLIC GLASS

4

TEMPERATURE AND STRESS DEPENDENCE OF CU-ZR BMG

The simulation of creep deformation by means of MD is quite challenging on account of the limited time scales accessible to this method. In simulations of conventional tensile tests of $Cu_{64}Zr_{36}$ MGs, strain rates on the order of $10^7\,s^{-1}$ or $10^8\,s^{-1}$ are usually employed to study shear band formation in MGs.[24,25] The combination of a typical integration time step of 2 fs with a constant engineering strain rate of $4 \times 10^7\,s^{-1}$, e.g., then yields a macroscopic strain of 10% in 2.5 ns. With the system sizes between 0.5 to 1.3 million atoms employed here, such simulations are usually realizable within less than 24 hours wall clock time. For our creep studies at constant stress conditions and low temperatures, however, we expect to observe deformation at much lower strain rates and thus a significant increase in simulation times necessary to observe measurable plastic deformation. Hence, in the following chapter, we will first establish the temperature, stress and simulation time parameter space necessary for the simulation of creep of homogeneous $Cu_{64}Zr_{36}$ MG, before treating the more complicated case of glass-crystal composites. Moreover, the possibility of surface effects is treated by comparing creep experiments under $2d$-periodic and $3d$-periodic boundary conditions.

4.1 SIMULATION SETUP

A $3d$-periodic homogeneous glass sample of composition $Cu_{64}Zr_{36}$ has been quenched from the melt ($T = 2000\,K$) to $T = 50\,K$ with a quenching rate of $\dot{T} = 0.01\,K/ps$ (as established in Ref. 24) and subsequently equilibrated for 2 ns. This has been realized in the NPT-ensemble, such that the pressure is completely released from the sample. The resulting sample contains 504864 atoms and its dimensions are $20 \times 20 \times 20\,nm^3$. Characterization of this glass sample in terms of RDFs have already been presented in Figure 9 in Ch. 3. This glass sample will also serve as matrix glass for the composite models in Ch. 7.

For creep testing, the as-quenched sample is heated to the desired target temperatures with $\dot{T} = 0.1\,K/ps$ before a constant uniaxial load is applied in z-direction. Both tensile and compressive loads have been tested. The pressure in the x- and y-directions is controlled ($P_{xx} = 0$ and $P_{yy} = 0$) to allow for lateral expansion. During the course of the simulation, the box-length in z-direction is measured to calculate the true creep strain $\epsilon = \log\left(\frac{l_z(t)}{l_z(t=0)}\right)$.

4.2 ARGON'S DEFORMATION MODEL

Figures 15(a) and (b) show the evolution of the true creep strain ϵ with time for different temperatures and tensile and compressive creep loads of 750 MPa. A first observation is that these curves exhibit the viscoelastic deformation behavior as described in Ch. 2. During the timescales of 40 ns simulated here, the creep rates are monotonously decreasing. Neither a quasi-linear steady-state regime nor sample failure do occur. Both the initial elastic strain and the creep rates increase with temperature. Even at the lowest simulated temperature of 450 K, which corresponds to about $0.5T_g$, the MG exhibits a viscoelastic creep strain of about 0.1% on the

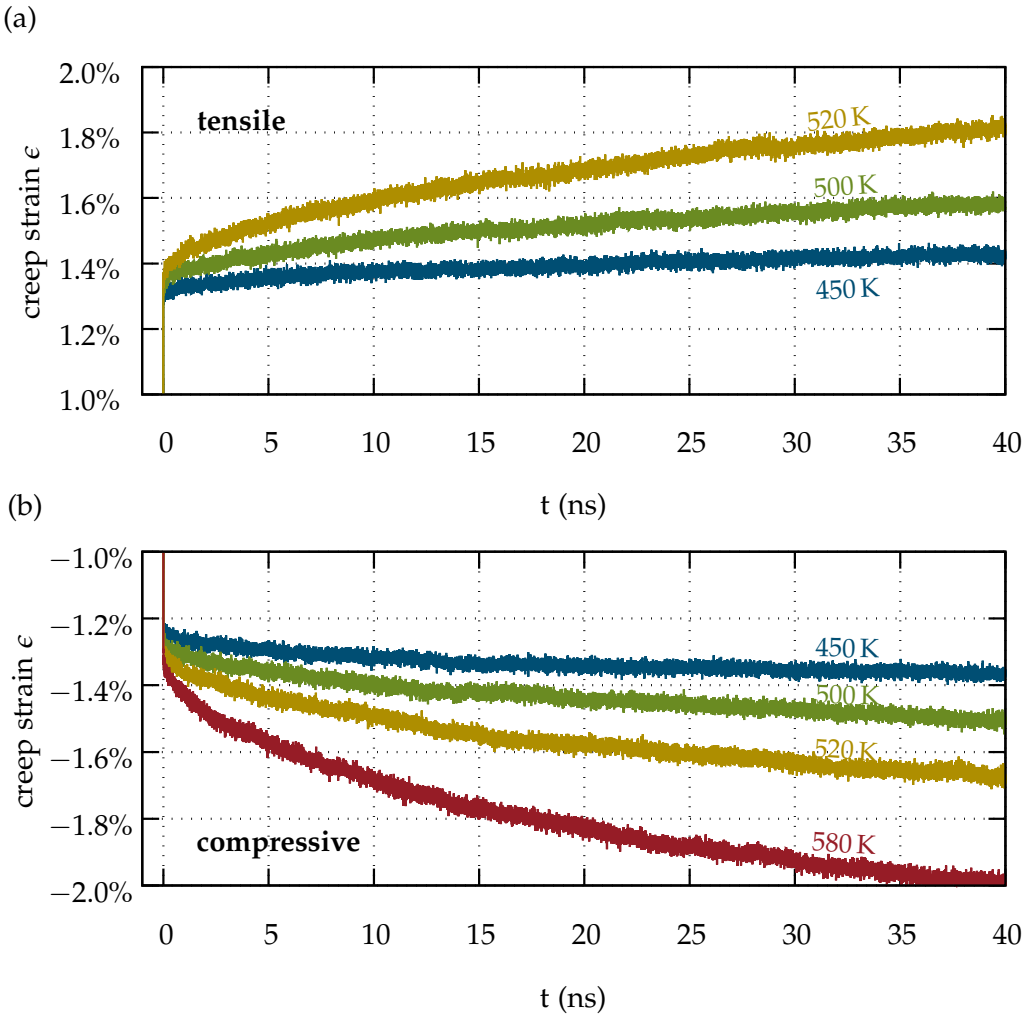

FIGURE 15: (a) Uniaxial tensile creep tests of homogeneous $Cu_{64}Zr_{36}$ at 750 MPa and T = 450 K, 500 K and 520 K. (b) Uniaxial compressive creep test at 750 MPa and T = 450 K, 500 K, 520 K and 580 K. The creep strain shown here is always the true creep strain.

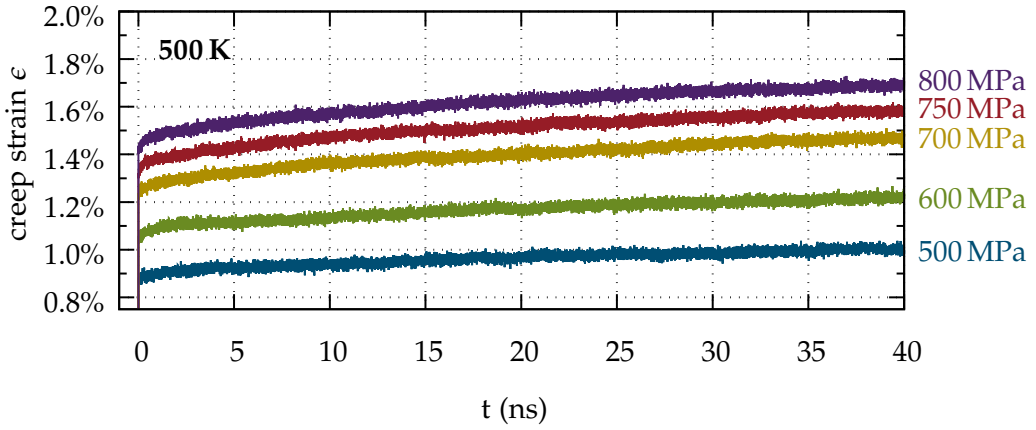

FIGURE 16: Uniaxial tensile creep tests of homogeneous $Cu_{64}Zr_{36}$ at 500 K and stresses ranging from 500 MPa to 800 MPa.

timescale of 40 ns. Although this seems negligible on the macroscopic scale, we expect that the viscoelastic creep deformation is accompanied by changes in the atomic structure and that those changes occur already in the early deformation stage.

When comparing tensile and compressive loads, the creep behavior is very similar. The absolute value of the total creep strain, however, is higher in tension than in compression. This matches results obtained from conventional loading conditions[45] and has been explained in terms of the free volume, that is diminished faster upon compression. Yet, we expect the underlying mechanism for creep deformation to be the same under tension and compression and thus will only discuss results for tensile creep loading in the following chapters.

In a next step, the stress dependence of the creep curves is examined. Figure 16 depicts the creep curves obtained at a fixed temperature of 500 K and stresses ranging from 500 MPa to 800 MPa. In this temperature and stress range, the stress increase is accompanied by an increase in the initial elastic strain from 0.9% to 1.4%. With respect to the total creep strain, the viscoelastic contributions, again, are small and increase from 0.15% to 0.3% between 500 MPa and 800 MPa.

What happens on the atomic level during creep deformation? Snapshots of the simulation cell showing only atoms with a local atomic von Mises shear strain $\eta_i \geq 0.2$ are depicted in Figure 17. The snapshots were taken after 10 ns and 40 ns of tensile creep deformation at 500 K and 750 MPa. The deformation is localized in clusters of a few atoms distributed homogeneously within the glass, which is consistent with the STZ picture. This suggests that, the mechanism behind creep deformation is the same as for conventional homogeneous deformation, i.e., nucleation of STZs.

Evidently, the creep rates depend both on the temperature and applied stress, as shown in Figure 18. The creep rates were obtained from linear fits of the true creep strain between $t = 25$ ns and $t = 40$ ns. We described above that the viscoelastic

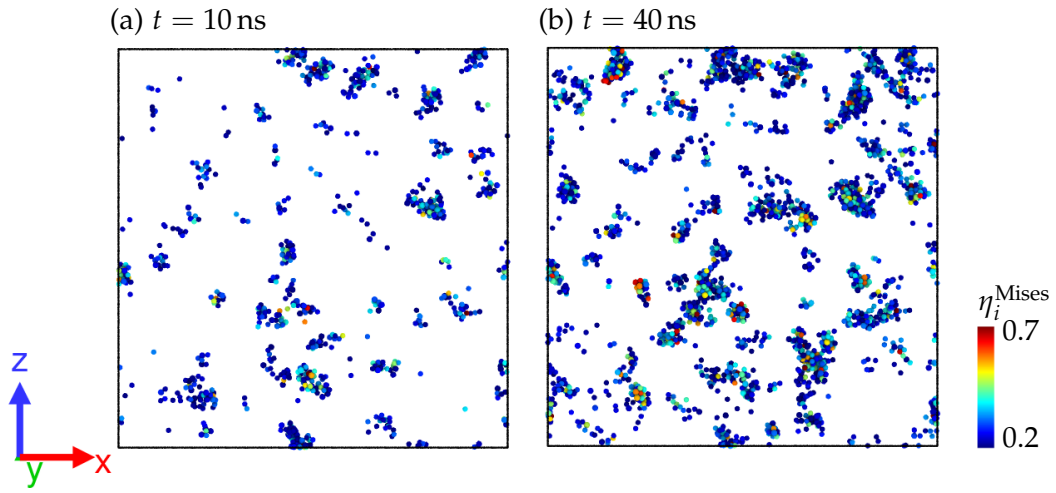

FIGURE 17: Slice of width $l = 2\,\mathrm{nm}$ through the simulation box after $t = 10\,\mathrm{ns}$ and $t = 40\,\mathrm{ns}$ of creep testing at 500 K and 750 MPa. The atoms are color coded according to the local von Mises shear strain. For better visibility, only atoms with $\eta_i \geq 0.2$ are shown here.

creep curves do not exhibit a steady-state regime, where the creep rate is constant. However, during short time frames, we can approximate the creep curves as linear and we chose to do so for the sake of simplicity. This allows to consistently compare the momentary creep values of the different creep experiments. Since, we could observe homogeneous deformation with STZs nucleating randomly throughout the sample, it seems reasonable to describe the temperature and stress dependence of the simulated creep rates through Argon's model for homogeneous deformation in MGs (cf. Eq. 2.5).[65,165] By fitting this model to our simulation data and using $\tau = \sigma/3$ (uniaxial tension) we obtain moderate agreement with the following fit parameters: The prefactor is $\alpha\nu_0\gamma = 11.15 \pm 1.16\,\mathrm{THz}$, the apparent activation energy for creep is $0.67 \pm 0.06\,\mathrm{eV}$ and $\gamma \cdot \Omega = 0.084 \pm 0.007\,\mathrm{nm}^3$, where Ω is the volume of an STZ and γ is the characteristic shear strain of an STZ. In the original publication, it is assumed that $\gamma = 0.1$.[65,165] Following this assumption we then obtain $\Omega = 840\,\mathrm{Å}^3$, which, for an average atomic volume of 16.4 Å in our $Cu_{64}Zr_{36}$ sample at 500 K, corresponds to about 51 atoms. The low-temperature and low-stress data show large scatter and the fit model does not match perfectly in this regime. This can have several reasons: First, the linear fitting between 25 ns and 40 ns might not be ideal to extract the creep rates, and statistics for individual creep rates could not be performed due to the large cost of each individual creep simulation. Secondly, the Argon model assumes a steady-state, which in our viscoelastic models never truly occurs. Moreover, it is based on the assumption that STZs do not influence each other and residual stresses are not considered.

However, our fit results give a general estimate of the apparent creep activation energy and are corroborated by findings from Kassner *et al.*,[166] who summarized the activation energies for creep of several metallic glasses. The values they found

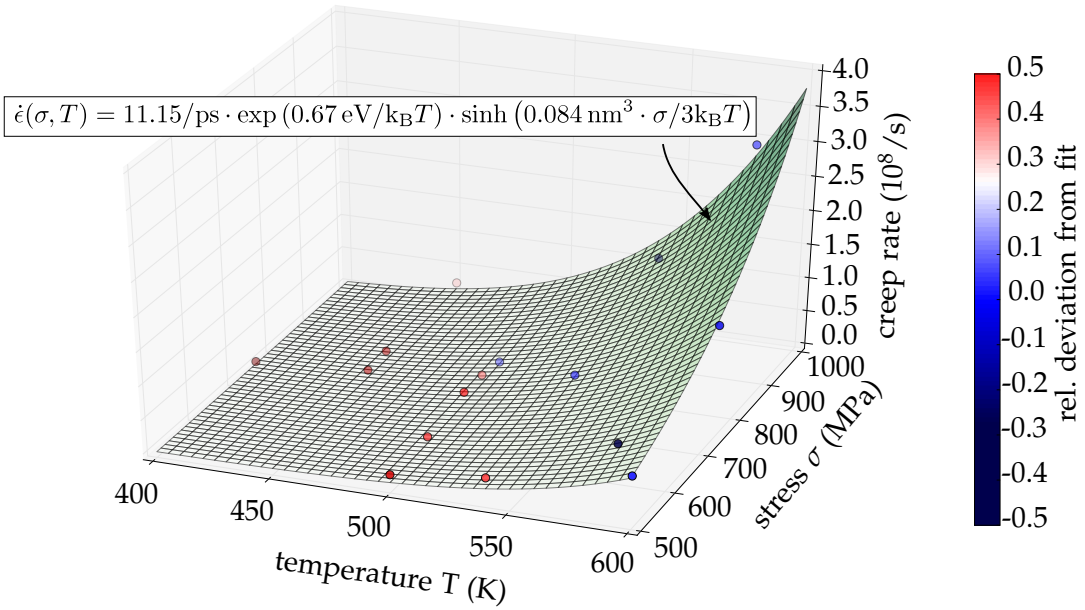

FIGURE 18: Fit of Argon model to creep rates obtained at different temperatures and stresses. The fit data is color coded to the relative deviation from the fit surface, see color bar on the right. The apparent activation energy for creep is 0.67 eV, with a standard deviation of $\pm$0.06 eV.

agree well with the activation energy of an STZ estimated by Schuh *et al.*,[2] i.e., 1–5 eV. For a $Cu_{60}Zr_{40}$ glass, with a composition close to the one used in this work, Argon and Kuo[165] measured an activation energy of about 2.4 eV.

4.3 BOUNDARY CONDITIONS

Both, in experiments and simulations, shear band nucleation is facilitated at stress concentrators at the sample surface.[24] Hence, the influence of surfaces on the creep deformation mode should be examined under the here applied creep conditions. We thus repeated the creep experiment at 500 K and 750 MPa with the same $Cu_{64}Zr_{36}$ sample, but non-periodic boundary conditions in y-direction, which introduces two surfaces in our sample. Figure 19 compares the creep curves of the fully periodic sample and a sample with open surfaces (2d-periodic boundary conditions). The true creep strain is higher for 2d-periodic sample, but the general shape of the creep curve is not altered. In addition, the analysis of the atomic von Mises shear strain showed that STZs still nucleate homogeneously throughout the glass sample and not only from surface defects. It is thus safe to assume that the creep deformation mode is independent of the boundary conditions.

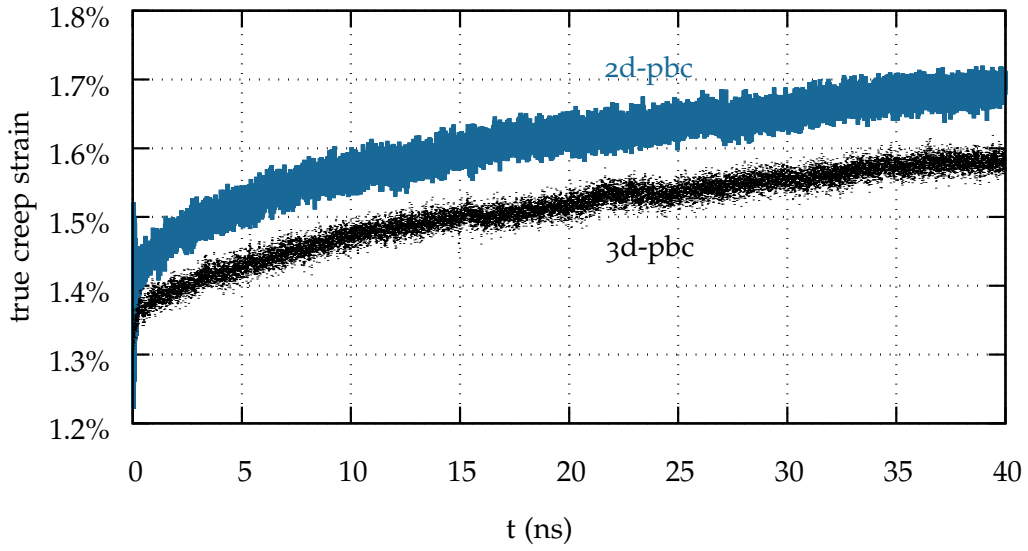

FIGURE 19: Creep curves of the same $Cu_{64}Zr_{36}$ glass sample simulated with $3d$ and $2d$-periodic boundary conditions.

4.4 CONCLUSION

In conclusion, we showed that a homogeneous $Cu_{64}Zr_{36}$ MG does exhibit creep deformation on MD-timescales - even at temperatures far below T_g and stress ranges below the yield stress. Furthermore, the creep deformation observed on the timescales simulated here was always homogeneous, and the mechanism behind the creep deformation is the same as during conventional loading conditions, i.e. the nucleation and activation of STZs. The temperature and stress-dependence of the creep rates resembles the widely recognized Argon-model.[65] Fitting the Argon model to our simulation data yields an average STZ size of 51 atoms and an apparent activation energy of 0.67 eV.

5

LONG-TERM CREEP BEHAVIOR

MGs modeled using MD simulations are usually not directly comparable to their experimental counterparts due to the limited quenching rates accessible on MD time scales.[45] The influence of the quenching rate on the final state of the MG has been explained in the framework of the PEL: The faster the quenching rate, the less relaxed is the resulting glass and the higher its energetic state. Fan *et al*. studied the influence of the quenching rate on the properties of the as-quenched glass, e.g., the activation energy spectrum.[167] When the glass is quenched more slowly the activation energy spectrum shifts to higher energies. A fast quenching on the other hand, resulted in a rather flat PEL, which decreases the barriers for STZ activation. These results motivate the question whether the PEL accessible to the MG can also be altered after quenching, e.g. during isothermal sub-T_g annealing or under creep conditions.

In the previous chapter we have simulated creep times of up to 40 ns to be able to sample the parameter space of temperature and stress while still containing the computational costs. However, in all cases the simulations were interrupted before a quasi-steady state was reached. Thus, it should be elucidated whether the absence of the steady-state regime is due to the limited simulation times or actually never occurring since the creep behavior is truly viscoelastic. Furthermore, when increasing the creep timescales from 40 ns to several hundreds nanoseconds, we expect interference of possible aging and rejuvenation effects. This chapter addresses the following questions: Firstly, we ask whether on timescales accessible to MD simulations a deep relaxation state can be reached by thermal annealing, which is comparable to the experimental situation.[30] Secondly, we inspect the possibility that thermal annealing under an elastostatic stress is accelerating the relaxation process, since there is possibly stress-assisted activation of local relaxation processes. Since also plastic deformation in MGs is a process that can be both thermally and mechanically activated, we are finally interested in the room temperature mechanical properties of binary $Cu_{64}Zr_{36}$ glasses that have been pretreated either by load-free annealing or under an elastostatic load. We are specifically interested in the question, whether strain localization can be observed at room temperature in well relaxed model samples and if mechanical prestraining has an influence on the plastic response.

5.1 SIMULATION SETUP

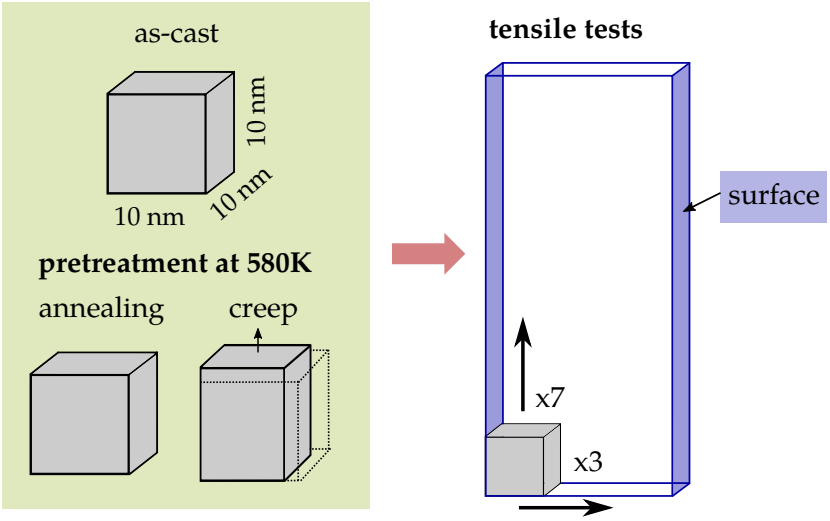

FIGURE 20: Simulation setup: Cubic precursors are prepared in annealing and creep experiments and then used as patterns for glass slabs of $1.3 \cdot 10^6$ atoms. These glass slabs are probed under conventional tensile testing at 50 K and room temperature.

The preparation of the $Cu_{64}Zr_{36}$ glass model is realized as follows: First, a MG sample composed of 63108 atoms is quenched from the melt to 50 K with a quenching rate of $\dot{T} = 0.01\,\mathrm{K/ps}$ and subsequently equilibrated for 2 ns as described in Ref. 168. Then replicas of this cubic master sample ($1000\,\mathrm{nm}^3$) are heated again to 580 K (about 0.65 T_g) at 0.1 K/ps and either (a) annealed at zero pressure or (b) annealed under a constant uniaxial load of 0.75 GPa for an extended period of up to 1 µs. After different annealing or creep times, the samples are unloaded and quenched to 50 K. We use these pretreated samples as patterns to build larger glass slabs of 1.3×10^6 atoms with dimensions of $30\,\mathrm{nm} \times 10\,\mathrm{nm} \times 70\,\mathrm{nm}$. The mechanical properties of these virtual slabs are finally determined in uniaxial tensile test experiments, which are performed with a constant engineering strain rate of $\dot{\epsilon} = 10^8\,/\mathrm{s}$. Ritter has shown for a similar glass geometry that under $2d$-periodic boundary conditions this strain rate is sufficient to study shear band formation.[24]

5.2 LONG-TIME SUB T_g ANNEALING

The lower red curve in Figure 21(a) shows the evolution of the potential energy during sub-T_g annealing at 580 K for 1 µs. The sample shows enhanced relaxation between 100 ns and 1 µs, which results in a final energy decrease of $2-3\,\mathrm{meV/atom}$. For comparison, the thermal energy at 580 K is $k_B \cdot 580\,\mathrm{K} \approx 50\,\mathrm{meV}$. The shape of the energy relaxation curve looks like it can be described by a decaying stretched exponential function (cf. Eq. 1.2). However, due to the scatter of the data it is difficult to extract reliable KWW-exponents β^{KWW} and relaxation times. As already

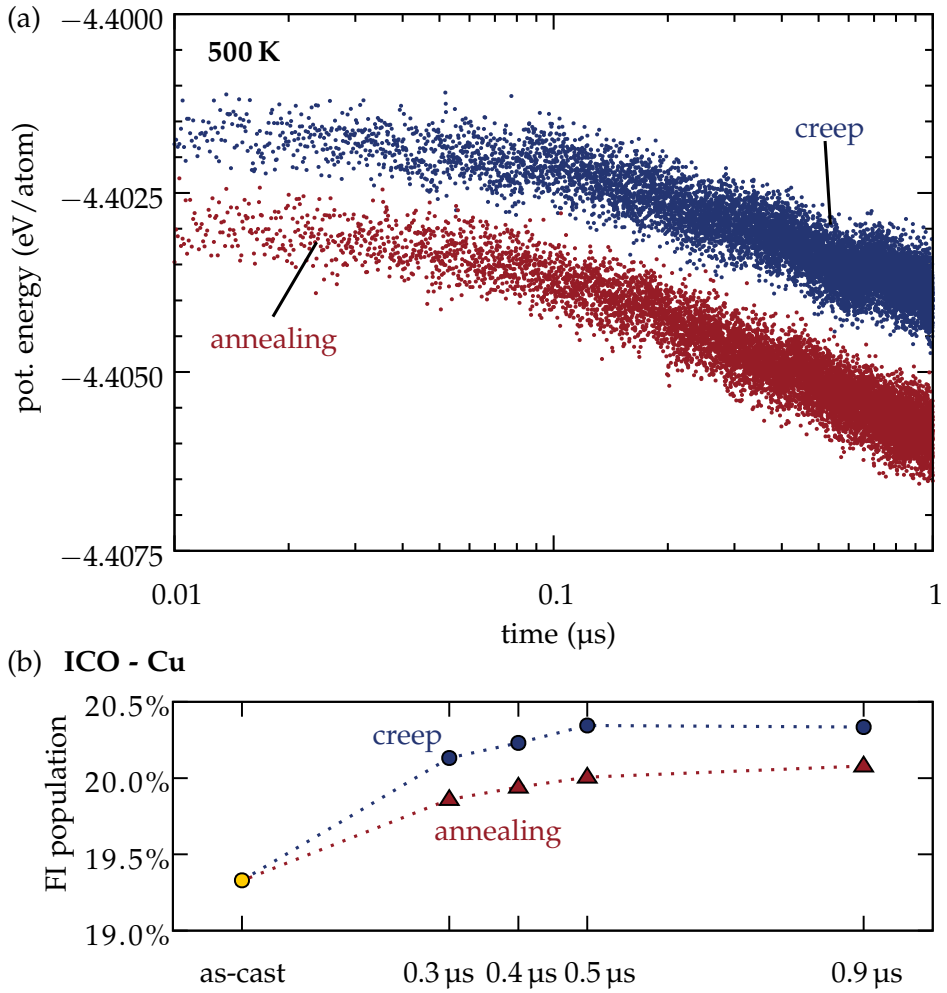

FIGURE 21: (a) Evolution of the potential energy during isothermal annealing with and without a constant elastostatic tensile load at 580 K. (b) Icosahedral fraction in the as-cast sample and in eight representative snapshots after different treatment times.

discussed in Ch. 2, in MGs the sub-T_g relaxation curve should be viewed as a sum of many relaxation events[55] rather than being represented by a single fit parameter β^{KWW}.

Moreover, the relaxation process is accompanied by an increase of icosahedral structural units in the glass, as depicted in Figure 21(b) for the four intermediate snapshots taken during annealing. Starting off from an initial level of 19.3%, the icosahedral unit fraction seems to slowly saturate reaching about 20.1% at the end of our simulation. The energy reduction accompanied by an increasing number of FI structural motifs suggests that long-time annealing, even at temperatures well below T_g, brings the glasses into a deeper state of relaxation. There is possibly an upper limit of FI units that can be accommodated in the current configurational state. At this point, we will first treat the case of load-free annealing. The creep data depicted in blue will be treated in Sec. 5.3.

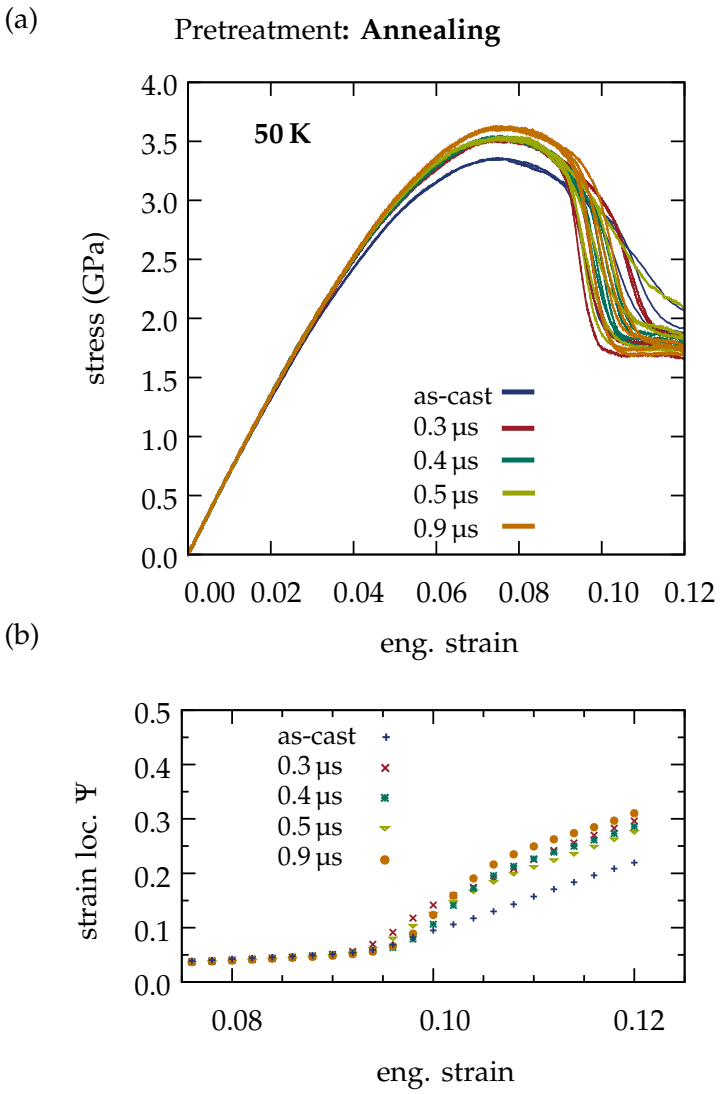

FIGURE 22: (a) Stress-strain curves from tensile tests performed at 50 K of the as-cast sample and samples that were annealed for a duration of 300 ns, 400 ns, 500 ns and 900 ns. For each treatment time, five independent simulations were performed and are plotted on top of each other in the color. (b) Evolution of the mean strain localization parameter with the macroscopic strain. Mean values are obtained from the five simulations for each sample set.

The FI fraction found in the glass is usually correlated with the mechanical strength.[24,45] Thus, in the next step, we will reveal what influence the annealing pretreatment has on the low-temperature mechanical properties at 50 K. After different annealing times, samples are taken and subjected to tensile tests. Prior to straining all samples are cooled down to 50 K at a quenching rate of 0.1 K/ps.

Because the cubic samples with an edge length of ~ 10 nm are too small to study deformation mechanisms such as shear banding, we build extended slabs by periodically replicating these precursors 3 times along x and 7 times along z. Periodic boundary conditions are used along the x- and z-dimensions (10 nm and 70 nm), while open boundary conditions are used along the third dimension (30 nm). These slabs are equilibrated for another 1 ns before a constant engineering strain rate of 10^8/s is applied in the z-direction. Furthermore, boundary conditions were such that normal stresses in the lateral directions remained close to zero. To assess the variability of the measured stress-strain curves, which is to be expected at such small scales, we performed five statistically independent tensile tests with each sample. For this purpose five different glass slabs have been built from each precursor by equilibrating the structures with a different random number generator seed for initializing the velocity distribution. The five stress-strain curves of each sample set are plotted on top of each other in Figure 22(a). From this analysis, it is evident that the value of the yield stress is reproducible while the flow stress is subject to large scatter. We observe that longer annealing times result in samples with a higher yield stress while the flow stress that is reached after the initial load drop is on average independent of the pretreatment time.

Snapshots in Figure 23 showing the shear strain distribution in the annealed and pretreated samples at 12% macroscopic strain reveal how a major shear band oriented at 45 ± 5 degrees to the loading direction has formed in all samples during the load drop. It can be seen that the pretreated samples develop slightly thicker shear bands, which may be responsible for the larger stress relieve. This visual observation is confirmed by an increase of the strain localization parameter ψ[169] [cf. Eq. 3.18] shown in Figure 22(b). While the as-cast samples exhibit a mean strain localization parameter of $\psi = 0.22$ (averaged over five runs), the mean values determined for the annealed samples range from $\psi = 0.28$ to 0.31. Note, that all calculated localization parameters show large error bars (up to ± 0.09), since the value depends on when and how the shear band develops. In the chosen sample geometry, the shear band always nucleates from the surface. The exact position and nucleation time is, however, subject to statistics. Nonetheless, the trend is visible that in the annealed, more relaxed glasses the strain localization is generally higher and shear bands grow thicker as compared to the as-cast sample.

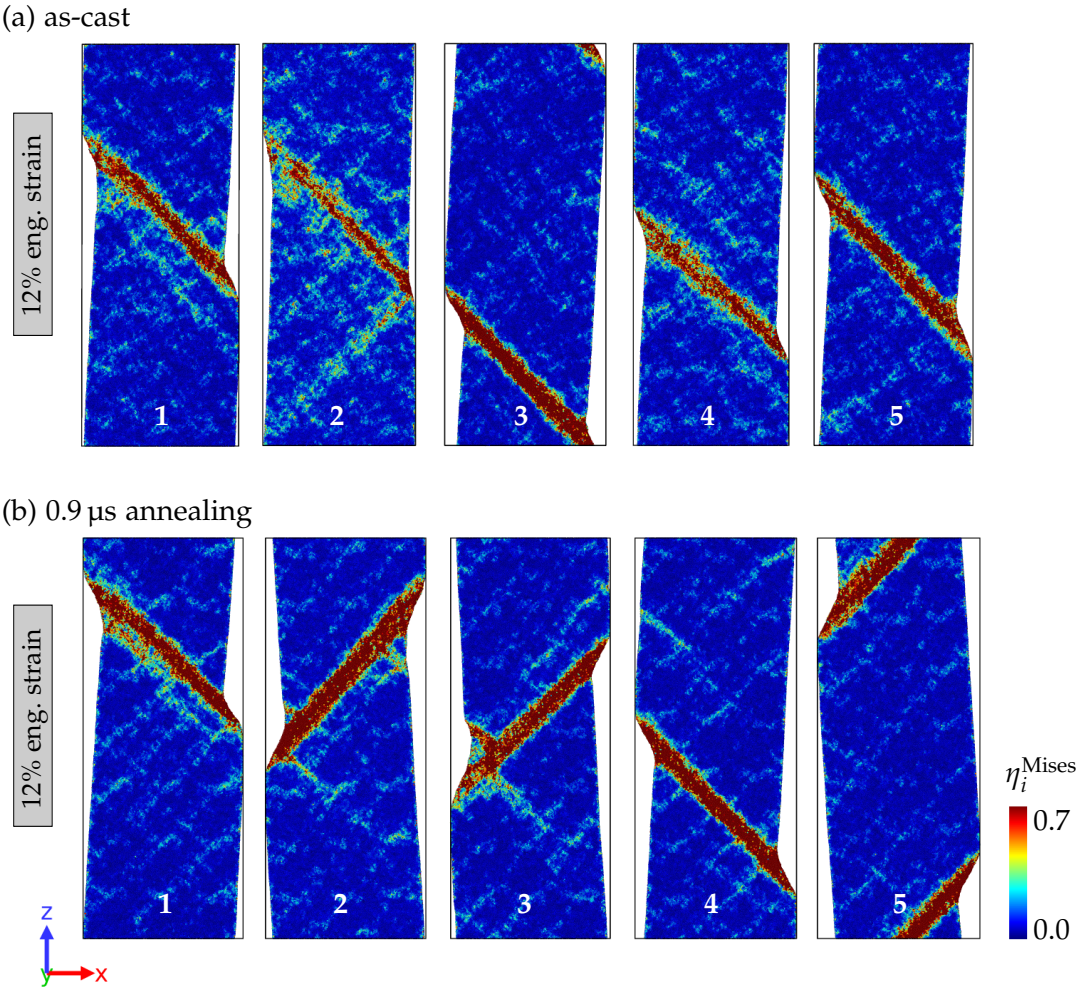

FIGURE 23: Snapshots of the atomic configurations at 50 K and 12% macroscopic strain, where the atoms are color coded according to the local atomic von Mises strain. Samples 1-5 in each row represent the five independent simulation runs for MGs (a) built from the as-cast precursors and (b) built from the precursor that has been annealed for 900 ns at 580 K.

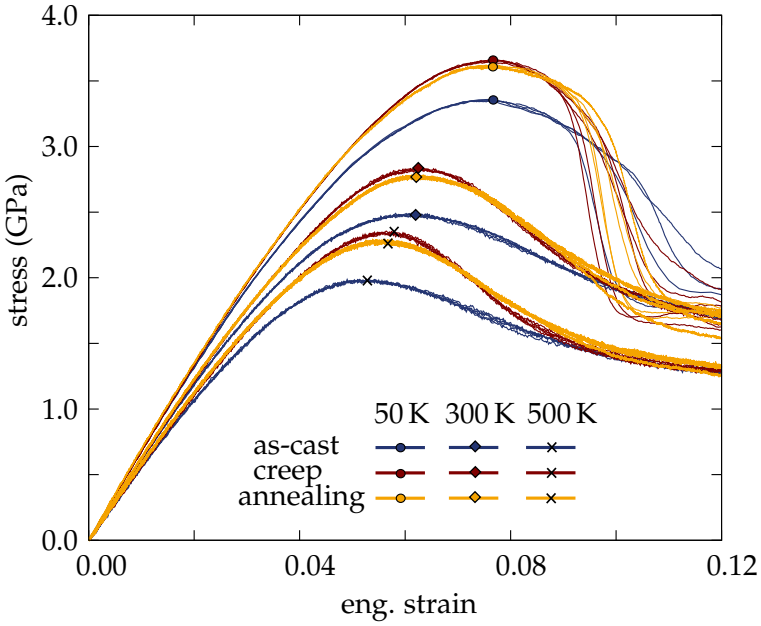

FIGURE 24: Stress-strain curves from tensile tests performed at 50 K, 300 K and 500 K of the as-cast sample and the samples that were annealed for 900 ns (both with and without applied constant load). Five independent simulation runs were performed and are plotted on top of each other. The strengthening effect caused by long-time annealing prevails even at 300 K and 500 K.

Glasses in simulations are commonly considered less relaxed than their experimental counterparts[83,167,170] due to the employed extreme quenching rates. Fan *et al*. found a shifting of the activation barrier distribution in a $Cu_{56}Zr_{44}$ glass towards higher energies[167] for glasses that were quenched at slower rates. In our case, that would explain why the deeply relaxed annealed glasses, that correspond to slowly quenched glasses, exhibit an increased yield strength with respect to the less-relaxed as-cast state. In order to still observe shear banding, the deformation behavior of MGs is conventionally studied in the low temperature regime only (50 K).[83] Thus, the question arises how the annealed samples with their increased number of FI motifs mechanically behave at higher temperatures. The yellow and blue curves depicted in Figure 24 represent the stress-strain curves of the samples in the as-cast and annealed (900 ns) states obtained at 50 K, 300 K and 500 K. As expected, the yield stress is reduced at higher temperatures. Furthermore, the absolute strengthening effect of the annealing pretreatment persists up to 500 K. Figure 25 depicts atomic snapshots of one as-cast and annealed sample set after having experienced 12% macroscopic strain during tensile testing at 300 K. At this temperature, the "unrelaxed" as-cast MGs always deform homogeneously and STZs nucleate uniformly in the samples. In contrast, all pretreated samples exhibit clear strain localization, albeit spread over more than one major shear band. Notably, formation of such shear bands visibly reduces the STZ activity in the remaining matrix. The above findings are summarized in Figure 26, that shows the temperature dependence of the yield stress and strain localization parameters observed in the as-cast and deeply relaxed glass taking into account five independent tensile tests for each data point. At all testing temperatures the average strain localization is larger in the relaxed glass than in the as-cast state. With increasing tempera-

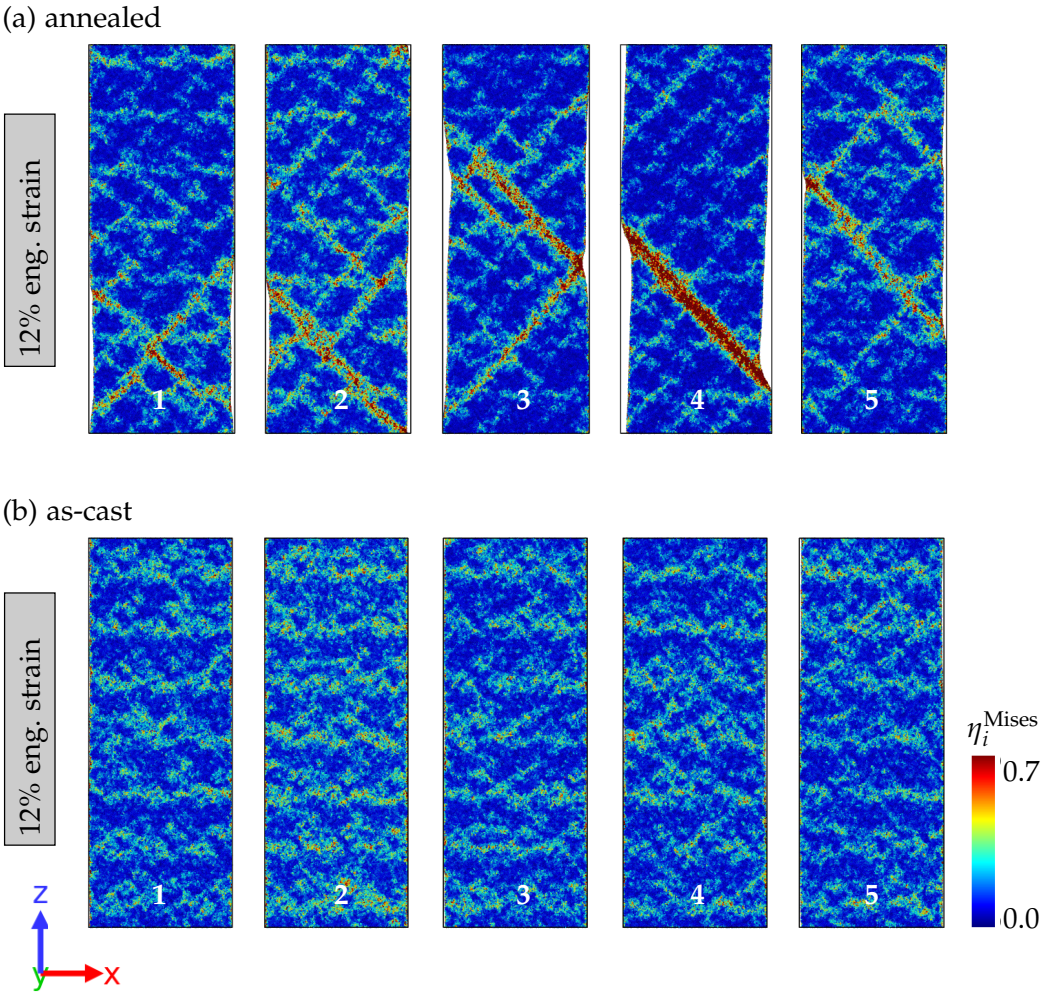

FIGURE 25: Snapshots of the atomic configurations of the five samples in each sample set after 12% macroscopic straining at 300 K. The atoms are color coded according to the local atomic von Mises strain. While the (b) as-cast samples only deform homogeneously, the annealed ones (a) clearly exhibit shear banding which is expected from experiments but unusual for simulations performed at 300 K.

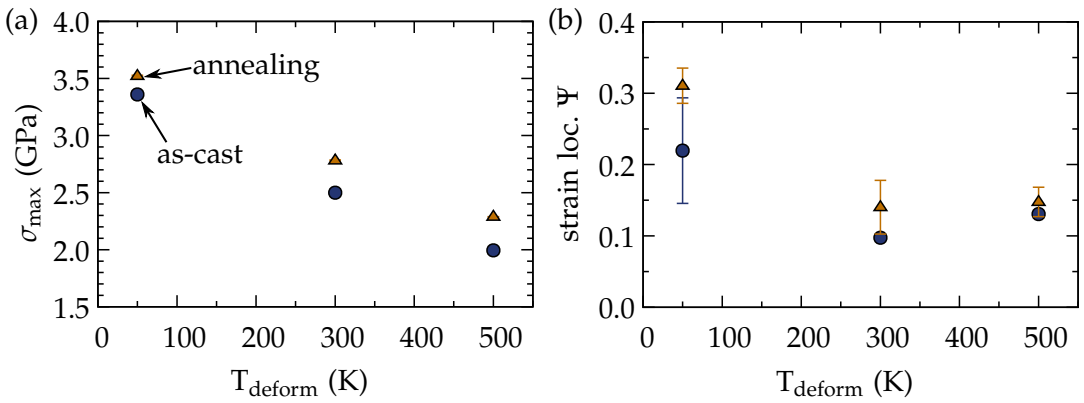

FIGURE 26: Temperature dependence of the (a) yield stress and (b) strain localization parameter of the as-cast and 900 ns annealed sample sets.

ture, the difference in the absolute value becomes smaller. Sample sets where shear bands occur are recognizable by having a non-negligible standard deviation to the average shear localization parameter, see Figure 26(b). These simulations provide proof that deformation via shear banding can be achieved in simulated glasses even at room temperature by pretreating the quenched structure at sub-T_g temperatures for an extended period of time.

5.3 UNIAXIAL CREEP LOADING

We have shown, that opposite to earlier assumptions, shear banding can indeed be observed in room temperature simulations of conventional tensile tests of MGs, if the glasses are in a deeply relaxed state. Admittedly, a rather time-consuming annealing procedure was necessary to reach this relaxation state. Naturally, this raises the question whether the relaxation process can be manipulated, ideally even sped up, e.g. by applying external elastostatic stress to overcome local barriers. Thus, during the long-time annealing procedure, a uniaxial constant tensile load is applied, with the objective to impose creep conditions. In doing so, the same long-time annealing experiment was repeated at 580 K with the as-cast sample being subjected to an elastostatic load of 750 MPa.

Figure 27 shows the creep curve of the $Cu_{64}Zr_{36}$ metallic glass. It can be seen that over the entire time period of 1 µs, the creep rate still does not converge. This absence of a linear creep stage has been observed before for metallic glasses in both experiments and simulations:[49,121,171–173] The creep deformation can be decomposed into an elastic, a recoverable anelastic and a permanent viscoplastic part. It should be noted that MD simulations typically reach time scales around 100 ns and the creep deformation is mostly recoverable on such short intervals, because the elastic and anelastic part dominate over the irrecoverable deformation. Here, we observe that over an extended creep interval of 1 µs, a total strain of 5% is reached without any sign of failure. The simulation was interrupted after differ-

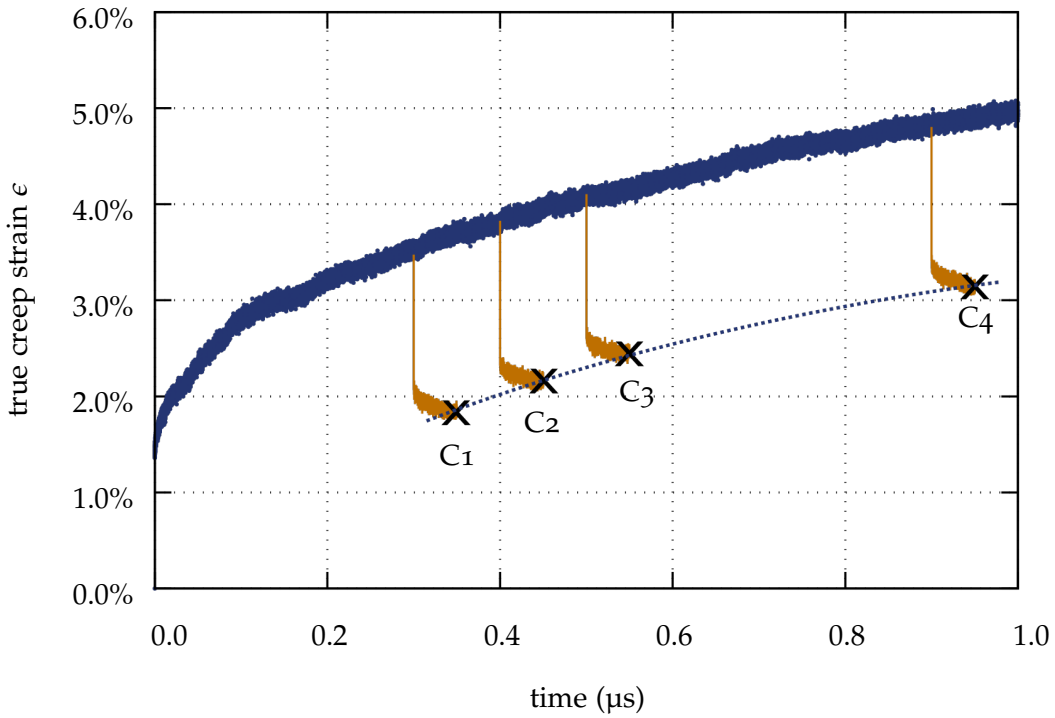

FIGURE 27: Creep curve of an as-cast $Cu_{64}Zr_{36}$ metallic glass obtained by static uniaxial tensile loading at 0.75 GPa and 580 K. After 300 ns, 400 ns, 500 ns and 900 ns the sample is unloaded and subsequently annealed at zero pressure for another 50 ns. The elastic and anelastic part of the creep deformation can be recovered during relaxation, the remaining plastic strains are marked with crosses.

ent times along the creep trajectory and replicas of the sample were unloaded and subsequently relaxed for another 50 ns at zero pressure and 580 K for comparison with their load free annealed counterparts shown in the previous section. These unloading processes are indicated by yellow curves in Figure 27, where the remaining strain after relaxation represents the irreversible plastic deformation. It is evident that the plastic strain monotonically increases, reaching more than 3% after 900 ns of creep time.

With these precursors, again, four sample sets with five slabs of 1.3×10^6 atoms were modeled and exposed to tensile tests at 50 K. Figures 28(c) and (d) show the stress-strain curves and mean strain-localization parameter for each sample set. For comparison, the tensile tests of the load-free annealed samples (cf. Figure 22) are shown again in Figure 28(a) and (b). At first, the situation does not appear much different to before. A prolonged creep pretreament, leads to an increased yield stress and strain localization. Note, however, that the straining direction during tensile testing is parallel to the direction of creep load during the described pretreatment. In Figure 29(a) we put the measured yield stress in relation to the change in potential energy per atom for the two sets of precursor materials, i.e.

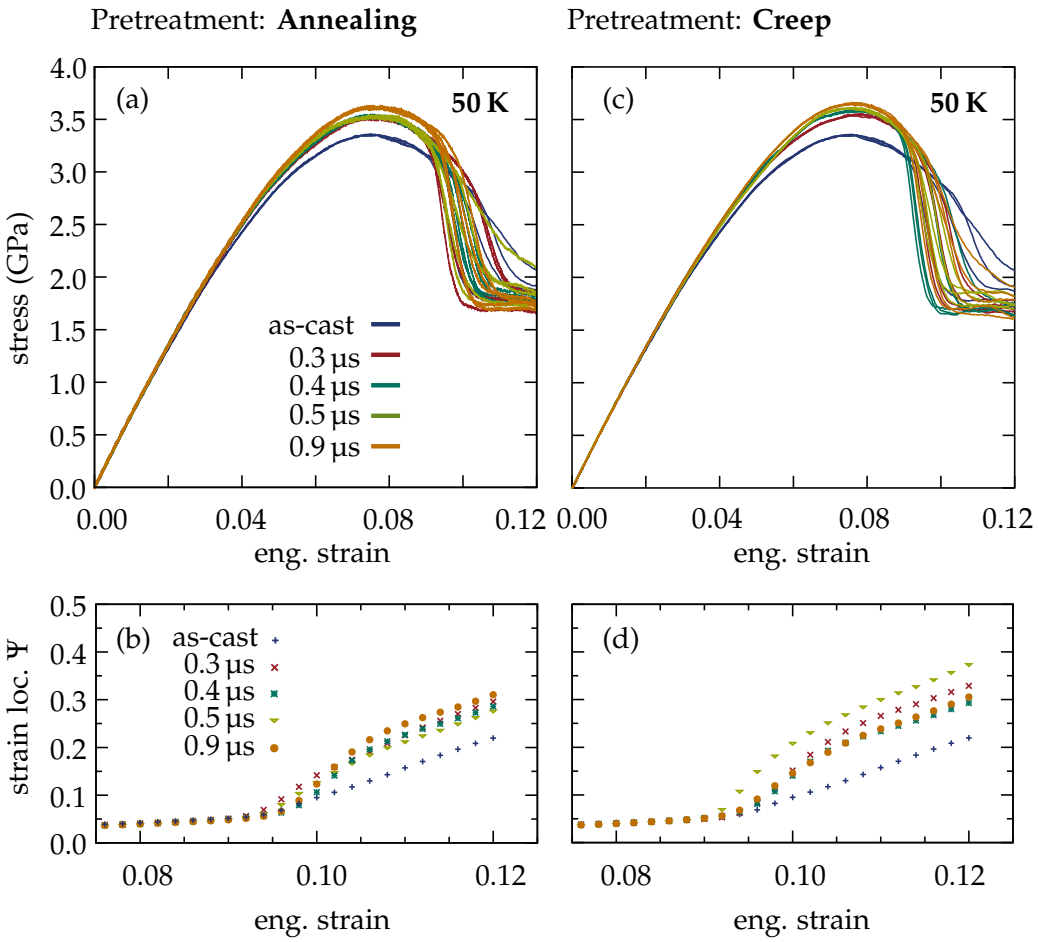

FIGURE 28: Stress-strain curves from tensile tests performed at 50 K of the as-cast sample and sample sets taken after 300 ns, 400 ns, 500 ns and 900 ns of (a) annealing pretreatment and (c) uniaxial creep loading. (b) Evolution of the mean strain localization parameter with the macroscopic strain in the annealed samples and (d) the creep samples. Mean values have been obtained from the five individual specimens of each sample set.

their degree of relaxation. The potential energy of the as-cast sample served as reference. Both types of pretreatment, creep loading and annealing, clearly lead to a strengthening of the material in comparison to the as-cast sample. More precisely: longer pretreatment times generally lead to a deeper relaxation state of the material (cf. Figure 29(a)) which in turn seems to correlate with the increased yield stress. This is an expected finding, because one would anticipate a depletion of readily activatable STZs in a glass that has been brought into a more relaxed state, making it more resistant to deformation.

If we directly compare the observations made for the two pretreatment procedures, however, the situation turns out to be more intricate (Figure 29(a)). For equal pretreatment times, the yield stress is always higher in the crept sample than in the corresponding annealed sample. This trend also prevails at room tempera-

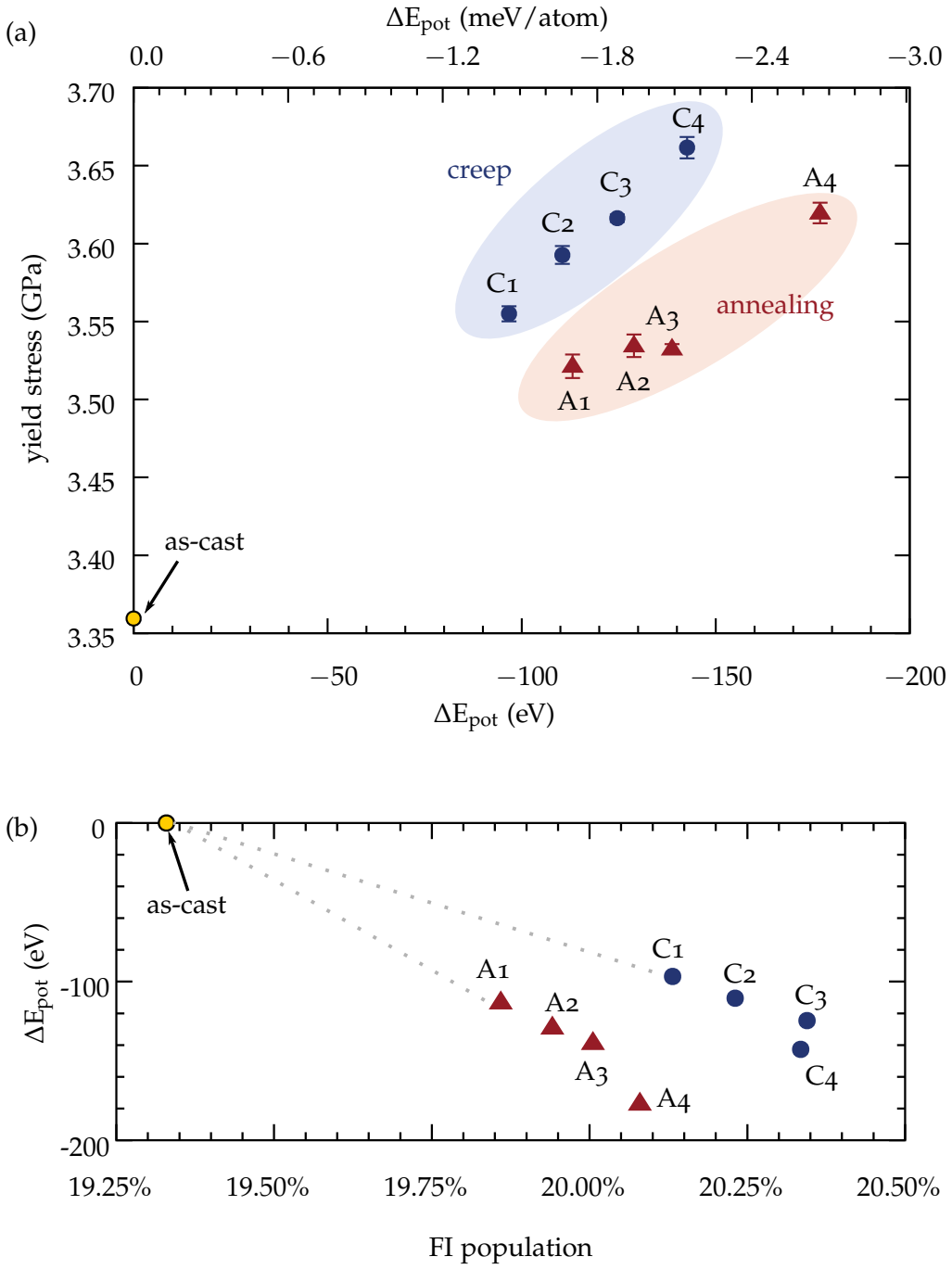

FIGURE 29: (a) Comparison of the yield stress of the as-cast, crept and annealed samples measured at 50 K. Each yield stress value has been computed from five independent tensile tests. The y-error bars show the corresponding standard deviation, in some cases the points are larger than the error bars. The x-axis shows the decrease in the potential energy (of the quenched samples minimized via the conjugate gradient method) with respect to the as-cast sample. The shaded areas solely serve as guide to the eye. In general, the potential energy of an annealed sample is lower than that of its creep counterpart. (b) Correlation of potential energy and FI fraction during relaxation.

ture and 500 K, shown in Figure 24. On the other hand, the athermal energy states of the annealed samples are lower than those of the corresponding creep samples. This matches the high-temperature results in Figure 21(a), where the evolution of the potential energy at 580 K is shown for both the annealing and creep pretreaments. Other than an offset due to the straining the curves exhibit a very similar shape. But clearly, no speed up of the relaxation process can be enforced through the creep pretreatment. On the contrary, the final glass state after 1 µs of creep is from an energetic point of view slightly rejuvenated with respect to the stress-free annealed one, since it resides in higher energetic state.

5.4 CHEMICAL AND TOPOLOGICAL SHORT RANGE ORDER

The previous observation seems to contradict the assumption that glasses exhibiting a lower energy state are generally stronger. In an attempt to resolve this discrepancy, we first examined the atomic structure of the glasses more closely and performed an atomic Voronoi analysis. Figures 21(b) shows the evolution of the fraction of Cu-centered icosahedra during annealing, here denoted as FI. Regardless of the pretreatment type, the number of FI always increases with time with a maximum increase of around 1%. A saturated state seems to be reached for pretreatment times longer than 500 ns. The increasing number of FI corroborates the finding that the yield stress increases with pretreatment time. But, again, the fact that the total number of FI, which are believed to be energetically more favorable over other motifs, is always higher in the crept samples than in the annealed ones seems to contradict their potential energy hierarchy as plotted in Figure 29(b). These findings render the density of FI, i.e. the icosahedral short range order (ISO) questionable as a structural indicator for the glass relaxation state. As stated by Ding *et al.*,[12] more characteristic parameters are needed to fully describe MGs, and the analysis of the Voronoi polyhedra should be extended to their CSRO as well. Indeed, when examining the CSRO of the FI present in the crept and annealed samples, we can observe that firstly, the favored CSRO among the FI is the Cu_6Zr_6 cluster shell as shown in Figure 30(a). Secondly, in the crept samples, the fraction of energetically less favored Cu_7Zr_5 clusters (with respect to Cu_6Zr_6) is increased. Furthermore, although these clusters share the same coordination number, their energies differ, which is depicted in Figure 30(b). The latter also shows that the mean potential energy of a Cu-atom in the center of a FI does not change much during creep or annealing when comparing the same CSRO. Moreover, it is evident, that the average potential energy of the FI center atom increases with increasing amount of direct Cu neighbors. The average potential energy of Cu center atoms of FI with eight Cu and four Zr neighbors even lies below the average potential energy of all Cu atoms in the sample, depicted as solid line in Figure 30(b). The distribution of FI clusters with different CSRO and their corresponding potential energies matches the trend, that the crept samples feature a higher number of FI but at the same time higher potential energies than the annealed samples: In the crept samples, the number of energetically more unfavorable Cu_7Zr_5 clusters increases faster than in

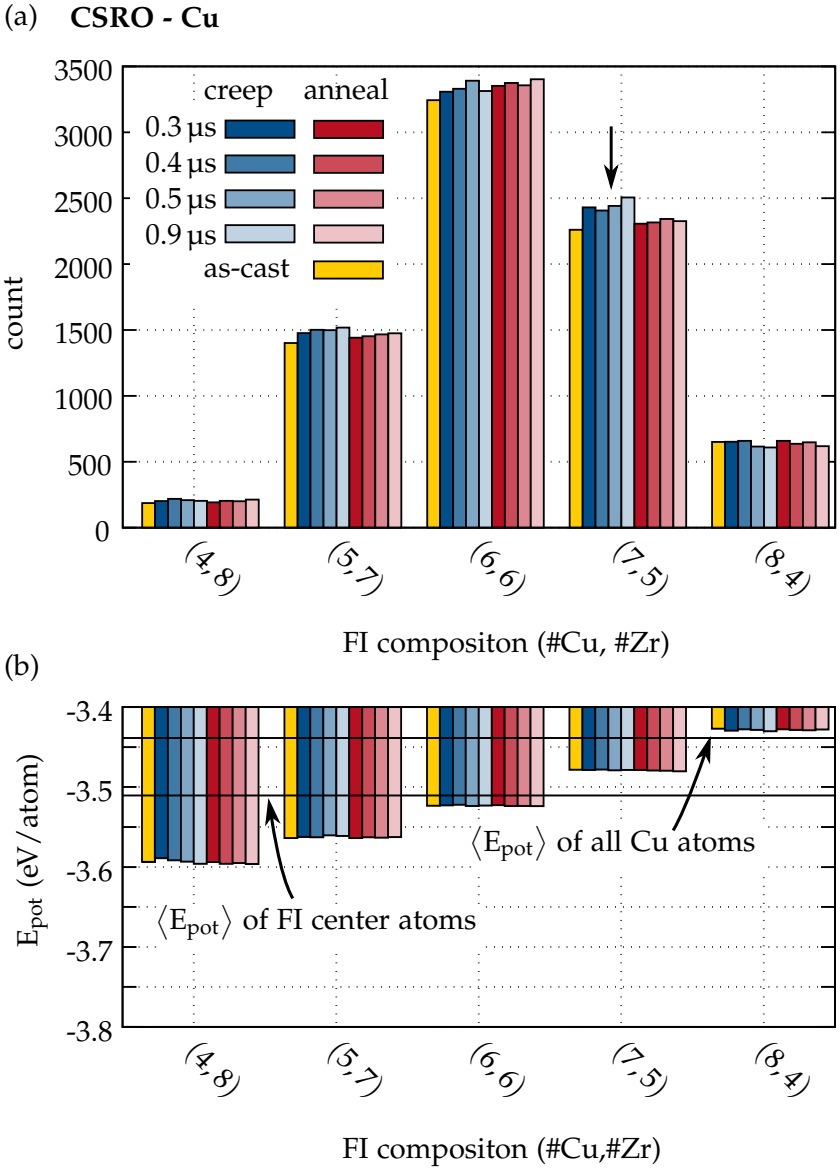

FIGURE 30: (a) Histogram of different FI cluster types ordered by increasing number of Cu atoms in the Z12 Voronoi polyhedron. In the creep samples, the population of Cu_7Zr_5 clusters is increased. (b) Potential energies of Cu atoms located in the different FI clusters ordered by increasing number of Cu neighbors. For comparison the average potential energy of all Cu atom and only those that are FI centers are shown.

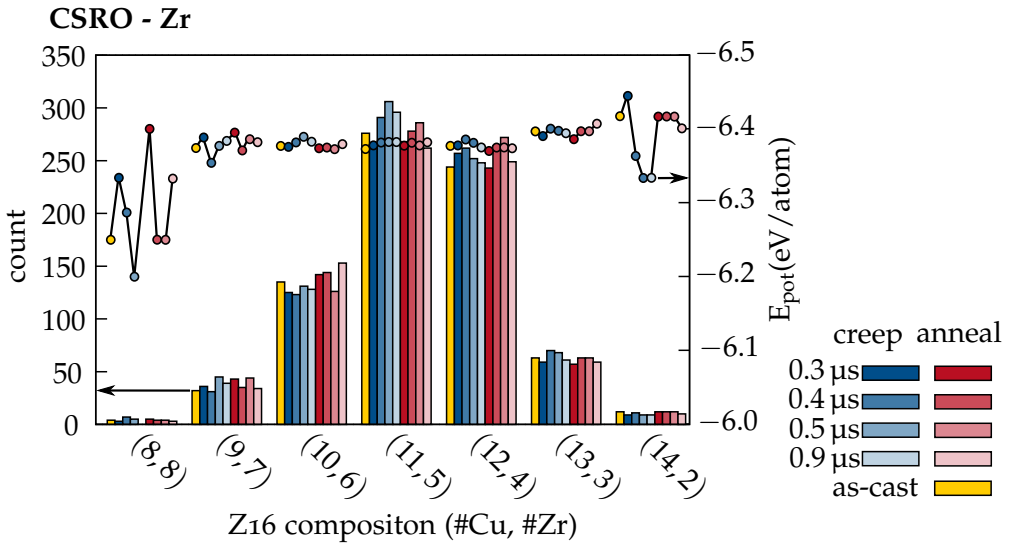

FIGURE 31: Histogram of different Zr-centered Z16 cluster types ordered by increasing number of Cu atoms in the Z16 Voronoi polyhedron. Potential energies of the Zr-centers belonging to different Z16 clusters are shown as points.

the annealed samples. This causes a shift in the distribution of FI potential energies and the average potential energy to higher values even though the absolute number of FI (which so far have been considered to be the energetically most favorable environment) is higher. Obviously this analysis would have to be repeated for the whole set of different Voronoi signature motifs to rule out other major contributions, however, we believe that the FI belonging to the largest representative are a good indicator. At least, the most frequent Zr-centered Z16 clusters ($N_{Cu} > 8$) do not exhibit large energetic differences (cf. Fig. 31).

We found that the distribution of FI clusters types characterized by their CSRO is different after the creep and annealing pretreatment. While this is an intriguing finding, the difference in atomic energies of these cluster types can not explain the overall energy difference.

5.5 ANISOTROPIC MECHANICAL RESPONSE

Returning to the fact that the straining tests were performed along the same tensile direction as the creep treatment: We can explicitly show that the material must have attained an anisotropic state after the creep treatment by repeating the straining experiment in a different direction, perpendicular to the creep load direction (Figure 34(b)). In this orientation, the yield stress of the creep sample becomes even lower as in the sample that has been annealed for the same duration under zero load, which becomes more clear from Figure 33. We note that these observations are independent of the geometry of the samples (3*d* periodic vs. thin-film geometry) as evidenced by the stress-strain curves presented in Figures 34(a)-(c).

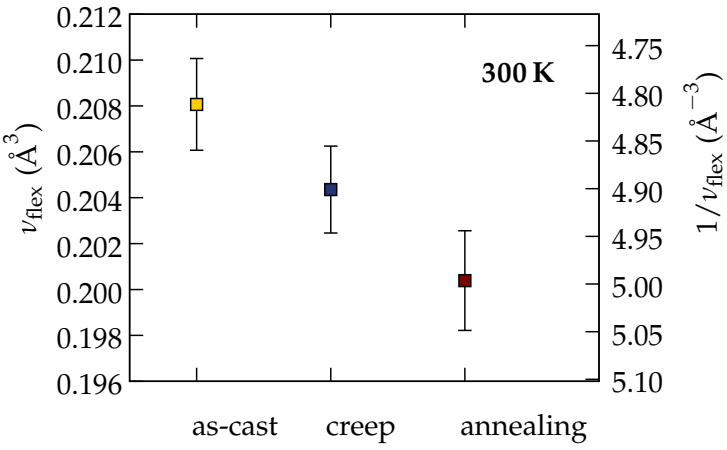

FIGURE 32: Mean flexibility volume for the as-cast, annealed and creep sample measured at 300 K.

The atomic flexibility volume (Eq. 1.3), which is correlated to soft-spots present in the sample,[81] should give a clearer picture. The sample average of the per-atom values obtained at 300 K in the as-cast, crept and annealed samples is given in Figure 32. The thermal mean squared displacement has been averaged over 50 time intervals of 1 ps simulated in the microcanonical ensemble, where the samples have been previously equilibrated at 300 K. The flexibility volume in the unrelaxed as-cast sample is highest and, indeed, when comparing the crept and annealed samples, the flexibility volume is lowest in the annealed sample, which matches with the order of the potential energies of the samples.

What is the mechanistic picture behind the here observed anisotropic mechanical response? Structural anisotropy in MGs caused by mechanical deformation has been reported before in experimental studies using X-ray diffraction to measure the structure function and pair density distribution function.[11,63,174,175] In our case, however, the analysis of the RDFs does not reveal any differences [cf. Figure 35]. One might suspect that the previous straining in z-direction causes a bond-elongation in that direction. Thus, we also examined the projection of the neighbor bonds onto the z-axis, but still, no differences in the distribution of bond lengths could be detected. To ensure, that these subtle details are not swallowed in the noise, we repeated the same analyses for the bond distributions of the FI-clusters [cf. Figure 35(a) and (b)], but the RDFS of the FI do not hint towards a bond-length change either. Here, we can thus preclude that the anisotropic mechanical response is rooted in a changing bond distribution.

Nonetheless, the remaining plastic creep deformation observed here is as high as 3%, as visible for sample C4 in Figure 27. Hence, significant STZ activation had to occur in the crept samples. When unloading not all of them can be reversed leaving residual stresses behind. The observed higher yield strength despite the energetically less relaxed material state could also be explained in the framework of the PEL. We suggest that the creep prestraining introduces a bias in the PEL and causes an anisotropy in the glass, that is not visible by the characterization meth-

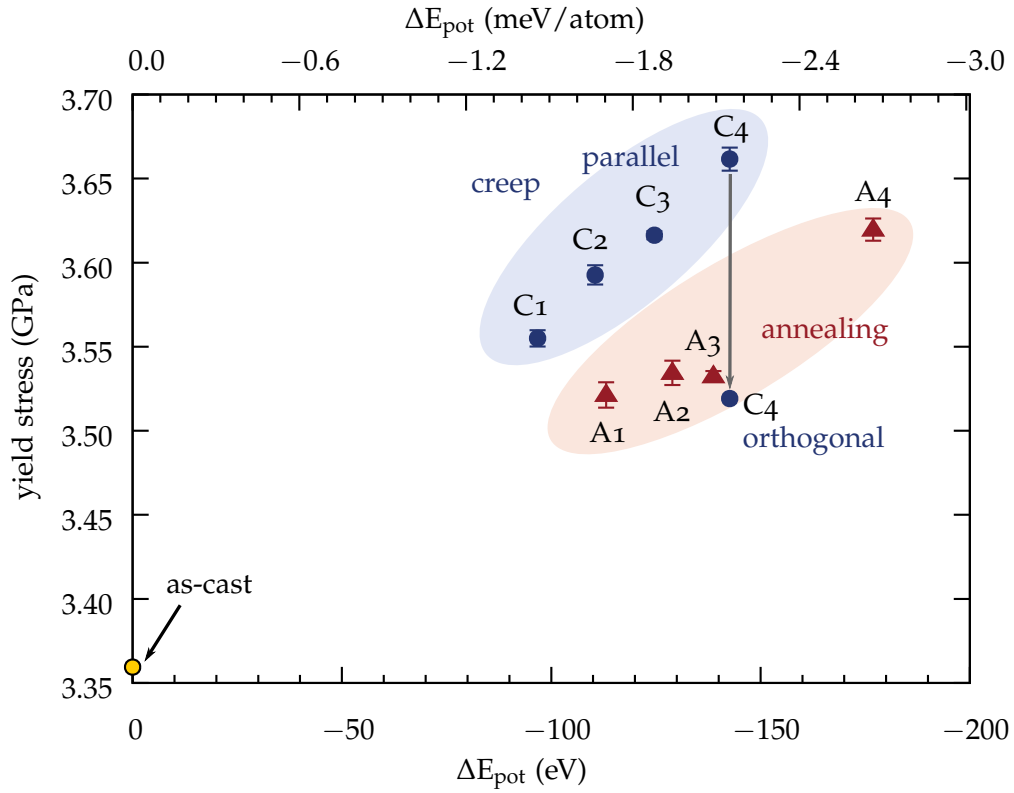

FIGURE 33: Comparison of the yield stress and potential energies of the as-cast, crept and annealed samples measured at 50 K as already presented in Figure 29. In addition, the yield stress of sample C4 tested under uniaxial tension along the y-direction, i.e. orthogonal to the creep prestraining direction, is shown.

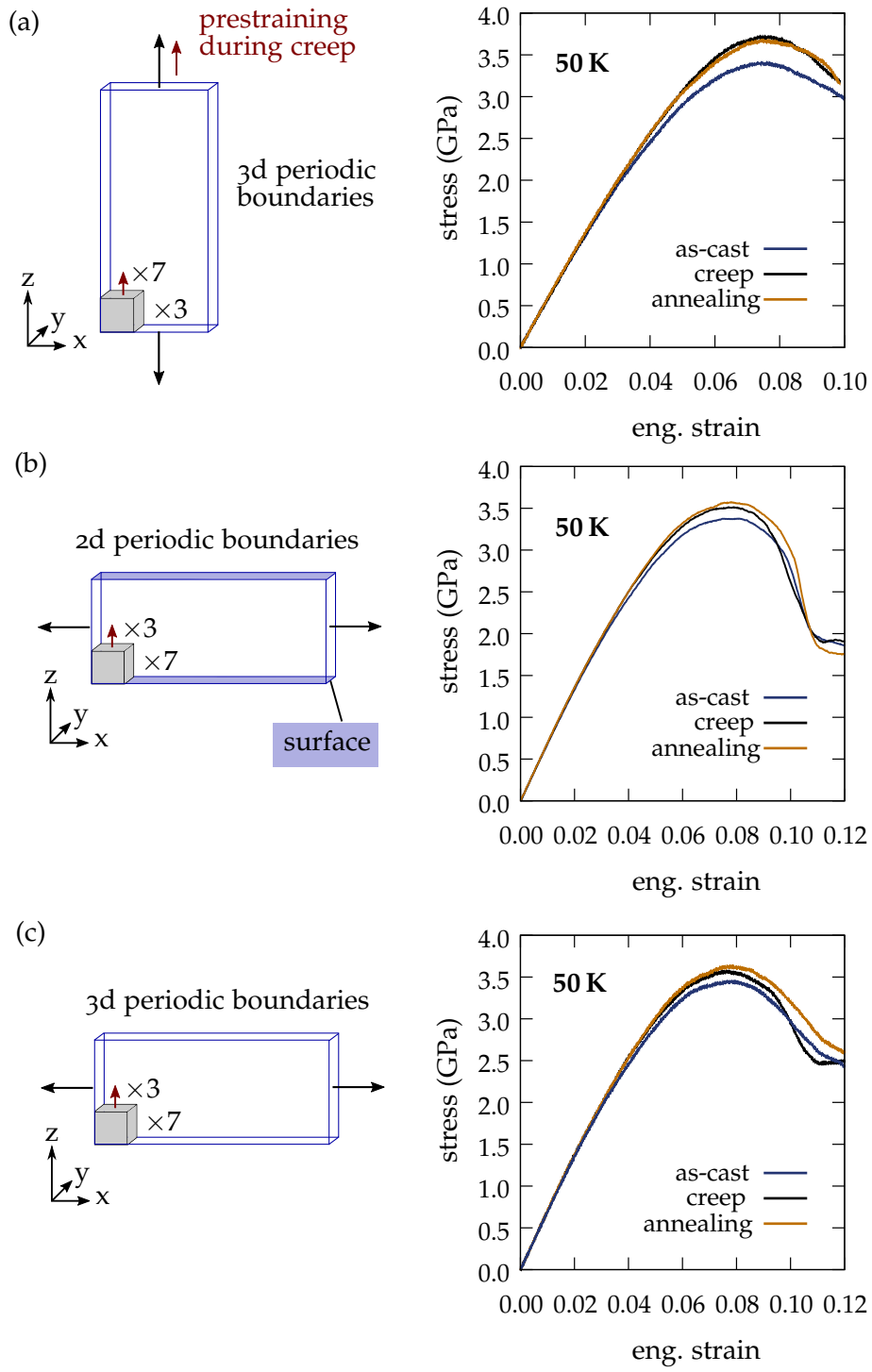

FIGURE 34: Tensile tests of the as-cast sample and after different creep and annealing times with (a) 3*d* periodic boundary conditions and the tensile load parallel to the prestraining (b) 2*d* periodic boundary conditions and the precursor replicated 7 times in *x*-direction, and (c) 3*d* periodic boundary conditions and the precursor replicated 7 times in *x*-direction. For (b) and (c) the tensile load was applied perpendicular to the prestraining direction.

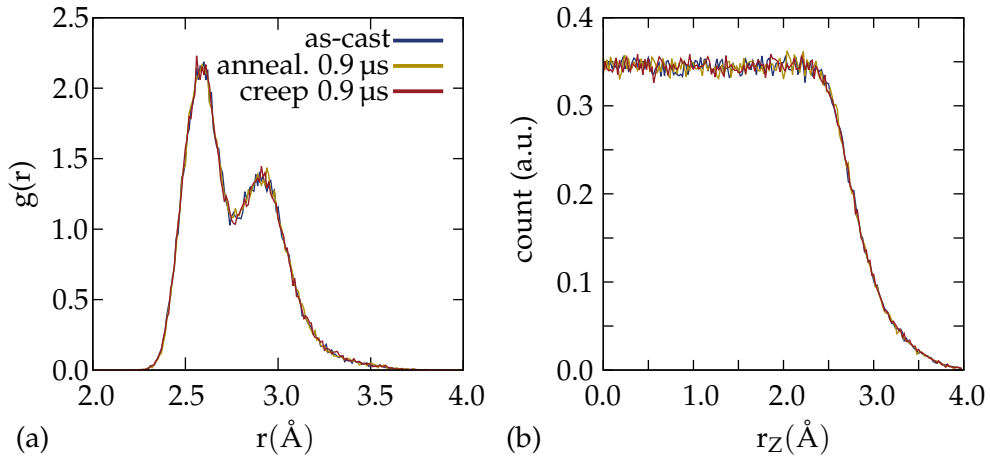

FIGURE 35: Comparison of the RDF of the Cu-centered $\langle 0,0,12,0\rangle$ clusters in the as-cast sample and the samples annealed for 500 ns with and without load. (b) Projection of bond-length distribution onto z-axis.

ods we used here. Assuming an initially broad distribution of activation barriers for STZs in the as-cast glass, we posit that easily activated barriers are exhausted during the creep pretreatment, which leads to a strengthening of the glass in the subsequent deformation experiment. We expect this effect to be visible as a shift in the STZ barrier distribution. The distribution could be measured by the activation relaxation technique (ART) as e.g. described in Refs. 69 and 167. Determination of the two spectra of the annealed and crept samples warrants further study.

5.6 CONCLUSION

We have shown that even at temperatures well below T_g, long-time annealing under both load-free and constant uniaxial loading conditions causes aging accompanied by an enhanced relaxation. These processes occurred at timescales far beyond 100 ns, i.e. on time-scales that are usually not assessed during MD-simulation of MGs. In general, we observe that MG samples that were relaxed longer, exhibited a higher strain localization and higher yield stresses. In the deeply relaxed glasses, strain localization in a major shear band could even be observed at room temperature, which could help bridging the gap between experimental and simulation studies. In addition, we were able to manipulate the relaxation process by inducing creep deformation. Such a pretreatment did not enhance the relaxation process but introduced an anisotropy in the glass, such that the yield strength under tensile load parallel to the prestraining direction was even further increased. We suggest that this effect is caused by a shift in the STZ barrier distribution.

6

CYCLIC LOADING

In the previous chapter we have shown that long-time annealing at $0.65T_g$ under an elastostatic uniaxial load of 750 MPa causes aging accompanied by anisotropic mechanical behavior. In order to avoid this anisotropy a different loading scenario may be considered, e.g. a hydrostatic stress environment. Moreover, the benefit of a load cycling between tensile and compressive hydrostatic stresses is that in theory the average stress should be zero. Such loading conditions have been used before to study aging of a potassium sodium alumosilicate glass by means of MD.[176] In the case of this network glass, the motivation to use cyclic stress-perturbation was to accelerate the aging process and be able to predict long-time relaxation from MD simulations, which was otherwise not possible during simulations at ambient pressures and temperatures. The atomic structure of our MG, however, is very different from those of rigid network glasses and we showed that relaxation processes already occur on timescales of a few hundred nanoseconds during stress free annealing [cf. Ch. 5]. We thus expect to be able to reduce the aging simulation times through the application of a cyclic elastostatic load.

6.1 SIMULATION SETUP

The simulation setup is schematically shown in Figure 36. The same cubic sample from Ch. 5, denoted as "as-cast", is heated to 580 K with a heating rate of $\dot{T} = 0.1\,\mathrm{K/ps}$ and subsequently subjected to an isostatic load cycling of ± 750 MPa using the Nosé–Hoover thermo- and barostats. Each load cycle consists of 1 ns tensile loading and 1 ns compressive loading. This cycle procedure is repeated up to 250 times.

Then, analogous to the experiments in Ch. 5, the cycling is interrupted after 300 ns and 500 ns and these samples are quenched to 50 K with $\dot{T} = 0.1\,\mathrm{K/ps}$ and further equilibrated. The cubic precursors are again replicated to generate larger glass slabs of $30 \times 10 \times 70\,\mathrm{nm}^3$ that are used for low-temperature tensile testing under $2d$-periodic boundary conditions with a constant engineering strain rate of $\dot{\epsilon} = 10^8/\mathrm{s}$.

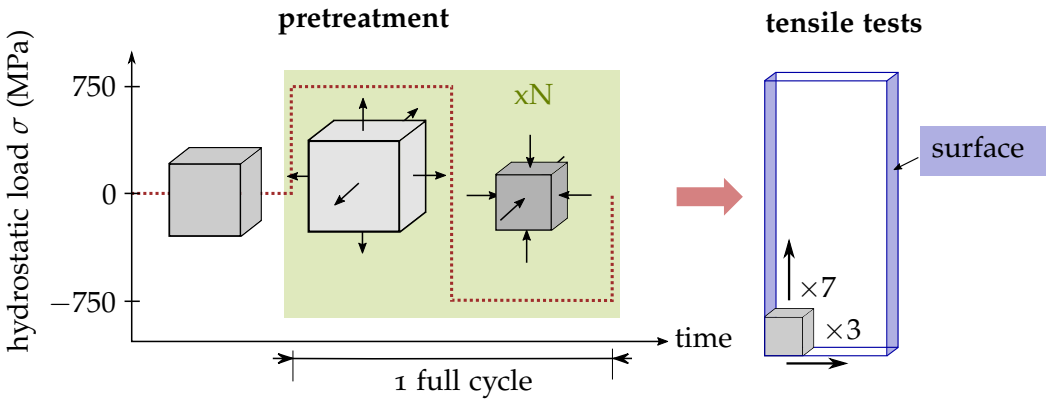

FIGURE 36: Hydrostatic cyclic loading procedure at $T = 580\,\mathrm{K}$. The stress conditions are switched between tensile and compressive hydrostatic loading. After this pretreatment, the sample is replicated and tested in conventional tensile tests at 50 K and room temperature.

6.2 ENERGY RELAXATION

Figure 37(a) compares the evolution of the potential energy during 500 ns of annealing and cyclic loading at $T = 580\,\mathrm{K}$. For the cyclic loading, each data point corresponds to the energy at the end of a 1 ns load sequence. What is striking is that the potential energy curves of the compressed and tensioned samples do not coincide. In the ideal elastic regime, the elastic strain energy contribution should both be positive and both curves should have the same offset with respect to the

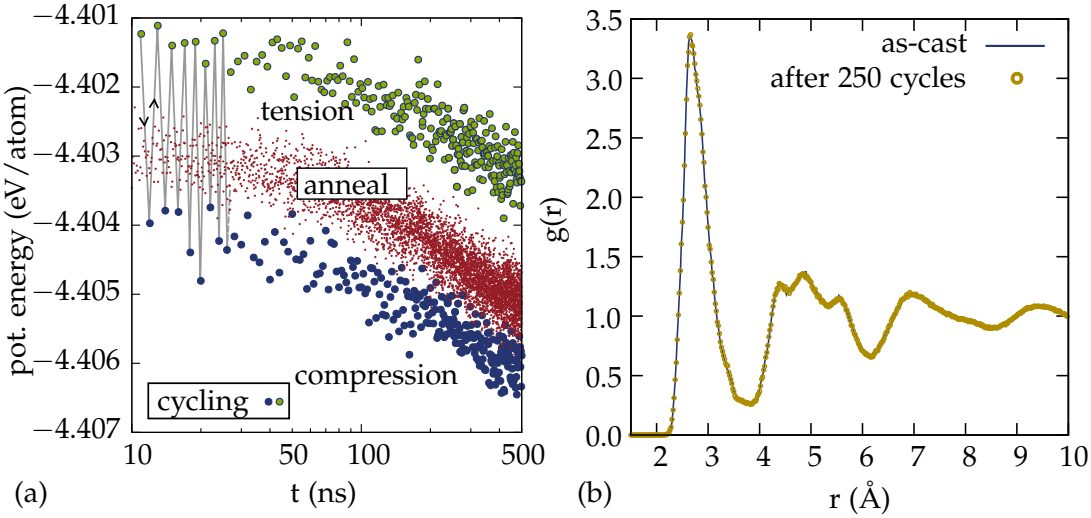

FIGURE 37: Evolution of the potential energy during annealing (red data points) and cyclic loading (blue data points) at $T = 580\,\mathrm{K}$. Each point represents the potential energy after 1 ns of static loading with 750 MPa or −750 MPa. (b) Radial distribution functions before and after 250 pressure cycles (obtained after static minimization).

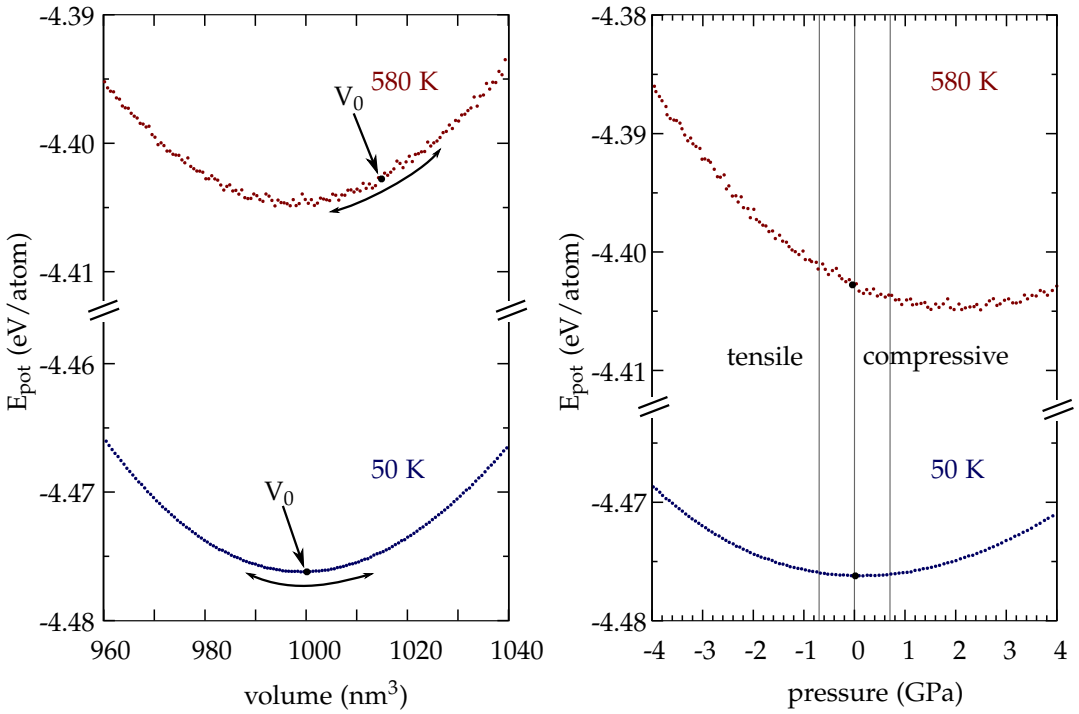

FIGURE 38: (a) Potential energy-volume dependence of the as-cast sample at 580 K and 50 K. The initial volumes are marked in black. (b) Corresponding energy-pressure dependence.

stress-free annealed state. Moreover, the potential energies of the compressed samples are even lower than in the stress-free annealed case. An explanation for this behavior can be found in the dependence of the potential energy on volume and pressure as shown in Figures 38(a) and (b). The data points have been obtained by incrementally rescaling the dimensions of the simulation cell at 580 K (red curve) and 50 K (blue curve), respectively. After each volume change 20 ps of equilibration have been simulated in the canonical ensemble. The black points mark the initial configuration in each case. At 50 K the equilibrium configuration corresponds to the minimum of the potential energy, see Figures 38(a). Any rescaling of the volume brings the sample out of its minimum energy configuration and the corresponding pressure vs. potential energy curve is symmetrical, visible as blue curve in Figure 38(b). At 580 K however, the initial configuration does not coincide with the minimum of the potential energy–volume or potential energy–pressure curve any more. This shift in the potential energy is due to the entropic contributions. Increasing the volume leads to to a potential energy increase and decreasing the volume causes the potential energy to decrease. We observe that the volume change during pressure application is fully reversible. Once the pressure is removed the sample returns to its initial volume with the corresponding higher potential energy state. This is not at odds with thermodynamics since actually, one would have to look at the Helmholtz free energy of the samples, i.e. the thermodynamic potential of

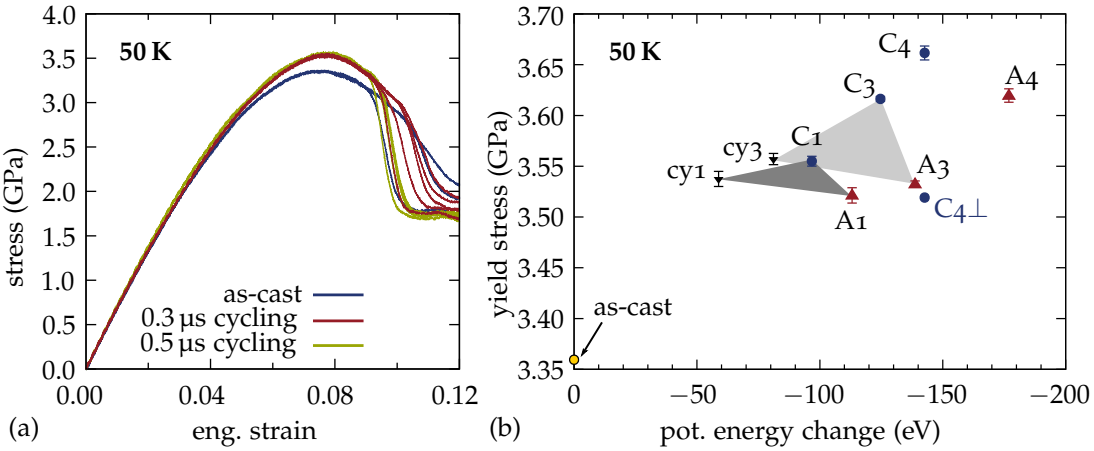

FIGURE 39: (a) Comparison of tensile tests at $T = 50\,\mathrm{K}$ for the as-cast sample and samples that have been pressure-cycled for 300 ns and 500 ns. (b) Yield-stress vs. potential energy change with respect to the as-cast sample comparing different annealing, creep and cyclic pretreatment times. The yield stress increase due to cyclic loading ranges in those measured for annealing and creep treatments. The labels stand for the different pretreatment methods and times "cy" stand for cyclic loading, "C" for creep, and "A" for isothermal annealing, and the number denotes the pretreatment time (1) 300 ns, (3) 500 ns and (4) 900 ns in analogy to the nomenclature in Ch. 5.

the canonical ensemble. Of course its minimum doesn't have to coincide with the minimum of the potential energy, especially not at high temperatures.

What is the effect of this cycling procedure on the atomistic structure of the MG? The RDF in Figure 37(b) at least shows no structural changes. The Voronoi analysis of the quenched samples, however, reveals that the number of FI clusters is increased from 19.3% to 20.1% after 500 ns of cyclic loading. Thus, the pretreatment presented here should also result in increased mechanical strength with respect to the as-cast sample. In the next section, we will reveal the influence of the cyclic loading on the low-temperature mechanical properties.

6.3 CONVENTIONAL TENSILE TESTING

Figure 39(a) shows the results of the tensile tests at 50 K for glass slabs generated from precursors after two different cycling times, 300 ns and 500 ns. Again, five independent tensile tests per sample set have been performed. As already observed and explained in the previous chapter, the yield-stress is reproducible and the flow-stress is subject to statistics. Much like the annealing and creep pretreatments, cyclic loading at 580 K generally improves the low-temperature mechanical strength: With respect to the as-cast sample, the pressure-cycle pretreatment increases the 50 K yield-stress by 178 MPa after 300 ns and 197 MPa after 500 ns.

How does this compare to stress-free annealing or uniaxial creep? Figure 39(b) summarizes the following observations: On the one hand, when comparing the cor-

(a) **pretreatment: annealing 500 ns**
50 K - 12% eng. strain

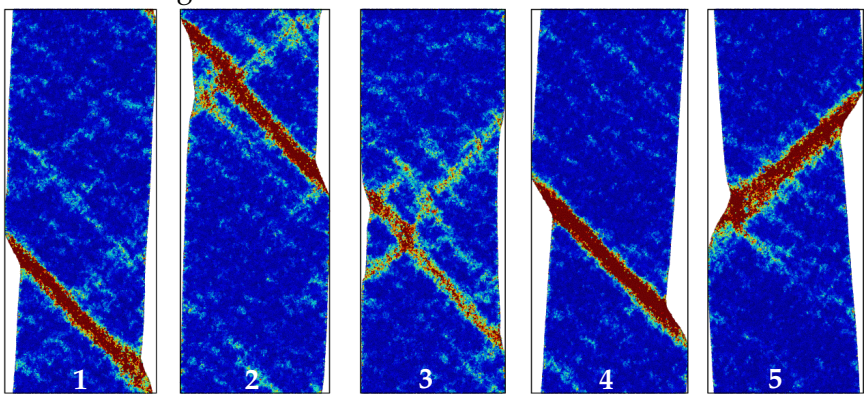

(b) **pretreatment: cyclic loading 500 ns**
50 K - 12% eng. strain

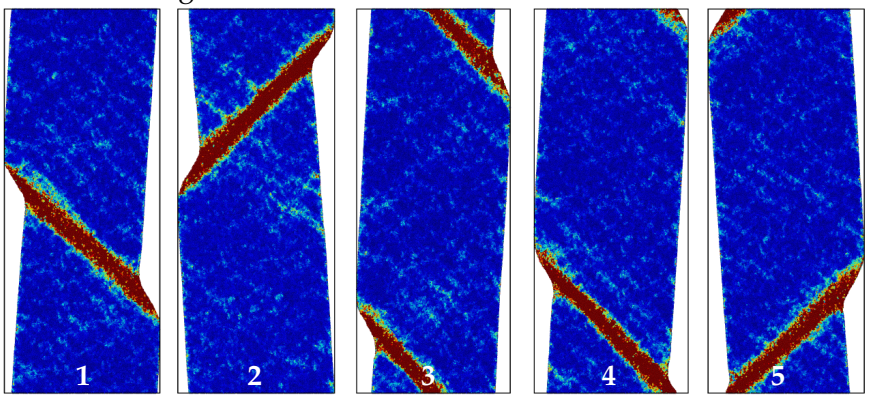

300 K - 12% eng. strain

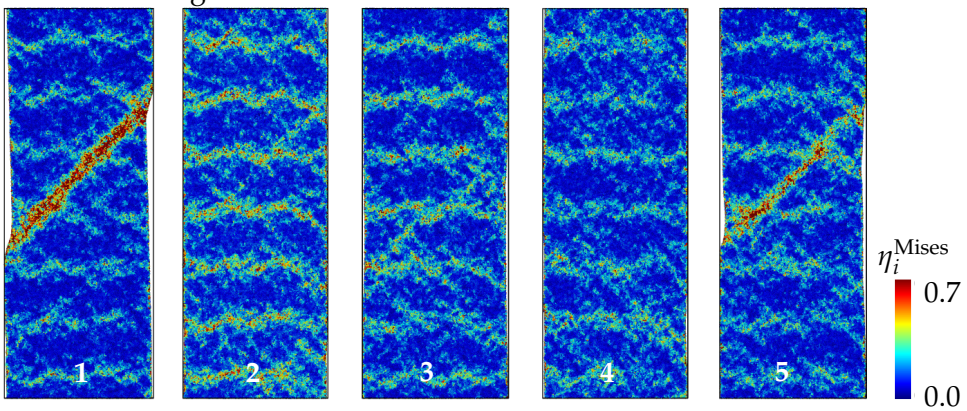

FIGURE 40: Snapshots of the atomic configurations at 12% macroscopic strain colored according to the local atomic von Mises shear strain. (a) The precursor has been annealed at 580 K for 500 ns. Shown are five independent simulation runs performed at 50 K. (b) The precursor has been treated by pressure cycling at 580 K. Depicted are five independent simulation runs performed at 50 K (top row) and 300 K (bottom row).

relation of the potential energy reduction with the yield stress increase due to the different pretreatments, the cycled samples exhibit higher energies than their crept or annealed counterparts. The energy values have been measured after quenching and statically relaxing each precursor sample. The yield stress values, on the other hand, range in between those obtained after creep and annealing pretreatments. These results suggest that similar to the case of uniaxial creep loading, some low energy barriers disappear during cycle loading and the distribution of energy barriers for STZ activation is shifted to higher values, such that the cycled MG exhibits a higher strength. The main difference between hydrostatic cycling and uniaxial tension is that no anisotropic mechanical behavior should result from the hydrostatic treatment. Moreover, we could show that structural relaxation can already be achieved at 580 K under load-free conditions. Thus, it is not too surprising that the absolute differences in yield stress after the thermal and the thermo-mechanical treatments are small, i.e. < 100 MPa.

Finally, from the results in Ch. 5 we know that the shape of the stress–strain curves may not be a sufficient criterion to distinguish between homogeneous and inhomogeneous deformation modes. For that reason, we present snapshots of the atomic configurations at 12% macroscopic strain during tensile testing in Figure 40, where atoms are color coded according to the local atomic von Mises strain. Figure 40(a) shows the samples from five independent tensile tests that have been annealed for 500 ns at zero-load as a reference. In all five samples, a major shear band is formed. Samples 2 and 3, exhibit additional shear band nuclei, that are on the verge of forming a continuous band. The results of the 50 K and 300 K tensile tests after the pressure-cycling treatments are summarized below in Figure 40(b). Again, in all five independent simulation runs a major shear band is formed. As compared to the load-free annealed samples, it seems that less STZ activity is occurring in the matrix. Even at 300 K, shear bands can be observed in two out of five cases (at 12% macroscopic strain). The chosen constant engineering strain rate of $\dot{\epsilon} = 10^8$ /s is sufficiently slow to observe shear band formation in these samples, which was not the case for the less-relaxed as-cast sample tested at 300 K (see Figure 24 in Ch. 5).

Generally, the shear bands that formed during tensile testing at 50 K are thicker in the pretreated samples as compared to the as-cast state. As for the different pretreatment types, it might be rather speculative to correlate differences in the shear band width with the type of pretreatment. Yet, we can conclude that any of the three treatments used here lead to deeply relaxed MG states, which in turn allows to reduce the strain rates necessary to observe shear band formation in MD-simulations - even at room temperature.

6.4 CONCLUSION

In conclusion, sub-T_g hydrostatic cyclic loading within the elastic regime caused the MG to age. As opposed to simulation results obtained for network glasses, however, no speed up in the relaxation dynamics did occur. On the contrary, the

hydrostatic pressure cycling resulted in a slightly rejuvenated sample with respect to the stress-free long-time annealed case. In analogy to the cycling and annealing pretreatments studied in Ch. 5, the aging process manifests itself in improved mechanical strength and increased strain-localization during 50 K tensile testing. The observed yield stress increase with respect to the as-cast state could be correlated with an increased fraction of FI clusters. The effect is not as pronounced as in the case of uniaxial creep loading, but the advantage of using hydrostatic stress states is that no anisotropic mechanical behavior is induced.

Part III

METALLIC GLASS - CRYSTAL COMPOSITES

7

INFLUENCE OF SECONDARY PHASE TOPOLOGY

The results presented in this chapter have been published in Ref. 177.

So far, we discussed different thermo-mechanical pretreatments of the homogeneous $Cu_{64}Zr_{36}$ MG and their impact on the low-temperature mechanical strength. Another common strategy to improve the room-temperature mechanical properties of MGs is to reinforce them with crystalline secondary phases. Typical crystalline composite microstructures involve dendritic crystalline phases which percolate the glass phase.[6,178] Besides an increase in yield strength, secondary phases can be beneficial to the ductility by promoting a more homogeneous deformation behavior through the formation of multiple shear bands. In these composites this is the case, since shear bands are spatially confined and are arrested at the glass-crystal interfaces, causing new ones to nucleate. However, with decreasing volume fraction and size of the secondary phase the deformation mechanism changes. For nano-sized precipitates, e.g., different interaction scenarios between shear bands and the precipitates have been observed. By means of MD-simulations of $Cu_{64}Zr_{36}$ Brink *et al*. established that depending on the crystallite size and distribution either shear band wrapping, blocking or cutting is favored.[9]

All the above findings have been obtained during conventional loading conditions at low temperatures. In the SCL state ($>T_g$) the presence of crystalline precipitates can have an impact on the rheological behavior.[134–136] During thermoplastic deformation of a Ti-Cu based MG containing micrometer-sized B2 particles, e.g., an increased viscosity could be correlated with larger volume fractions of secondary phase. FEM-simulations revealed that the viscosity increase was caused by sluggish flow in the vicinity of the particles.[136] However, the effect did only play a role for threshold volume fractions of secondary phase larger than 15%.

At intermediate temperatures and low stresses, in contrast, the deformation behavior of MG–crystal composites has not received much attention so far. If the viscosity is altered by the presence of glass-crystal interfaces, it stands to reason that the creep behavior is also affected. In this chapter we study $Cu_{64}Zr_{36}$ MG-matrix composites with various geometries of an embedded crystalline phase in order to asses the impact of secondary phases on the creep behavior. In experimental Cu–Zr glasses, B2 CuZr precipitates can be obtained by annealing procedures and during deformation[179–182] and are thus chosen as a representative crystalline phase for our model systems. The B2 phase is brittle and dislocation activation is hindered by the high antiphase-boundary energy. Indeed, in previous simulations

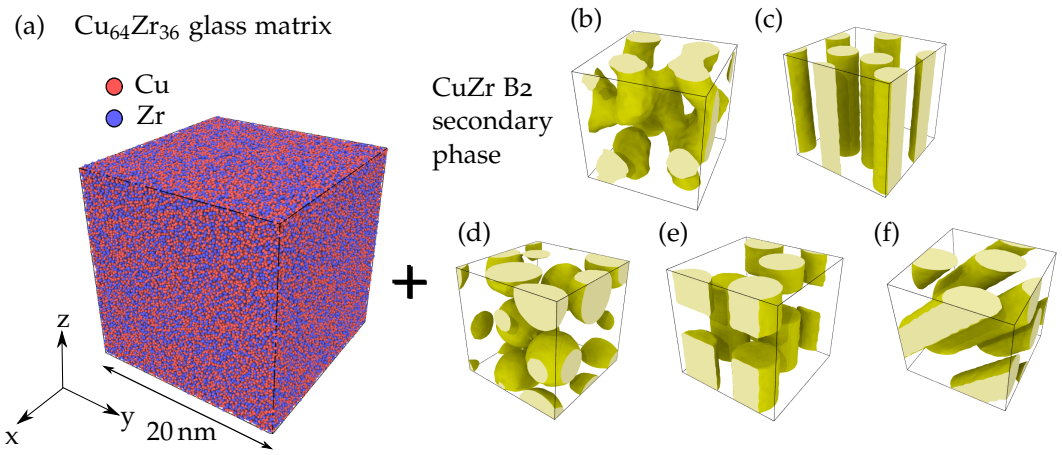

FIGURE 41: Snapshots of the composites from the sample series with $f = 30\,\%$ and $\phi = 210\,\mu m^{-1}$. (a) The glass sample. Color coding: Blue and red represent Cu and Zr atoms, respectively. (b)–(f) Surface meshes of the secondary CuZr B2 phases that are inserted into the glass matrix.

using the interatomic potential by Mendelev, this phase was shown to only respond elastically when being part of a composite.[9] Analogous to crystalline materials, the question arises if mechanical reinforcement against creep is possible by introducing a stronger non-yielding secondary phase, e.g., by combining a glass matrix with a crystalline phase. Therefore, our systems are a mixture of a crystalline phase with high yield stress, that only reacts elastically, combined with an amorphous phase. As explained in Ch. 2, such composite models were also proposed for ceramics,[130] and are therefore relevant models even beyond metallic systems.

7.1 SIMULATION SETUP

The straight-forward way to model glass–crystal composites is to insert the secondary phase and delete all overlapping atoms, as described in the Methods section 3.3. Figure 41 shows a snapshot of the homogeneous $Cu_{64}Zr_{36}$ metallic glass and the different secondary phase topologies used in this study. The matrix glass, a cubic box of dimension $20 \times 20 \times 20\,nm^3$ of $Cu_{64}Zr_{36}$, is obtained by quenching from the melt with 0.01 K/ps at ambient pressure. This glass is then equilibrated at 300 K, again at ambient pressure, for 1 ns. The composites are created starting from the glass matrix, by cutting out the desired geometry for the secondary phase and filling the empty space with a B2 crystal oriented with the $\langle 100 \rangle$ directions along the Cartesian axes. The lattice constant for B2 was obtained using a simulation at 300 K. After assembly, the composites are relaxed for 1 ns at 300 K and ambient pressure.

We start with an interpenetrating, continuous network, depicted in Fig. 41(b), which serves as a model for percolating crystalline structures embedded in a glass. Such structures resemble those that have been proposed, e.g., for phase-separating

oxide glasses.[130] The networks in our simulations were obtained by creating a mask using simulated spinodal decomposition of a binary alloy which has been used to model nanoporous metallic models as in Ref. 149. The two components are chosen with volume fractions of $f_A = 0.3$ and $f_B = 0.7$. The system completely decomposes into a network (A) and a matrix phase (B). Then, the network phase starts to coarsen. The network structure is extracted from four different evolution stages of this coarsening process and used as a mask. Thus, the masks have the same volume fraction, $f = 0.3$, but different surface areas. We use those two parameters to describe the geometry of the secondary phase: The crystalline volume fraction f and the specific interface area ϕ. We define the latter as the surface area of the free-standing crystalline phase divided by the total volume of the composite:

$$\phi = \frac{A_{\text{interface}}}{V_{\text{tot}}} \,. \tag{7.1}$$

The surface area is determined using a surface-mesh construction by Delaunay tessellation[163] as implemented in the software OVITO.[148] For the networks, we choose four molds at different stages of the spinodal decomposition with specific interface areas $\phi_1 = 170/\mu\text{m}$, $\phi_2 = 210/\mu\text{m}$, $\phi_3 = 320/\mu\text{m}$ and $\phi_4 = 410/\mu\text{m}$.

In order to understand the influence of geometry in more detail, we also employed simpler geometric shapes, such as continuous nanowires in various orientations (Figs. 41(c) and 41(f)), non-percolating nanorods (Fig. 41(e)), and spheres (Fig. 41(d)). These were prepared using the same volume fraction and specific interface areas as the network composites.

For the creep simulation, we choose a temperature of 500 K, which corresponds to about $0.6\,T_g$. The samples are heated to the target temperature with a heating rate of 0.1 K/ps. Creep tests are performed by instantaneously applying a constant tensile stress in z direction for 40 ns while keeping the other dimensions at ambient pressure. The creep rate is obtained through a linear fit of the creep simulation data between $t_1 = 25$ ns and $t_2 = 40$ ns. Furthermore, a load-cycling test is simulated at 500 K by instantly unloading the samples for 20 ns and subsequently reloading for 20 ns.

7.2 PLASTIC DEFORMATION OF GLASS–CRYSTAL COMPOSITES

As a first step, we perform tensile tests on the different samples to ascertain that we choose a stress regime below yield for the creep tests. Figure 42 shows the stress-strain curves obtained by tensile tests of bulk $Cu_{64}Zr_{36}$ glass, single-crystalline B2 CuZr, and the composites with a network structure [cf. Fig. 41(b)]. We perform strain-rate-controlled tensile tests at $T = 500$ K with a constant engineering strain rate of $\dot{\epsilon} = 4 \cdot 10^7/\text{s}$. The tensile direction coincides with the [001]-orientation of the single-crystal. It can be seen that the Young's moduli of the glass and crystal are very similar, but the yield-stress of the glass is far exceeded by the crystal's. Furthermore, it is evident that the four composites exhibit lower elastic moduli than their pure constituents, even though they all contain the same volume fraction

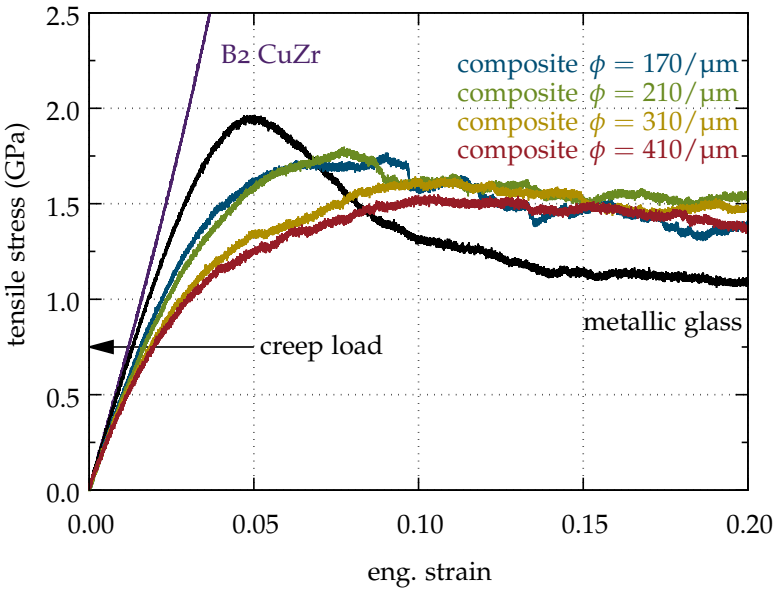

FIGURE 42: Tensile tests of the homogeneous glass, the single crystalline B2 CuZr, and the four composites with network microstructure at 500 K. For all composites and the glass, a stress of 750 MPa is well below the yield stress.

of crystalline network phase, $f = 30\%$. This suggests that the specific interface area plays a strong role in the mechanical properties. The higher the specific interface area ϕ, the lower is the composite's mean elastic modulus. On the other hand, the composites have a higher flow stress and do not show the stress overshoot typical for a glass. Such a "flattening" of the stress response has also been observed in other glasses with a microstructure containing weakened interfaces, such as NGs.[83,98] From these results we can conclude that $\sigma = 750\,\text{MPa}$ is an appropriate stress level for creep testing at $T = 500\,\text{K}$, since it is below the individual yield stresses of both the composite structures and the homogeneous glass, but high enough to observe creep on MD timescales. The crystalline phase is still in the linear elastic regime up to strains of at least 5%.

7.3 CREEP SIMULATIONS

7.3.1 *Homogeneous glass and interpenetrating network secondary phase*

Instead of strain rate controlled experiments, we now switch to creep conditions under static uniaxial loads. Figure 43 shows the creep curves of four network composites with topologies as depicted in Fig. 41(b), with the parameters established above. Additionally, we show the creep curve of the homogeneous glass. At the simulation times available, we were never able to observe failure. The creep curve rather suggests viscoelastic behavior which appears as a mix of creep stages I and II. Analogous to Ch. 4 we simply extract the creep rate in all cases from the slope in the time range between $t = 25\,\text{ns}$ and $t = 40\,\text{ns}$ to obtain comparable data. The creep strain depicted in the following figures is always the true strain, $\epsilon_{\text{true}} = \ln(L_z/L_{z0})$,

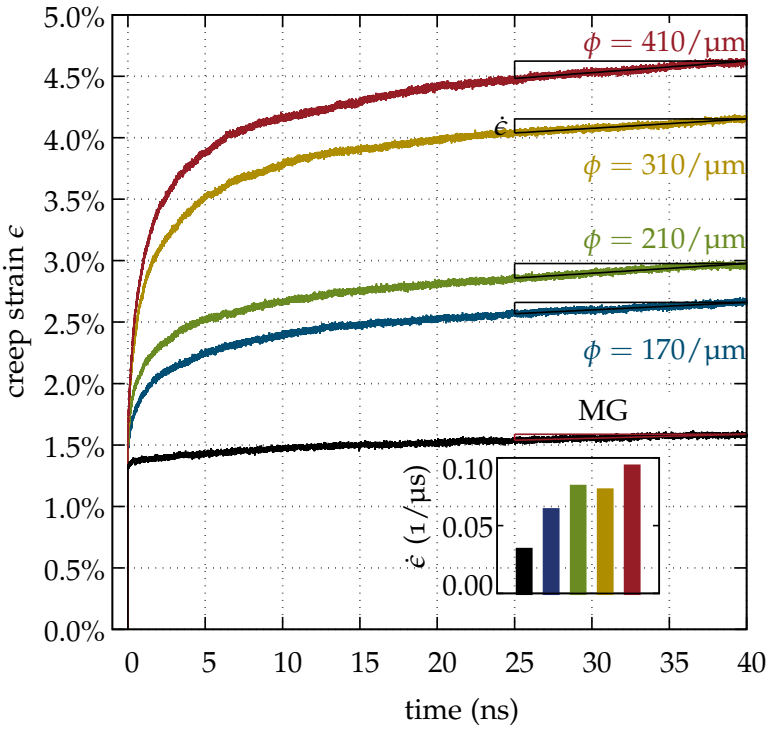

FIGURE 43: Dependence of true strain on loading time during the creep test of the composites with crystalline interpenetrating network microstructure. The creep curve of the matrix glass is shown in black as a reference. The inset shows the different creep-rates of the samples fitted between $t = 25\,\text{ns}$ and $t = 40\,\text{ns}$.

where L_z is the box length in z direction. In this way, we ensure that the fitted creep rates are independent of the initial box length L_{z0} in loading direction.

Moving on to the composites, we observe that the creep behavior's temperature dependence also resembles the behavior described by Argon, cf. Fig. 44. Surprisingly, Fig. 43 reveals that the composites exhibit much higher creep rates than the homogeneous glass at the same temperature. Furthermore, we note that the larger the specific interface area ϕ, the higher is the total true creep strain after 40 ns, which is also reflected in the inset to Fig. 43, which shows that the creep rate increases with ϕ. For these glass–crystal composites, composed of viscous glass phase and a stronger crystalline phase that cannot exhibit dislocation activity under the present testing conditions, we would have expected a decrease in the creep rate. The observed increase seems counter-intuitive, considering the mix of a time-dependent deforming phase with a significant volume fraction of non-deformable phase. In fact, we showed above that at the creep strain levels obtained here in the composites, the crystalline phase only deforms elastically. Thus the creep behavior of the composite must be governed by the glass phase.

How is it possible that introducing the network phase, makes the glass more prone to creep? A first explanation can be found in the elastic moduli of the glass and crystal. While they do not differ much, the composites are less stiff than the homogeneous glass (see Fig. 42). Thus, we can infer that the composite interfaces must be weaker than the surrounding matrix. To understand the influence of the interface, we need to study the creep deformation in the glass and crystal phase at the atomic level. Figures 45(a)-(e) shows snapshots of the atomic strain in the ho-

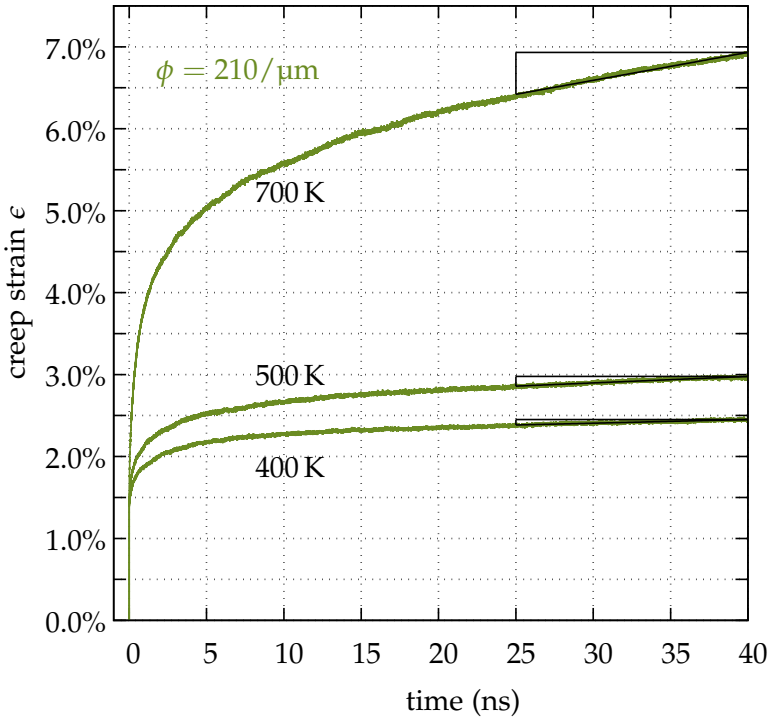

FIGURE 44: Dependence of the creep behavior on temperature for the composite with a network structure such as in Fig. 41(b) with $\phi = 210/\mu m$. The creep curves have been obtained for three different temperatures, 400 K, 500 K and 700 K. Both the total creep strain and creep rate strongly increase with temperature.

mogeneous glass and composite structures. The color coding indicates the amount of atomic strain experienced by the atoms. We use two different color maps for the atoms that initially belonged to the glass matrix or the B2 crystal. The results of this strain analysis support the hypothesis that the crystalline phase only deforms elastically since we could not observe any dislocation activity. Furthermore, Figs. 45(b)-(e) reveal that the deformation is mostly localized in the interface. For very high specific interface areas ($\phi = 410/\mu m$), almost the complete glass matrix can be considered as an interface region because of the small distance between the two interfaces. The pure glass, however, exhibits a homogeneous distribution of STZs without the formation of shear bands, which resembles the non-interface glass regions in the composites. This suggests that the glass–crystal interface can be viewed as a weak interphase, where the effective activation barrier is lower than in the surrounding glass. Therefore, STZs are more easily activated in the interface than in the bulk glass and a closer look at the interface is warranted. For this, we performed a Voronoi analysis of the atoms in the interface and glass phase. The interface is defined such that it includes glass atoms at the direct glass-crystal interface and their neighbors in the glass phase within a cutoff of 3.6 Å. Figure 65(f) exemplarily shows the Voronoi statistics of the Cu atoms in the glass and interface phase of the sample with network microstructure $\phi = 170/\mu m$, both before and after 40 ns of tensile creep testing. Prior to the Voronoi tessellation, an energy minimization using molecular statics has been performed. Here, only polyhedra that either occur more often than 2% in the glass phase or interface phase are shown, the remaining polyhedra are summarized under the category "others". When compar-

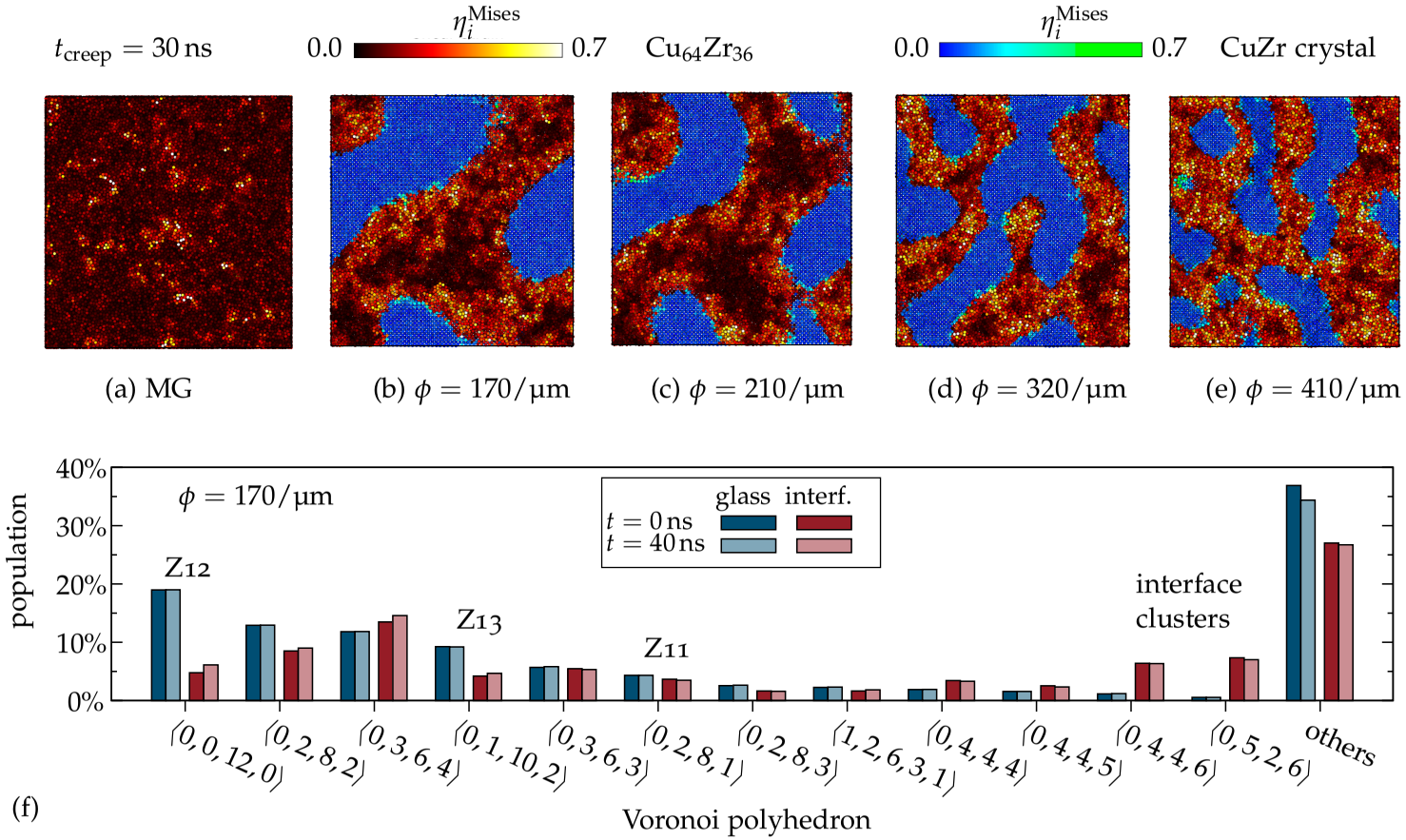

FIGURE 45: Snapshots of (a) the MG and (b)–(e) composites with secondary phase network ordered by increasing interface area after $t = 30\,ns$ creep testing. The atoms are color coded according to the atomic shear strain, using two different color maps for the glass and the crystalline phase. (f) Voronoi statistics of the Cu atoms in the interface and glass matrix. Only Voronoi polyhedra that occur more often than 2% are shown, the rest are summarized as "others". The energetically favorable Cu clusters with an eleven-fold, twelve-fold and thirteen-fold coordination are indicated as Z11, Z12 and Z13.[183] The 12-fold signature motif $\langle 0, 0, 12, 0\rangle$ and its defective variant $\langle 0, 2, 8, 2\rangle$ are the most prominent clusters in the glass matrix, but are severely reduced in occurrence in the interface. The $\langle 0, 4, 4, 6\rangle$ and $\langle 0, 5, 2, 6\rangle$ clusters appear predominantly at the immediate glass–crystal interface.

ing the most prominent Cu centered polyhedra in the interface and glass phases, it is evident that the geometrically favorable motifs, also called Z-clusters,[183] are abundant in the glass. This is especially visible for the copper-centered icosahedra (Z12), and their defective version $\langle 0, 2, 8, 2\rangle$. Their fraction is significantly reduced in the interface, where more geometrically unfavored motifs (GUMs),[12] such as the $\langle 0, 3, 6, 4\rangle$ polyhedron, can be found. Additionally, 13-fold $\langle 0, 5, 2, 6\rangle$ and 14-fold $\langle 0, 4, 4, 6\rangle$ clusters appear at the immediate glass-crystal interface. The zirconium-centered polyhedra exhibit similar trends and are omitted here. In total, these results indicate a weakened glass structure in the interface. This is also supported by the lower number density of the interface of 50.1 atoms/nm^3 as compared to 63.3 atoms/nm^3 in the glass matrix. Thus, there is excess volume in the interface. Additionally, Fig. 45(f) shows that the Voronoi statistics of the glass do not change during the 40 ns of creep deformation. In the interface, there is a slight increase in occurrence of Z12 and Z13 clusters after 40 ns creep testing. Moreover, in a common neighbor analysis, we could observe a minor increase of 0.4 % in the fraction of bcc atoms in the overall composite. These last two observations indicate a marginal stress-assisted relaxation of the interface. Nonetheless, the effect is negligible.

When comparing the composites in Figs. 45(b)-(e), it can be seen that the higher ϕ, the higher is the amount of glass atoms with a high atomic strain. This matches the observation of increasing creep rates with increasing ϕ. The more STZ sites can be activated, the higher is the resulting creep rate. Nanoscale microstructures in Cu-Zr-based MGs have been reported in literature,[8,82,184] with secondary phase particle diameters between 2 nm and 20 nm. This corresponds to our spherical inclusions, which have a diameter of 9 nm. In few studies with spherical precipitates, both the phase fraction and average diameter of the secondary phase are given,[9,184] which allows direct comparison of the specific interface area ϕ with our models. In Ref. 184, which is closest to our geometry, the average diameter of these particles is around 20 nm with volume fractions between $f = 0.064$ to 0.0176. This yields values of ϕ_{exp} between 21/µm to 53/µm. Since we use slightly higher volume fractions, we simulate higher specific interface areas, but they only differ by a factor of 4 to 10 from the experimental ones. Hence, we expect that the effect of increasing creep rate with increasing interface is experimentally observable.

7.3.2 *Influence of interface geometry*

We showed above that the interface promotes creep and that the specific interface area ϕ is directly related to the creep rate. If we assume a simple, three-phase composite model of glass, crystal, and interface, this would suggest that ϕ is the only parameter for creep. We tested this by generating simpler geometric shapes with similar parameters ϕ and f to the network structures, where f is always 0.3. Considering that the network composites have a complex interphase topology with a variety of surface orientations, we at first construct two simpler geometries: A non-percolating crystalline phase in the form of spherical particles and a percolating phase made of nanowires aligned with the loading direction, (see Figs. 41(c)

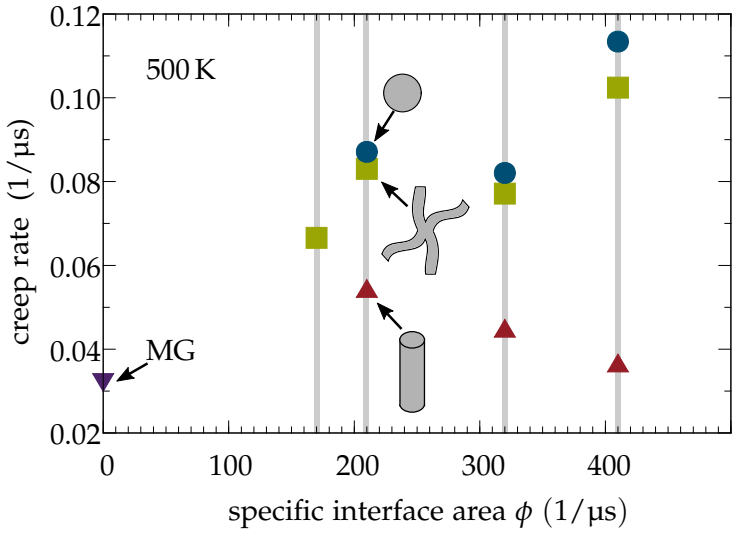

FIGURE 46: Correlation of creep strain rates fitted between $t = 25\,\text{ns}$ and $t = 40\,\text{ns}$ and specific interface area of various composite microstructures.

and 41(f)). These samples are then subjected to the same load of 750 MPa at 500 K for 40 ns. Their creep rates are shown in Fig. 46. If ϕ were the only parameter influencing the creep rates of our composites, the latter should remain unchanged when the shape of the crystalline phase is varied for constant f and ϕ. However, from Fig. 46 we see that this is not the case. Although all composite structures exhibit higher creep rates than the pristine glass, different secondary phase shapes lead to different creep rates for the same f and ϕ. The following trend can be identified for the network and sphere-containing composites: The higher the specific interface area, the higher is the creep rate. However, the opposite trend is visible for the nanowire composites. Thus, a simple model which only takes into account the relative fraction of the different phases is insufficient. Even the percolation cannot explain the different rates, as the non-percolating case (spheres) and the percolating network structures behave similarly. The remaining difference between the three cases is therefore the interface orientation.

Thus, in the next step we studied the creep rate dependence on the interface geometry for constant $f = 0.3$ and $\phi = 210/\mu\text{m}$. We also compared composites with percolating and non-percolating secondary phases: In addition to the secondary phase network, nanowires aligned with the loading direction and spherical particles, see Figs. 41(b)-(d), we introduce non percolating nanorods as in Fig. 41(e) and percolating nanowires, that are tilted 45°, see Fig. 41(f), and 90° to the z-axis. In Fig. 47, all these composites with different specific interface area ϕ are ordered with respect to their creep rates. The reference creep rate of the glass structure is shown on the right. The green bars are creep rates fitted from composites where the CuZr B2 crystal orientation is [100]. The highest creep rate is shown by the composite containing nanowires oriented 45° with respect to the loading direction. This is followed by the sphere and network composite, that have a similar creep rate. After that, the creep rate decreases for the wire that lies perpendicular to the loading direction. Furthermore, the lowest composite creep-rate is shown by the wires oriented along the loading direction. Interestingly, they are not significantly

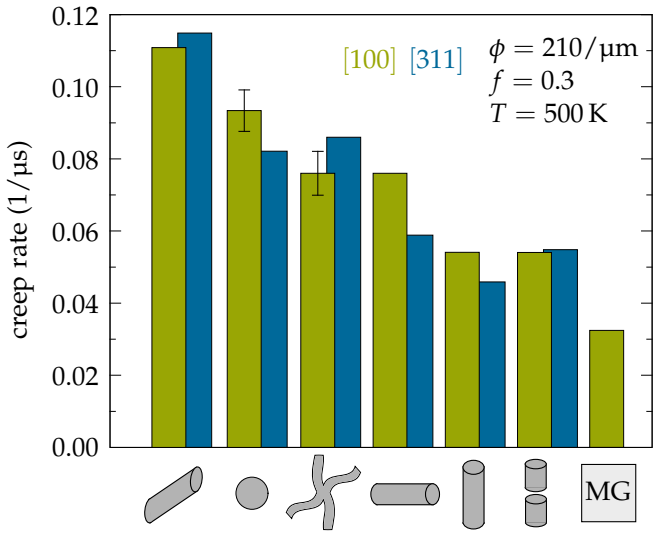

FIGURE 47: Creep rates of composites with $\phi_2 = 210/\mu m$ and volume fraction of 30%, but different shape of the secondary phase fitted between $t = 25\,ns$ and $t = 40\,ns$. The different colors reflect the orientation of the crystalline phase with respect to the loading direction: Green means [100], blue means [311].

changed when the wires are non-continuous. The error bars for spheres represent the standard deviation of four different spatial distributions of the spheres, while the error bars for the networks were determined by loading the structure in the three cartesian directions. We note that the size of the error bars is comparable to the difference in rates between the nanowires in Fig. 46. The reduction of rate with interface area does therefore not exceed the margin of error. The fluctuations in the creep rate can be explained by the fact that the glass is heterogeneous on length scales of nanometers[183] and is therefore sensitive to the location of the crystalline phase. Nevertheless, the hierarchy presented in Fig. 47 exceeds the margin of error.

As the interface controls the mechanical behavior, the results of our simulations may be influenced by the orientation of the crystals. Hence, we repeated the simulations with B2 crystalline phases oriented with the [311] direction along the z–axis. The results are also shown in Fig. 47 and do not significantly deviate from the results with a [100] orientation. Indeed, it was found earlier that the interface energy of copper crystals in $Cu_{64}Zr_{36}$ is only weakly dependent on the crystal orientation,[93] which is in line with the current results.

7.4 INTERFACE SCHMID FACTOR MODEL

The alignment of the glass–crystal interfaces is therefore the main factor controlling the creep rate, while percolation only seems to play a minor role. For the nanowires oriented in loading direction, the interface normal is always perpendicular to the loading direction, see Fig. 48(a). The 45° orientation however, seems to be favorable for creep deformation (Fig. 48(b)). Based on the idea of the Schmid factor m in a crystal, which translates the applied stress σ into a resolved shear stress τ on the

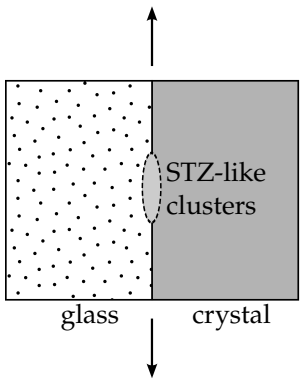

(a) inactive orientation

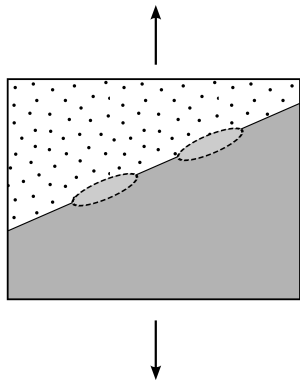

(b) activation of many STZs

FIGURE 48: The more interfaces with the highest Schmid factor are present in the composite, i.e., interfaces oriented 45° to the tensile load, the more STZs are activated in the glass.

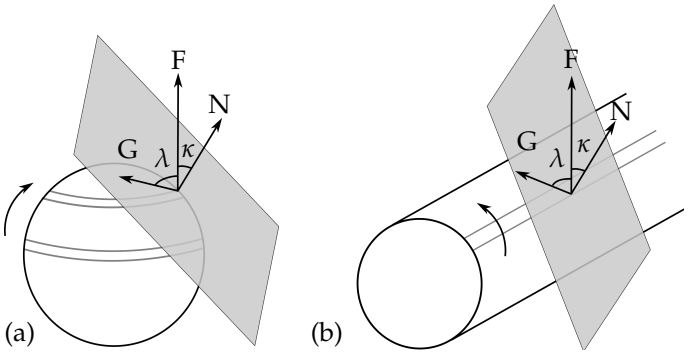

FIGURE 49: The integrated "interface" Schmid factor is expected to be different on a sphere surface (a) and cylinder (b). F is the direction of load, N is the normal of the tangential plane and G is the glide direction.

different slip planes and glide directions in a crystal, we define a Schmid-like factor for our composites. In a crystalline material, it is

$$\tau = m \cdot \sigma \tag{7.2}$$
$$= \cos\kappa \cdot \cos\lambda \cdot \sigma \, . \tag{7.3}$$

In our case, the amorphous interface regions act as preferential slip sites, so we use the concept of the Schmid-factor in a similar geometric derivation.

However, we assume that in the glassy interphase there are no restrictions to the glide direction $\boldsymbol{G}$ on the slip plane. The glide direction is thus the direction that maximizes $\cos\lambda$, which corresponds to the projection of the externally applied force $\boldsymbol{F}$ on the slip plane (represented by its normal vector $\boldsymbol{N}$). Using the definition of $\cos\kappa$ from the classical Schmid law, we arrive at

$$m(\boldsymbol{N},\boldsymbol{F}) = \cos\kappa \cdot \cos\lambda \tag{7.4}$$
$$= \frac{\boldsymbol{N}\cdot\boldsymbol{F}}{|\boldsymbol{N}||\boldsymbol{F}|} \cdot \underbrace{\frac{\boldsymbol{G}\cdot\boldsymbol{F}}{|\boldsymbol{G}||\boldsymbol{F}|}}_{\max} , \tag{7.5}$$
$$\text{with } \boldsymbol{G} = \boldsymbol{F} - \frac{\boldsymbol{F}\cdot\boldsymbol{N}}{|\boldsymbol{N}|^2}\boldsymbol{N} \, . \tag{7.6}$$

In Fig. 49 two example interface geometries are sketched.

We expect that different secondary phase topologies have different distributions of these local Schmid factors. In order to characterize these topologies, we use a total mean Schmid factor

$$M = \frac{1}{A} \int_A m(\boldsymbol{N}_{A'}, \boldsymbol{F}) \, \mathrm{d}A' \, . \tag{7.7}$$

(Note that m depends on the normal vector of the specific differential area for which it is calculated and cannot be moved out of the integral.) We choose six different composite structures with $\phi = 210/\mu\mathrm{m}$ and $f = 0.3$ for comparison. The integration over the interfaces is performed numerically: The software OVITO is used to create a surface mesh of the interface region by Delaunay triangulation.[163] For each of these triangles, we can calculate the surface area A and the surface normal $\boldsymbol{N}$ and thus m. Figure 50 shows the resulting total interface Schmid factors on the abscissa, while the ordinate shows the corresponding creep rates for the samples with $\phi = 210/\mu\mathrm{m}$. The data points show that—at constant temperature—the composite structures with higher total interface Schmid factors M exhibit higher creep rates. Note that since the mean interface Schmid factor has been determined numerically, even for the nano-rods and nanowire-type inclusions, M is not equal to zero. This can be attributed to the fact that there are surface triangles with surface normals non-perpendicular to the loading direction at the edges. The lines in Fig. 50 result from a fit of the Argon model [Eq. (2.5)] using $\tau = M\sigma$. This is obviously only a very rough trend, since the resolved stress varies for each surface triangle, each of which therefore contributes differently to the total creep. As such, we employed a model using local resolved stresses to obtain quantitative results:

$$\begin{aligned} \dot{\epsilon}(T, m_1, m_2, \ldots) = \underbrace{\alpha \nu_0 \gamma_0}_{\text{const.}} \cdot \exp\left(-\frac{Q}{kT}\right) \cdot \\ \cdot \left\langle \sinh\left(\underbrace{\gamma_0 \Omega}_{\text{const.}} \cdot \frac{m_i \sigma}{kT}\right) \right\rangle_i + \dot{\epsilon}_0(T) \, . \end{aligned} \tag{7.8}$$

In this formulation, the shear stress τ is replaced by the local resolved shear stress $m_i\sigma$, calculated for each surface triangle i. This modified sinh term is then averaged. This part of the equation represents the behavior of the interface phase. The term $\dot{\epsilon}_0(T)$ includes the contributions of the glass phase, while the crystalline phase only responds elastically and is therefore not included in the formula. Fitting parameters are the prefactor $\alpha\nu_0\gamma_0$, the activation barrier Q, the STZ activation volume $\gamma_0\Omega$, and $\dot{\epsilon}_0(T)$. The results of the fit, including simulations at two different temperatures, are plotted using crosses in Fig. 50 and agree well with the data. Table 1 lists the results of the temperature independent fit parameters.

As we can see, the activation barrier in the interphase is severely reduced compared to the values obtained for the homogeneous glass in Ch. 4 and those found in literature.[2,165] However, we observe that the noise in the creep curves is quite large compared to the creep rates that we try to fit. A detailed treatment of this

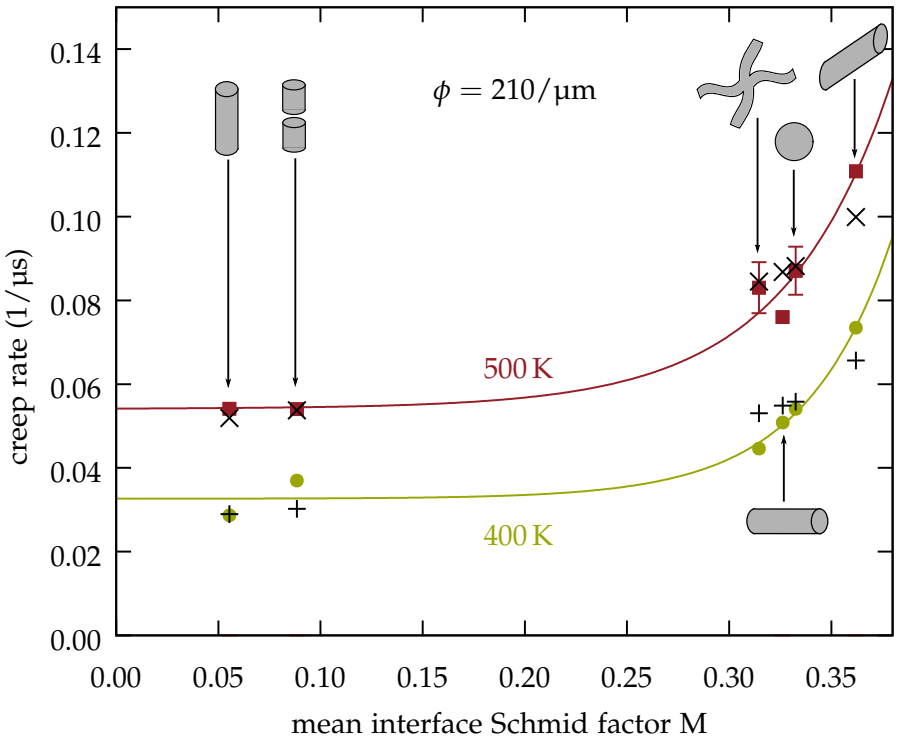

FIGURE 50: The data points show the creep rates vs. mean interface Schmid factor of composites with different shapes of the secondary phase but constant ϕ and $f = 0.3$. As a guide to the eye, the lines show an Argon-like creep behavior where the resolved shear stress is substituted by $M \cdot \sigma$. In addition, there is an offset caused by the fact that the glass matrix contributes to the creep strain. To properly fit the activation energy for creep, however, the local Schmid factors m_i have to be used, as they are included in the sinh function, see Eq. (7.8). The results are plotted as black crosses.

problem can be found in Sec. 7.6. The bottom line is that we cannot draw a quantitative conclusion concerning the activation energy and the prefactors. Nonetheless, this model shows that the interphase can be described as a weaker glass, where STZs are more easily activated. As such, it is more susceptible to a creep-like deformation behavior, even at lower temperatures. The orientation dependence hints towards anisotropic creep behavior of composites.

7.5 ELASTIC AND PLASTIC CREEP DEFORMATION

So far, we only quantified the composites' creep behavior in terms of creep rates. In addition to the creep rates fitted from steady state behavior, it is important to understand what happens at the onset of creep. Usually, the individual elastic and plastic contributions of the creep deformation overlap and are difficult to distinguish in the creep curve. The remaining plastic deformation can, however, easily be identified from the deformation that remains after unloading. Therefore, we

TABLE 1: Temperature independent fit parameters in Eq. (7.8).

parameter	$\alpha\nu_0\gamma_0$ (GHz)	Q (eV)	$\gamma_0\Omega$ (nm^3)
fit	0.394	0.346	0.172

revisit the creep simulations of the nanowire composites with ϕ_2, ϕ_3 and ϕ_4. After 40 ns, the wire composites are unloaded and relaxed for 20 ns. The corresponding data are depicted in Fig. 51.

The difference in strain between points A and C marked in Fig. 51 shows the composites' reversible part of the creep deformation. While AB is the elastic strain instantly recovered when the load is removed, BC shows an anelastic part that can be recovered over time. What is striking is that for all composites a significant part of the deformation is reversible; the homogeneous glass exhibits a lower anelastic strain. For the crystal, we would expect that once the load is removed it contracts to its initial length. In the composite, however, this is hindered by the glass-phase. We conclude that this remaining back stress together with a possible higher anelasticity of the interface leads to a significant time-dependent strain recovery. We note that the anelastic recovery is not completed after 20 ns, but that the anelastic recovery after 20 ns is very similar for all composites, see Fig. 52. The same is true for the elastic part, which is also comparable to the homogeneous glass. The plastic deformation that remains after removing the load and subsequent relaxation for

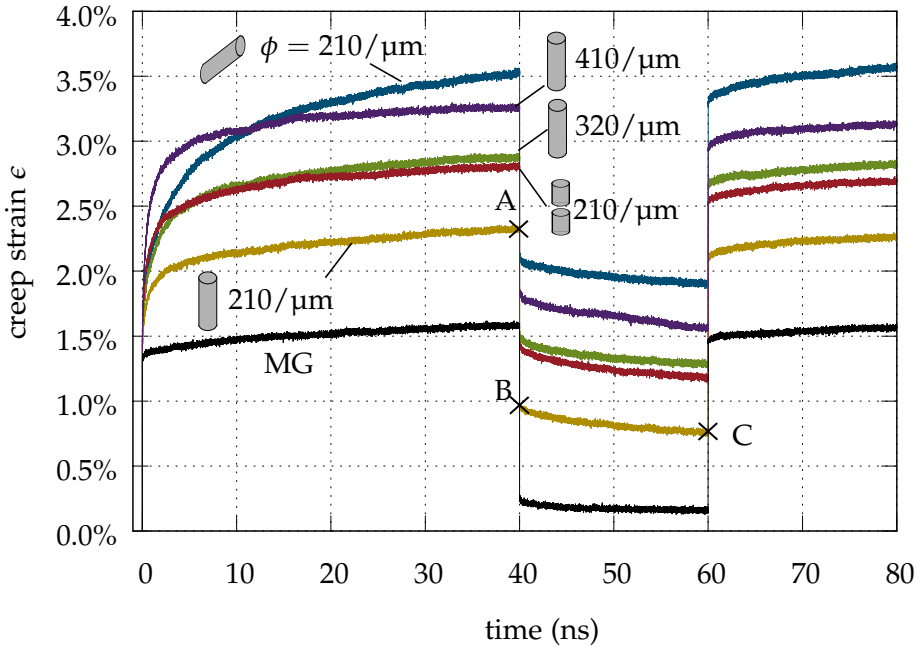

FIGURE 51: Loading–unloading cycle for nanowire composites. The distance AB marks the elastic part of the creep deformation. BC is a recoverable anelastic part and C the remaining plastic deformation.

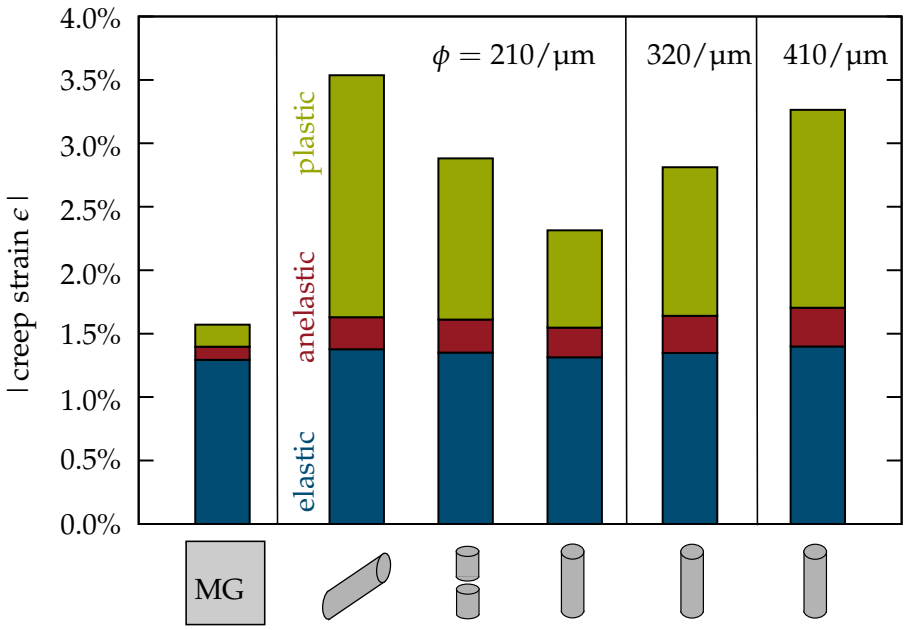

FIGURE 52: Different contributions to the strain calculated from the strain drop after unloading in Fig. 51.

20 ns, though, shows a significant dependence on the shape of the crystalline phase. This is in agreement with the results of the previous sections, which are now shown to be clearly plastic in nature, as the anelastic and elastic contributions do not differ significantly between the samples. This is to be expected, since the STZs (which are sensitive to the factor M) are plastic events.

7.6 QUANTITATIVE RELIABILITY OF FITS TO SIMULATION DATA

The activation barrier Q can only be determined by including data obtained using different temperatures and crystalline phase geometries, characterized by M. If we remove the temperature dependent offset term $\dot{\epsilon}_0(T)$ in the composites' creep rates, we note that the data points at the two temperatures are very close together, see Fig. 53. The scatter is on the order of the difference between the two data sets. Thus, the activation energy and the prefactors of the interface phase can only be determined approximately and cannot be interpreted as quantitatively reliable.

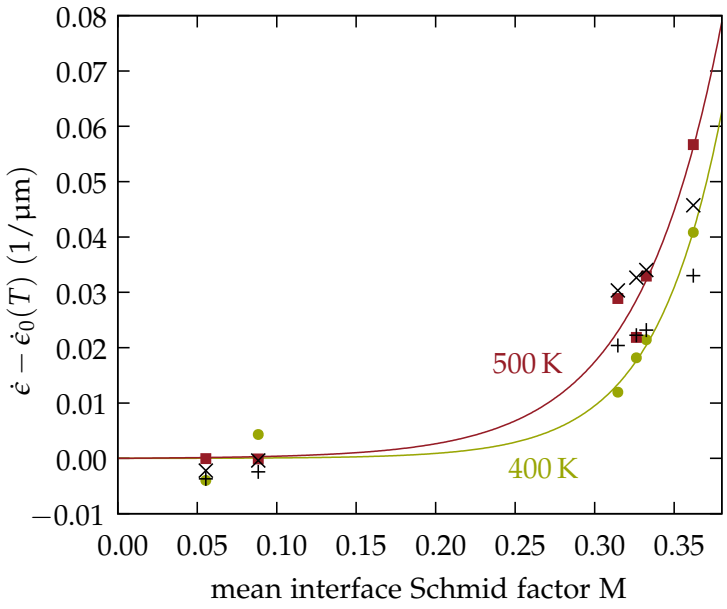

FIGURE 53: Colored data shows the creep rates and mean interface Schmid factors treated in section 7.4, but without the offset term. Thus, they reflect solely the properties of the interface. Black crosses represent the fit to the creep rates using Eq. (7.8).

7.7 CONCLUSION

In our simulations of the creep behavior of $Cu_{64}Zr_{36}$-glass and B2-crystal composites, we could observe a mixed regime of elastic, anelastic and plastic deformation. When comparing the creep behavior of the homogeneous glass to glass–crystal composites, where the crystalline phase only responds elastically, it could be shown that the composites have much higher creep rates than the homogeneous glass. Clearly, creep is promoted by the presence of interfaces. In our model system the interface presents a weak spot in comparison to the surrounding MG. Furthermore, by keeping the volume fraction constant but varying the shape of the secondary phase, we could analyze the influence of the specific interface area and the percolation of the secondary phase. We found that the creep rates of the composites strongly depend on the orientation of the glass–crystal interface. We have given an explanation in terms of the resolved shear stress τ derived from the concept of the Schmid factor in crystalline materials. This dependence of the creep rate on the anisotropy of the secondary phase should be taken into account when designing creep resistant MG composites.

8

INFLUENCE OF GLASS–CRYSTAL INTERFACE PROPERTIES

The results presented in this chapter have been obtained in collaboration with Dr. Tobias Brink, who provided the original composite model and implemented the calculation of the Kelvin shear moduli.

In Ch. 7 we have shown that weak glass–crystal interfaces in Cu-Zr-composites decrease their creep resistance and that the effect not only depends on the specific interface area but also on the interface orientation of the secondary phase.[177] All the benefits to the mechanical behavior in having secondary phase inclusions were outweighed by the presence of the interfaces, because the activation of STZs was easier therein. In short, as long as there are energetically unfavorable "artificial" interfaces present in our models, no improvement in creep resistance is to be expected from the introduction of secondary phases.

In contrast to this artificial "cut and paste" procedure, simulations of "in-situ" composites using the EAM potential by Mendelev *et al*. have been realized.[25,153,154] During long-time annealing simulations of $Cu_{64}Zr_{36}$ at temperatures in the vicinity of T_g, precipitation of the strong C14 and C15 Cu_2Zr Laves phases can be observed. As explained in Sec. 3.3.2.2, the short range order of the Cu atoms in the Laves phase is very similar to the the most favorable motif in the amorphous phase, i.e. full icosahedral order. This results in very stable glass–crystal interfaces between the Laves phase and the MG matrix. In this chapter, we exploit the fact that although Laves phases are not expected to appear in the experimental equilibrium CuZr phase diagram,[157] the Mendelev potential stabilizes them even below T_g.[25,153,154,157] Rather than focussing on the specific properties of of Cu_2Zr-Laves phases in the Cu-Zr system, which already have been treated in detail in Refs. 25 and 168 , we want to use these glass-crystal composites as generic composite models exhibiting very stable interfaces. In addition, this new type of composite model allows us to address the question if the creep behavior of a MG-crystal composite can be altered by tuning the properties of the interface phase. After studying the creep behavior of the as-grown composites, we will disturb the CSRO in these interfaces and probe these samples under identical creep conditions.

8.1 SIMULATION SETUP

The undisturbed reference composites models have been prepared by Tobias Brink following this thermal protocol:[25,168] First a $Cu_{64}Zr_{36}$ MG sample of 63108 atoms

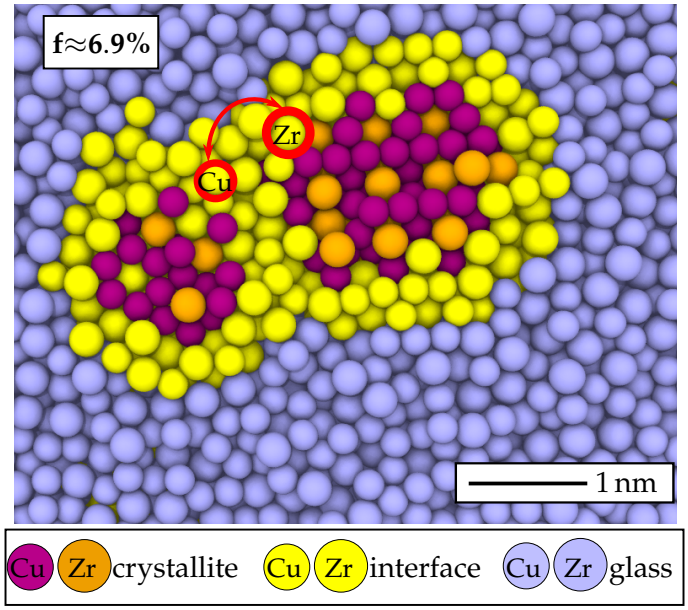

FIGURE 54: Simulation setup: Interchange of atoms in the glass-crystal interphase. Slice through two neighboring Cu_2Zr Laves phase crystallites embedded in a Cu-Zr glass matrix. The atoms in the glass-crystal interface region have been marked in yellow. In order to disturb the interface structure, the chemical identity of random Cu and Zr atoms within that region are interchanged.

is quenched from the melt at $\dot{T} = 0.01\,\mathrm{K/ps}$ and relaxed for 2 ns. To induce crystallization of Laves-type crystallites, the glass is then heated to 800 K with $\dot{T} = 0.1\,\mathrm{K/ps}$ and annealed at that temperature. After different annealing times, $t = 0.3\,\mu\mathrm{s}$, $t = 1.9\,\mu\mathrm{s}$ and $t = 3.8\,\mu\mathrm{s}$ the annealing is interrupted and three samples are quenched to $T = 50\,\mathrm{K}$ at $\dot{T} = 0.01\,\mathrm{K/ps}$. In that way, composites with different volume fractions f and crystallite sizes have been generated: $f_A = 6.9\%$, $f_B = 29.0\%$ and $f_C = 59.1\%$, where f is the fraction of atoms in the Laves phase. The method to identify Laves phases within the glass matrix is described in section 3.4.2. For our interface studies, we replicate these samples by $2 \times 2 \times 2$ to obtain larger composites of 504864 atoms and dimensions of $20 \times 20 \times 20\,\mathrm{nm}^3$.

We first compare the creep behavior of these three samples at $T = 500\,\mathrm{K}$. In a next step, we want to study how the creep response of a glass-crystal composite can be tuned by the state of the interface region. Therefore we use the annealed glass structure with crystalline phase fraction of $f_A = 6.9\%$ as a reference. The interface region in this reference structure is then manipulated to different extents, such that the positions of Cu and Zr atoms within that region are randomly swapped. In doing so, we assure that the concentration in the interface as well as the glass matrix structure, specific interface area and volume fraction of secondary phase remain constant. Here, the interface region is defined as the region consisting of glass atoms that are neighbors to Laves atoms within a cutoff radius of 5 Å. Figure 54 depicts a slice through two neighboring Laves crystallites embedded in the glass matrix. An example of an atom swap is shown, i.e. the positions of a randomly chosen Cu and Zr atom in the yellow interface region are interchanged. In that way five different interface structures are modelled, where 5%, 10%, 15%, 25% and 50% of Cu atoms in the interface have been swapped with Zr atoms, in the following referred to as sample I-V.

8.2 PRECIPITATION HARDENING

The creep curves of an as-cast homogeneous $Cu_{64}Zr_{36}$ metallic glass and the same sample after different annealing times are depicted in Figure 55. The annealed glasses contain different volume fractions of crystalline Laves phases, i.e. both C15 and C14 Cu_2Zr, that have precipitated and grown in the glass matrix. The as-cast glass exhibits an instant elastic strain of 1.3% and a total creep strain of 1.6% after 40 ns. In comparison, the annealed glasses, that contain different volume fractions of secondary phase, are more creep resistant. It can be observed, that the higher the crystalline volume fraction, the lower is the instant elastic response to the creep load and the creep rate. There are two factors contributing to this behavior [cf. Refs. 25 and 168]: On the one hand, the Laves crystallites decrease the composites resilience and increase their yield stress. On the other hand, also the glass matrix has changed structurally during the preceding annealing process, which was accompanied by and increase of the fraction of icosahedral units (that are not part of the Laves phase). In consequence, the glass matrices are in different relaxation states and the increase in creep resistance of the composites is to be expected.

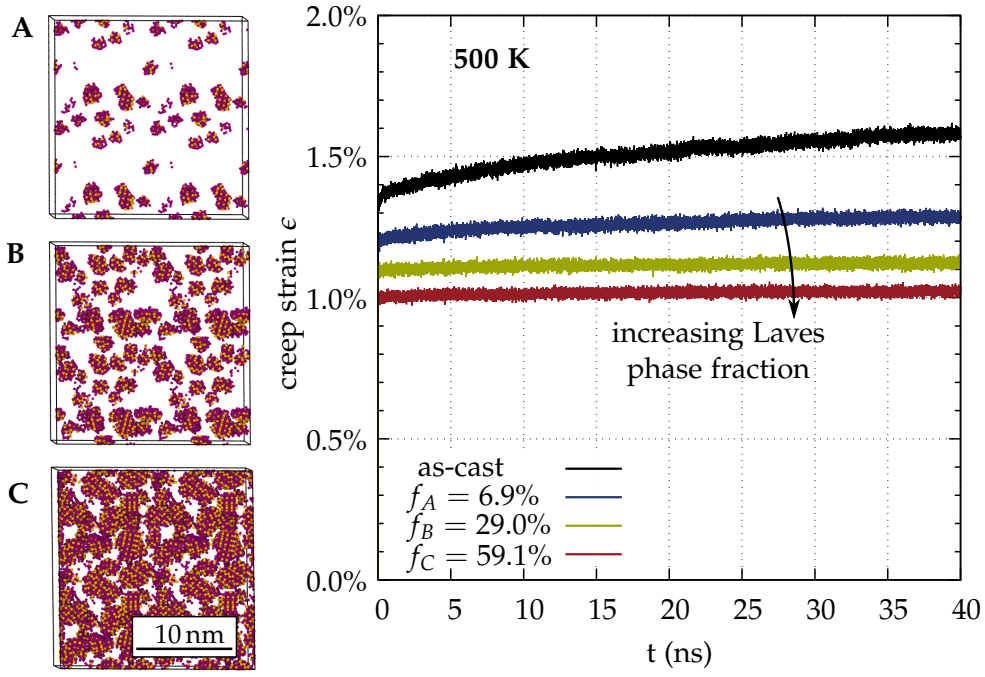

FIGURE 55: Right: Creep curves of a homogeneous metallic glass in the as-quenched state and after different annealing times at $T \approx T_g$. The samples contain different volume fractions of secondary phase, i.e. $f_A = 6.9\%$, $f_B = 29.1\%$ and $f_C = 59.1\%$, depending on their annealing time. The samples that have been annealed the longest show the lowest creep rates. Left: Snapshots of a slice through samples A, B and C, showing only atoms belonging to the Laves phase (Cu: magenta, Zr: orange).

Another means of characterization of these composites is to compare their specific glass-crystal interface areas. With increasing volume fraction and crystallite size, the specific interface area increases from $\phi_A = 301\,\mu m^{-1}$, $\phi_B = 856\,\mu m^{-1}$ to $\phi_C = 900\,\mu m^{-1}$. The reason for these quite large values as compared to the composites used in Ch. 7 are the small crystallite sizes $d_A = 1.5\,nm$, $d_B = 1.8\,nm$ and $d_C = 3.1\,nm$ (values taken from Ref. 25). Here, the only drawback of simulating the precipitation of the Laves phase is that we cannot control the shape and volume fraction of the secondary phase at the same time. For comparability, we choose sample A for the interface manipulation study, since its specific interface area is closest to the samples in Ch. 7.

8.3 DISTURBING THE CHEMICAL SHORT RANGE ORDER

After manipulating the CSRO within the glass-crystal interfaces of sample A we firstly probe the low-temperature mechanical properties of samples A and I–V. Strain-rate controlled tensile tests ($\dot{\epsilon} = 4 \times 10^7\,s^{-1}$) of these samples have been performed at $T = 50\,K$ and $T = 300\,K$. The results are depicted in Figures 56(a) and (b). Disturbing the CSRO by switching 50% of Cu and Zr atoms in the interfaces causes the 50 K yield stress to decrease by 1.7 GPa. At 300 K the yield stress is reduced from 3.2 GPa down to 1.7 GPa. For the severly manipulated interfaces, the typical stress overshoot disappears completely and the stress-strain curve resembles those exhibited by tensile tests of NGs.[94]

Furthermore, the creep behavior of the untreated sample A and the samples with lightly to severly manipulated interfaces are shown in Figure 57(a). As can be seen from the total creep strain after 40 ns, manipulating the interfaces severly reduces the creep resistance. Sample A-5, where 50% of all Cu atoms have been interchanged with Zr atoms, reaches a total strain of 4.5%. That is a difference of

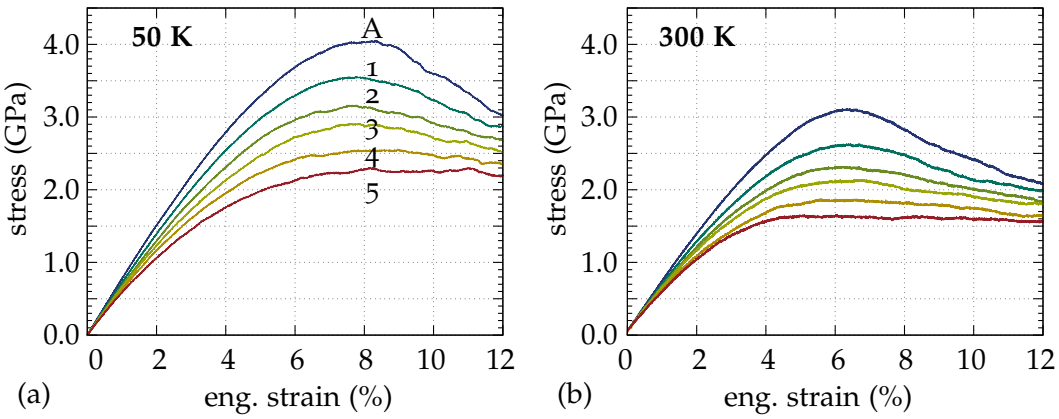

FIGURE 56: (a) Strain-rate controlled tensile tests at $T = 50\,K$ and $T = 300\,K$ of the composite reference sample A with Laves phase fraction $f = 6.9\%$ and its five derivates, where the interfaces have been manipulated to different extents: 5% (1), 10% (2), 15% (3), 25% (4) and 50% (5) of the Cu atoms in the interface have been interchanged with Zr atoms.

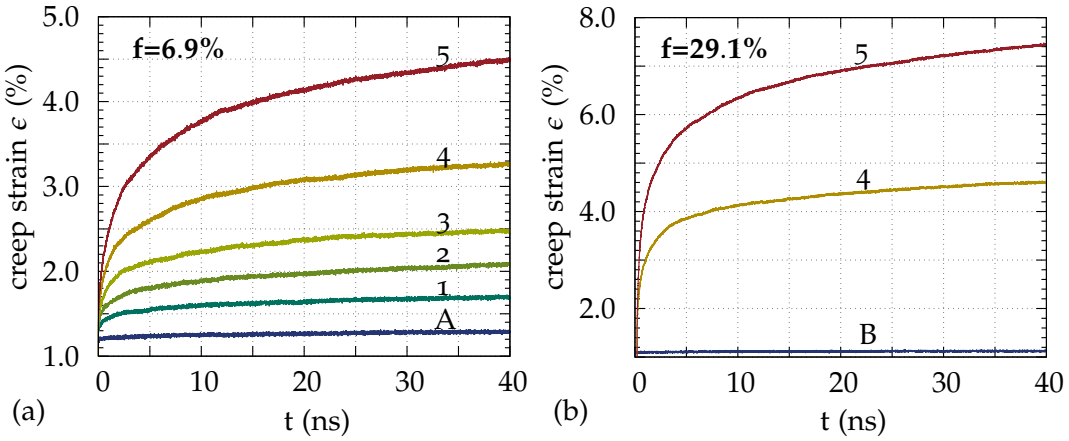

FIGURE 57: 500 K-creep curves of the annealed MG composites with (a) $f_A = 6.9\%$ Laves phase fraction and five different variations of that sample where the positions of 5% (1), 10% (2), 15% (3), 25% (4) and 50% (5) of Cu atoms in the interface have been interchanged with Zr atoms. (b) 500 K-creep curve of reference sample B with $f_B = 29.1\%$ and two samples, where 25% (4) and 50% (5) of interface atoms have been interchanged. Samples with highly disturbed interfaces exhibit higher creep rates.

more than 3% creep strain as compared to the original annealed sample, shown in dark blue. The same study has been repeated for sample B with $f_B = 29.1\%$ secondary phase, see Figure 57(b). Here, the effect of manipulating the interfaces is even more pronounced: Sample B-5 reaches a total creep strain of 7.4% after $t = 40$ ns.

In order to understand the influence of the interface structure on the creep behavior of a composites, the annealed and manipulated samples are characterized by means of their atomic Voronoi indices. Again, the interface region is defined as the region filled with atoms that are neighbors of Laves type atoms within a cutoff of 5 Å. In doing so, the composites can be segmented in three different phases, glass matrix, crystallites and interface. Figure 58 compares the Voronoi statistics of the glass phase and interface phase of the as-cast sample to samples IV and V. We distinguish between Cu and Zr-centered polyhedra, and show only the Voronoi polyhedra that occur more often than 2% in either phase in Figures 58(a) and (b). Furthermore, the polyhedra are ordered with respect to the coordination number of the center atom. The nomenclature commonly used in literature distinguishes between the geometrically favored clusters of a certain coordination, the so-called Z-clusters, and their geometrical derivates, the CN-clusters[12] and we will adopt that nomenclature in the following. In the reference sample, the population of polyhedra larger than the threshold value is actually very similar within the interface and glass phases: In the Cu-centered statistic, the decrease in Z-clusters in the interface can be explained by the occurence of CN-clusters of the same coordination. This again speaks for the fact that the interface structure is well relaxed.

Moreover, in all samples, the Cu-centered Z12-cluster remains the most prominent structural motif in the glass-matrix, followed by its slightly distorted version,

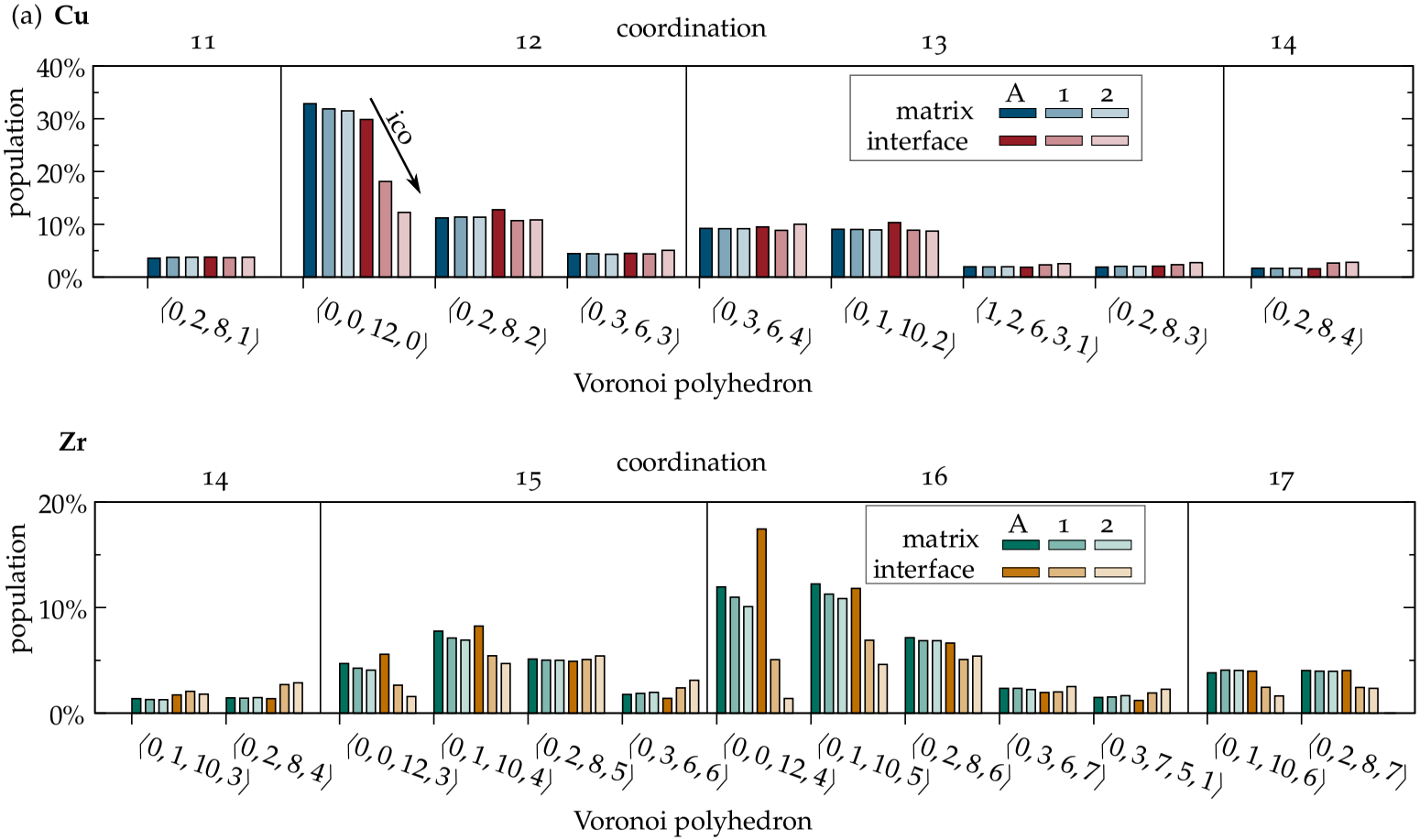

FIGURE 58: Statistics of the (a) Cu-centered and (b) Zr-centered Voronoi polyhedra that occur more often than 2% either in the glass or the interface phase. The plots compare the reference sample A to samples A-4 and A-5, where 25% and 50% of the Cu atoms in the glass-crystal interface have been interchanged with Zr atoms. (a) The fraction of Z12 clusters is mainly reduced in the interfaces but also in the glass matrix. (b) Coordination numbers of the Zr atoms are generally higher. The $\langle 0,0,12,4\rangle$ peak is an indicator for Laves-like ordering.

the $\langle 0, 2, 8, 2 \rangle$ polyhedron. The interface manipulation mostly affects the population of Z12-clusters in the interface; it is lower in samples where more interface atoms have been interchanged. More geometrically unfavored motifs with coordination numbers CN > 12 appear in the interface. A similar trend can be observed for the Zr-centered polyhedra: The population of geometrically unfavored CN-motifs is increasing at the cost of the population of Z-clusters. In the pristine sample, the Zr-centered Z16 polyhedron with index $\langle 0, 0, 12, 4 \rangle$ is the most prominent motif in the interface. That means that most of the Zr atoms in the interface actually have the same coordination as in the Laves phase.

The Z16 polyhedra are also the Zr-motif that is the most destroyed during the interface manipulation. In addition, the Voronoi statistics of sample A show that when manipulating the glass-crystal interfaces, there is only small interference with the glass matrix. However, we could observe that at higher phase fractions, e.g. $f_B = 29\%$, the impact on the glass matrix can not be neglected, since crystallite sizes are bigger and the dimensions of the glassy regions between the crystallites become smaller and more sensitive to changes in the neighborhood. This is shown in Figure 59. Here, the topological short range order in the glass matrix is strongly affected by disturbing the CSRO in the interfaces. Thus, the original idea, to isolately study the influence of the interface properties is at least not realizable in samples B and C.

This leads us to the next question of how we can quantify the impairing of the composites mechanical properties caused by destabilizing the interfaces. Here, the shear modulus G is a good measure to characterize the stiffness of the different phases. More specifically, in MD simulations of MGs the per-atom Kelvin shear moduli G_1 have been used to characterize the glass in terms of soft spots.[25, 185] The distribution of the per-atom shear moduli G_1 in the different composite phases are given in Fig 60. Again, we distinguish between atoms in the glass matrix, interface and crystalline phases. The blue curves correspond to the untreated sample A. From the positions of the maxima of the distributions it is evident that the crystal-

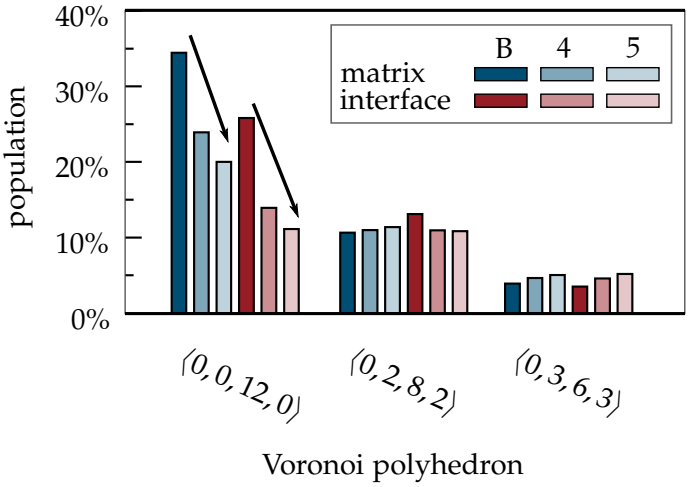

FIGURE 59: Population of the three most common 12-fold coordinated voronoi polyhedra in reference sample B, $f_B = 29.1\%$, and two variation of that sample, where the positions of 25% and 50% of all Cu atoms in the glass–crystal interface have been interchanged with Zr atoms. Both the matrix and interface regions are affected by the interface manipulation.

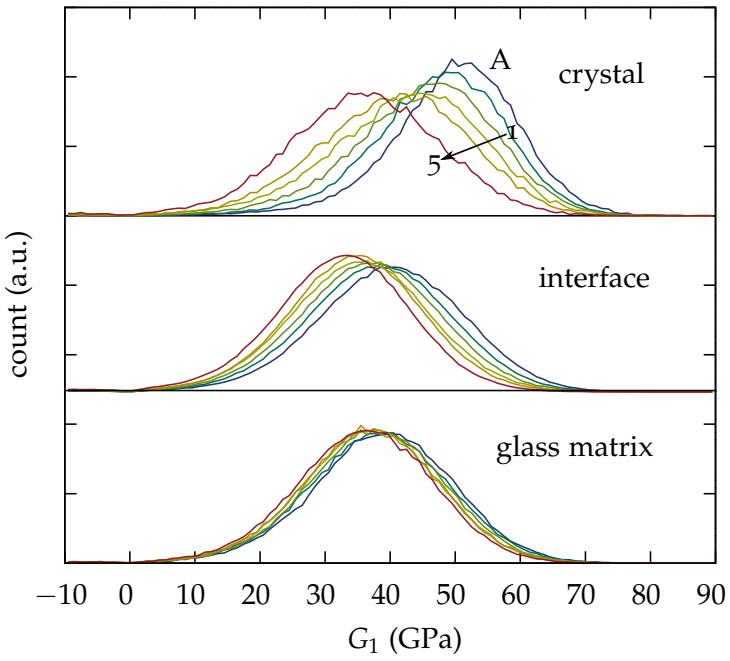

FIGURE 60: Distribution of the lowest per-atom Kelvin shear moduli G_1 in the glass matrix, interface and crystal phases. The crystallites are so small, that they are also softened when the interface regions are manipulated.

lites are stiffer than the glass matrix and that the interfaces exhibit values in between those of the matrix and the crystallites. This corroborates the reinforcing effect observed in Figure 55. Then, after disturbing the interfaces, the situation changes: While the values in the glass matrix do not change significantly, the distribution of atomic shear moduli in the interface clearly shifts and indicates a softening of the interface. In samples A4 and A5 the relation of G_1 in the interface and glass matrix has been reversed. What is striking is that even the crystallites are affected by the interface manipulation. Since they have a mean diameter of only 1.5 nm, and the cutoff of the potential is about half of that value, the perturbation of the immediate neighborhood can in the worst case affect atoms down to the core of such a crystallite.

8.4 EXCESS ENERGY AND CREEP RATE

In the previous section we could correlate the enhanced creep rates of the composites with the softening of the interfaces. In nanocrystalline materials the diffusion in the grain boundaries plays an important role in the creep deformation. A correlation between the interface energy γ and the self-diffusion coefficients in the grains D_{lattice} and grain boundaries D_{GB} has been found,[113,114]

$$D_{\text{GB}} = D_{\text{lattice}} \exp\left(\frac{\gamma}{\rho k_B T}\right), \tag{8.1}$$

which means that for vanishing interface energies, D_{GB} converges to D_{lattice}. Since the diffusion coefficient should be proportional to the creep rate, it is tempting to

relate the relative creep rates of the disturbed composites $\dot{\epsilon}_{\text{disturbed}}/\dot{\epsilon}_{\text{untreated}}$ to the interface energy, analogous to Eq. 8.1. This is valid under the assumption that only the interface phase and the glass matrix exhibit viscous flow around the stiff Laves-phase grains and that there is no dislocation activity in the crystallites. The findings of the previous section emphasize how sensitive the results are to the definition (e.g. the exact position) of the interface region. We thus expect a large error-bar on any quantitative analysis. To avoid this problem, we choose to calculate excess energies without having to make approximations on the position of the interface. Here, the excess energy is defined as the difference between the potential energy of the manipulated composites with respect to the undisturbed reference structure,

$$\Delta E = \frac{(E_{\text{pot}}^{\text{dist}} - E_{\text{pot}}^{\text{untr}})}{N}, \tag{8.2}$$

where N is the total number of atoms in the sample. The excess energy is thus normalized with respect to all atoms in the system, not just those in the interface region. The results of this analysis are presented in Figures 61(a) and (b). Indeed, the data follows an exponential scaling law similar to Borisov's model for grain boundary diffusion:

$$\dot{\epsilon}_{\text{dist}}/\dot{\epsilon}_{\text{ref}} = \exp\left(\frac{\Delta E}{\rho k_B T}\right) = \exp\left(\alpha \Delta\gamma\right) . \tag{8.3}$$

We already discussed the difficulty in having to define the position of the interface. Nevertheless, for comparison with experimental values we would like to give an estimate of an excess interface energy in units of $\mathrm{J/m^2}$ rather than in eV/atom. When constructing a surface mesh around the crystalline particles as described in Sec. 3.4.5 we obtain an interface area of $2450\,\mathrm{nm^2}$ in the annealed sample A. This value is then used to convert the excess energy per atom in an actual interface energy in units of $\mathrm{J/m^2}$, e.g.,

$$\frac{1\,\mathrm{meV/atom} \cdot 504864\,\mathrm{atoms}}{2450\,\mathrm{nm^2}} \cdot 1.602\,18 \times 10^{-19}\,\mathrm{J/eV} \approx 33\,\mathrm{mJ/m^2}. \tag{8.4}$$

The thus determined excess interface energy of sample A is plotted on the second abscissa in Figure 61(a), showing that at $T = 500\,\mathrm{K}$ an excess interface energy of $0.7\,\mathrm{J/m^2}$ leads to an increase in creep rate by a factor of 10.

In Figure 61(b), data from the creep experiments of sample set B (cf. Figure 57(b)) are included in the fit. Since samples A and B have different specific interface areas it is not possible to convert the second abscissa in energy units of $\mathrm{J/m^2}$ in the graphical representation chosen in Figure 61(b). Still, since they have the same number total number of atoms and roughly the same volume, the correlation between the relative creep rates and the excess potential energy introduced through interface manipulation is well described by exponential scaling as in Eq. 8.3. That means that in the case of MG-crystal composite types, that include stiff precipitates which do not participate in the viscous flow, Eq. 8.3 gives a good estimate

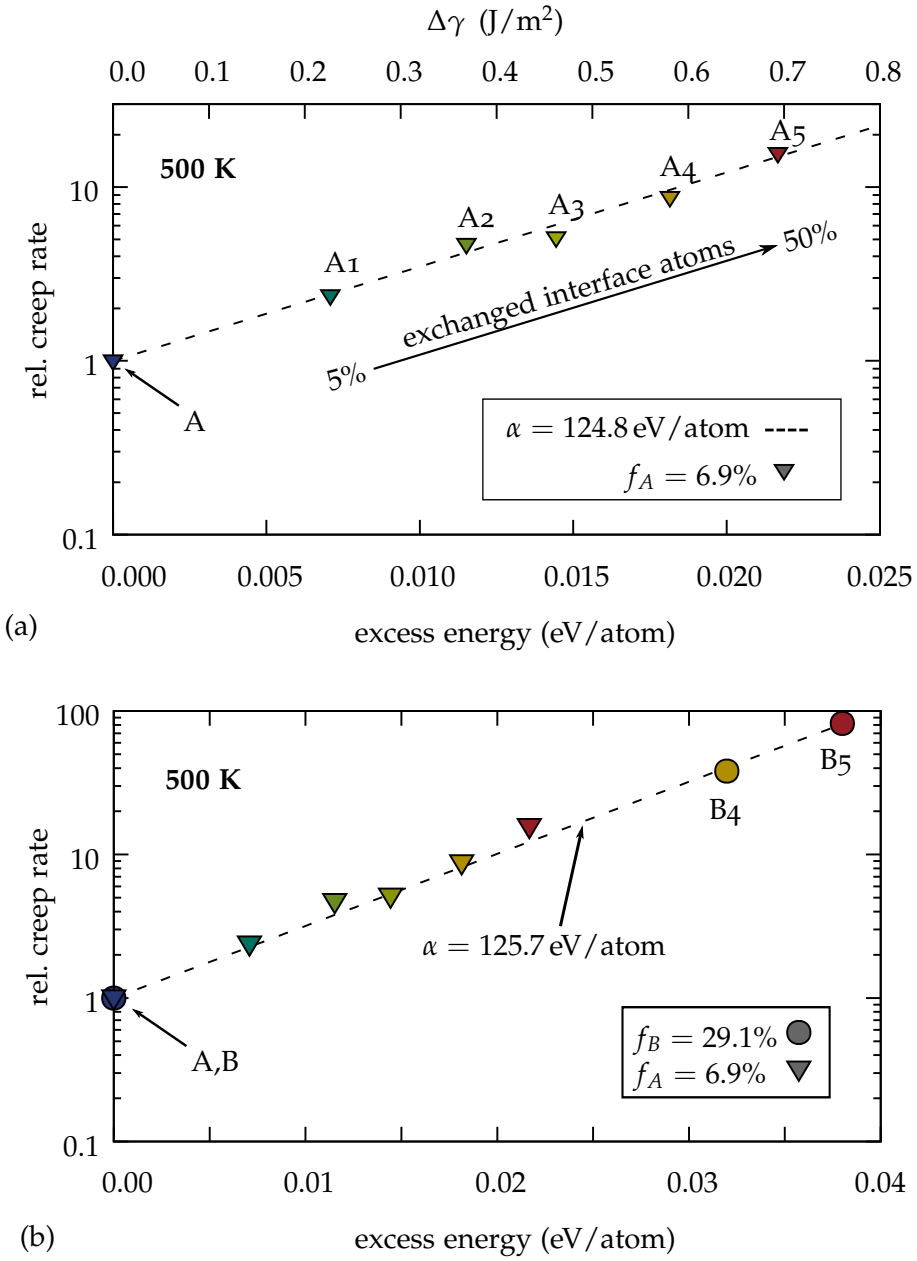

FIGURE 61: Excess energy per atom vs. relative creep rate. The dashed line is the fit function given in the legend. (a) Here the relative creep rate is the creep rate of sample A with respect to the creep rate of the as-cast sample. The excess energy is the excess potential energy per atom with respect to the as-cast sample. (b) Creep data from sample set B has been included in the fit.

of how any excess energy introduced in the interfaces decreases the creep compliance. Possible ways to introduce excess energy in the interfaces could be through solute segregration at the glass-crystal interfaces, or even irradiation damage. In MD simulations of nanocrystalline Cu-Nb alloys,[186] e.g., the grain boundary energy was found to decrease with increasing Nb-concentration in the grain boundaries. During subsequent creep simulations the samples with lower grain boundary energies exhibited higher creep compliances. Similarly, irradiation induced creep simulations of nanocrystalline copper revealed that the creep rates are controlled by the amorphous grain boundary phase, and that with decreasing grain sizes, the creep behavior of the nanocrystalline material approaches the one observed for bulk amorphous materials.[187] Here, we approached this question starting with the opposite scenario, i.e. composite types with large amorphous phase fractions. When increasing the crystallite size we approach the other limiting case, i.e., the composite type C with a large volume fraction of crystallites separated by glassy grain boundaries [cf. Figure 55]. This composite type could also be viewed as nanocrystalline, since the amorphous phase embedds the crystallites in grain-boundary like manner. Even for this limiting case, the creep properties are still dominated by the viscoelastic behavior of the amorphous phase.

8.5 CONCLUSION

More physical MG-composite models of $Cu_{64}Zr_{36}$ MG containing stiff Cu_2Zr Laves type crystallites obtained by simulating precipitation annealing[25] allowed us to study the influence of the glass–crystal interfaces on the creep resilience. By disturbing the CSRO of the glass–crystal interface phase in these composite models, we have shown that the composites' creep behavior critically depend on the relaxation state of the interface phase. The samples were characterized in terms of excess energy per atom as compared to the untreated sample. Furthermore, we found that for constant volume fraction of secondary phase and constant specific interphase area, the creep rate scales exponentially with the introduced excess energy per atom, analogous to Borisov's model for diffusion in grain boundaries.[113,114] According to our fit model, an excess energy of 5.6 meV/atom (which for the specific case of composite type A corresponds to $0.18\,J/m^2$) causes a doubling in the creep rates observed between 25 ns and 40 ns at 750 MPa and 500 K.

9

REINFORCEMENT OF NANOGLASSES

The results presented in section 9.2 have been published in Ref. 188.

In addition to MG-crystal composite technology there is an alternative to avoiding the formation of a critical shear band and hence critical failure: So-called NGs exhibit a heterogeneous structure with both glassy grains and grain boundaries and are produced through cold compaction of glassy precursor particles. The resulting microstructure is quite successful at dispersing shear bands. Usually though, the gain in ductility comes at the expense of the mechanical strength.

The key result from the previous chapters is that low-temperature mechanical properties as well as the creep behavior of MG-crystal composites strongly depend on the properties of the glass-crystal interfaces. In this chapter, we focus on the effect of internal interfaces in NGs. Hypothetically, if it were possible to freely manipulate the interface phase in the NG architecture without affecting the glassy grains, a sensible choice would be to turn that phase into a reinforcement. This can be seen in analogy to grain boundary strengthening in crystalline materials. Here, we study the mechanical properties of a generic model of a Cu–Zr cold–compacted NG and several reinforced NGs. To that end we manipulate the pristine NG by replacing the glass-glass interface with three different crystalline interphases with higher yield strength. The crystalline phases used as grain boundary reinforcement are expected to fail in a brittle manner in their bulk form. However, we will show that on the contrary, the presence of interface interphases does not necessarily impair the overall ductility while still being beneficial to the strength of the NG–composite. Finally, the results presented in chapters 7 and 8 are suggesting that the high fraction of interphase phase in both conventional and reinforced NGs will also play a major role in their creep behavior. This will be elucidated in the last section of this chapter.

9.1 SIMULATION SETUP

For this study, Dr. Omar Adjaoud provided the as-cast homogeneous MG sample and the conventional NG sample.

We study three different model types: (a) a homogeneous glass, (b) a conventional nanoglass and (c) nanoglasses reinforced with three different crystalline phases. The different processing routes of the models are shown schematically

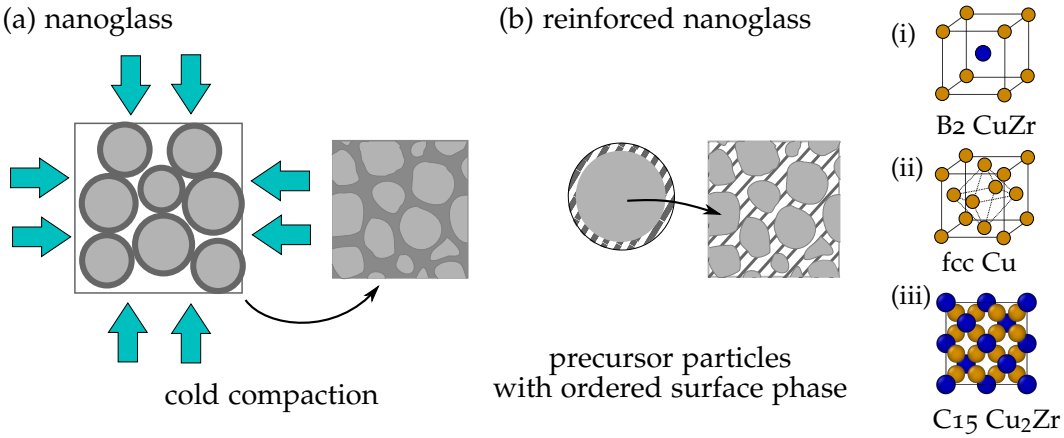

FIGURE 62: Overview of the different sample setups. (a) The homogeneous glass is quenched from the melt. (b) Then a conventional NG is produced by cold compaction of surface segregated glassy spheres cut from the bulk sample and subsequently annealed above T_g. (c) To reinforce the conventional NG, the glassy interface interphase is replaced by a crystalline phase. This can be single crystalline (i) B2 CuZr, (ii) fcc Cu or (iii) the C15 Laves phase.

in Fig. 62: In a first step, a homogeneous Cu–Zr MG is quenched from the melt at zero pressure with a quenching rate of 0.01 K/ps. The MG has the composition $Cu_{61}Zr_{39}$ and serves as a reference for all other models. For the conventional NG, glassy spheres are cut from a $Cu_{64}Zr_{36}$ homogeneous glass and subsequently annealed above T_g as described in Ref. 98. In this previous study, it has been shown that during annealing, the glassy spheres get enriched with Cu at the surface layer and depleted of Cu–atoms in the core. The NG model is then produced by simulating cold compaction of these glassy spheres at a compaction pressure of 5 GPa. The surface segregation process causes the surface layer and the core composition to deviate from the nominal composition of $Cu_{64}Zr_{36}$. The glassy spheres then form a $Cu_{72}Zr_{28}$ shell around a $Cu_{61}Zr_{39}$ core. As a result, the compacted NG has a glassy interface interphase that is richer in Cu as compared to the grain interiors. Finally, we manipulate the model of the NG by replacing the amorphous, Cu–rich grain boundary phase with different single crystalline phases, cf. Fig. 62(c). These phases are (i) B2 CuZr , (ii) fcc Cu, and (iii) the C15 Cu_2Zr Laves phase. After the insertion of the new grain boundary phase, the NG composites are equilibrated at 50 K for 1 ns. Tensile tests are simulated with a constant engineering strain rate of $4 \cdot 10^7\,s^{-1}$ in z-direction and pressure is controlled in x-and y-direction to enable lateral contraction.

9.2 CONVENTIONAL TENSILE TESTING

The mechanical response to straining of the homogeneous MG and the NG is shown in Fig. 63. The stress–strain curve of the homogeneous glass shows the typical stress–overshoot observed in MD–simulations of MGs.[24,94] When the yield strength

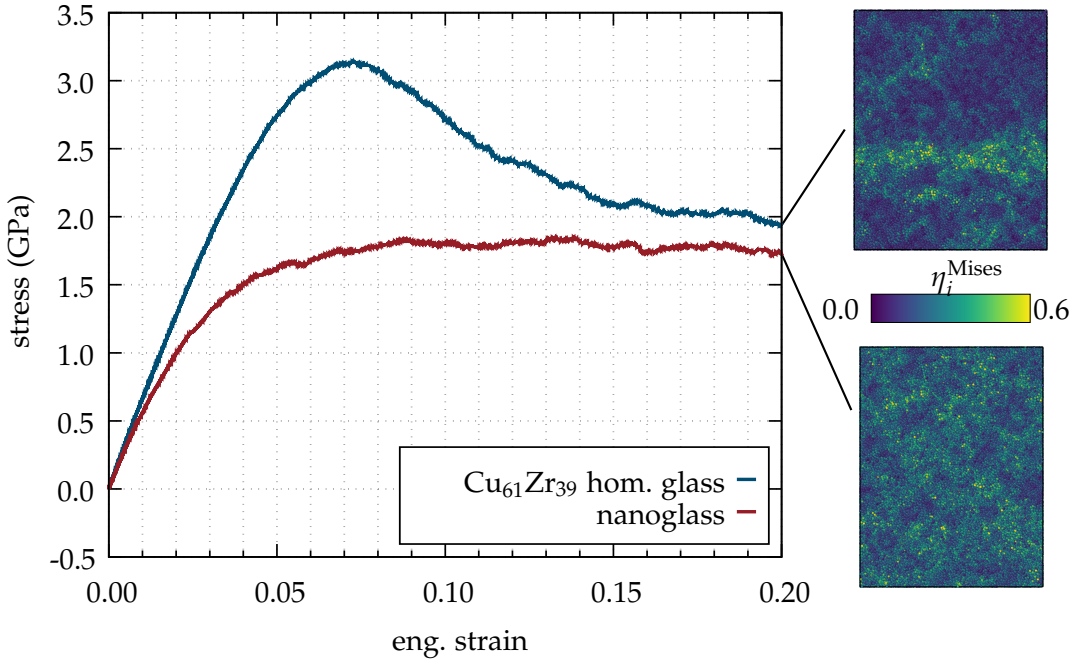

FIGURE 63: Tensile tests at 50 K and constant engineering strain rate of a homogeneous MG of composition $Cu_{61}Zr_{39}$ and a segregated NG, where the glassy grains have the same composition as the homogeneous glass. The snapshots of the MG and NG show the local atomic von Mises strain.

of 3.1 GPa is reached in the MG, shear bands nucleate, the material softens and the flow stress drops to 2 GPa. The NG on the other hand, does not exhibit such a stress-overshoot. Moreover, the steady state flow stress is decreased to 1.75 GPa. This originates from the fact, that shear transformation zones (STZs) nucleate more easily at the interfaces. Fig. 63 also shows snapshots of the atomic configurations colored according to the local atomic von Mises strain at 20% macroscopic strain. A shear band is visible in the homogeneous glass, whereas the deformation is more delocalized in the NG.

Since the aim is to delocalize the deformation in the NG without compromising strength, we replace the amorphous interface interphase by three different crystalline phases: B2 CuZr, fcc Cu and C15 Cu_2Zr. All of these phases have a higher yield strength than the homogeneous glass of composition $Cu_{61}Zr_{39}$. We thus expect, that all three phases act as a reinforcement to the overall NG composite structure. The average interface thickness in the untreated nanoglass is about 1 nm.

The mechanical properties of the NG composites are probed under the same tensile conditions as the conventional NG and the homogeneous glass. The resulting stress-strain curves are depicted in Fig. 64(a). Surprisingly, the B2 CuZr phase does not increase the strength of the NG composite with respect to the NG. When a strong crystalline backbone such as the orthogonal C15 Cu_2Zr Laves-phase is introduced into the system, however, the yield strength increases by more than 0.5 GPa. In the case of the fcc Cu reinforcement the stress-strain curve only starts to deviate

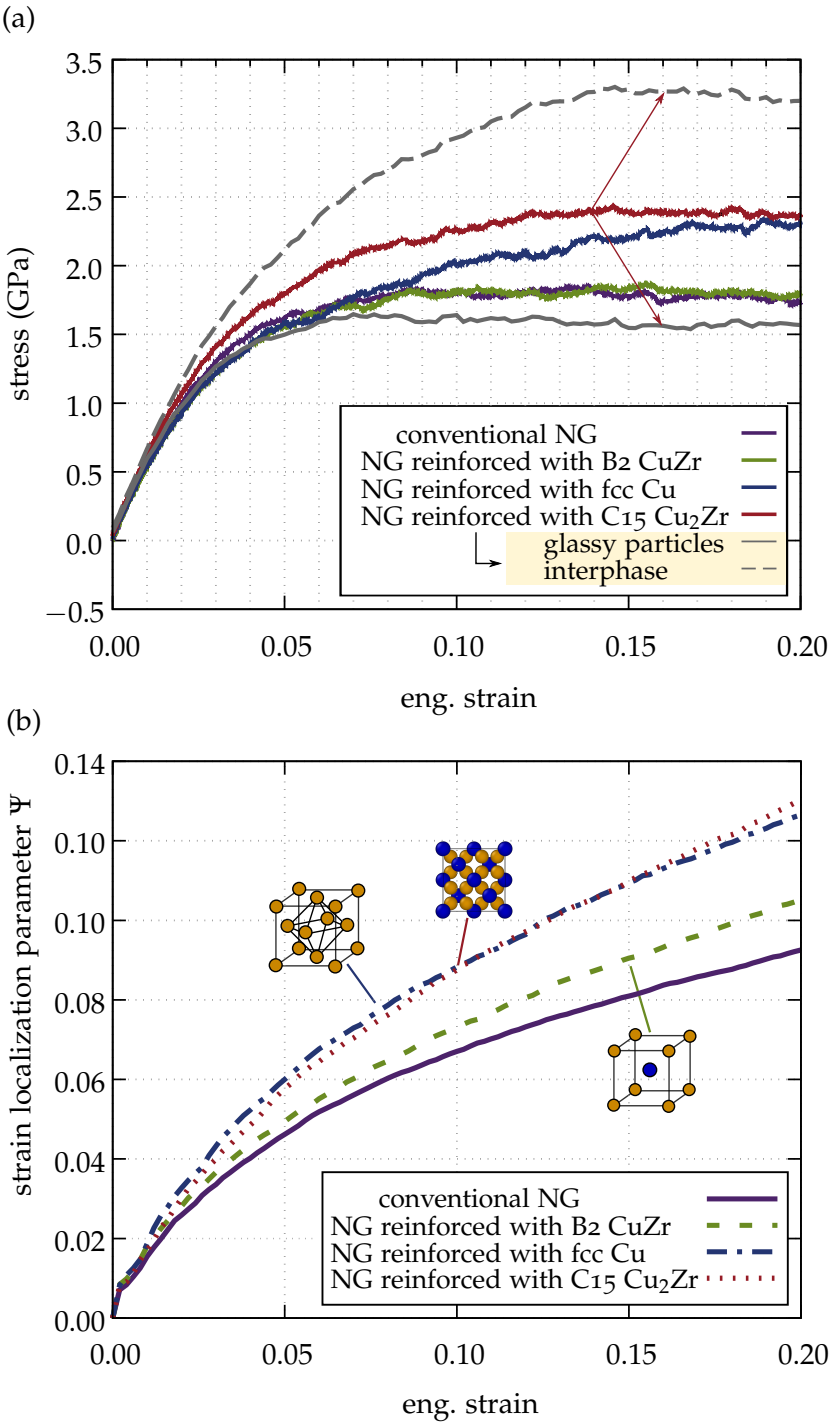

FIGURE 64: (a) Tensile tests at 50 K and constant engineering strain rate of the conventional NG and three NG composites reinforced with B2 CuZr, fcc Cu and C15 Cu_2Zr (Laves). While the B2 phase does not increase the strength of the composite, the fcc and C15 phases significantly reinforce the NG. For the composite reinforced with C15 phase, the evolution of the average von Mises stresses in the interphase and the glassy grains are depicted in grey. (b) Evolution of the strain localization parameter Ψ during deformation of the conventional NG and the reinforced NG composites. The unit cells indicate the different reinforcement types.

from the B2 CuZr NG composite at a macroscopic strain higher than 5%. Eventually, it increases to the stress level of the C15 Cu_2Zr NG composite.

In contrast to the overall stress state of the composites, the local stress state of the individual phases is not expected to be uniaxial. Thus, instead of looking at the axial stress we are analyzing the local von Mises stresses, which are relevant for plastic deformation. The gray curves in Fig. 64(a) represent the evolution of the average von Mises stresses in the interphase and glassy grains of the C15 Laves reinforced composite. Load transfer from the glassy grains to the reinforcement network can be observed.

In a next step, we investigate how the strain is accommodated by the different composites as compared to the NG. To quantify this, the strain localization parameter[169] of the different structures has been calculated via Eq. 3.18. Fig. 64(b) shows how the strain localization parameter evolves with the macroscopic strain during the tensile tests. It has been shown in earlier studies, that compared to the bulk glass, Ψ is reduced in the NG.[96] When reinforcing the grain boundaries Ψ increases again. The stronger the reinforcement phase, the higher is the degree of localization. The tensile tests show that similar to the conventional NG the reinforced NG composites do not exhibit strain localization in a dominant shear band. Hence, it can be expected, that the reinforced composites maintain their ductility. However, only the Cu and Laves phases lead to an increase in yield strength. Thus we studied in what respect the B2 CuZr interphase differs from the other ones and examined our models at the atomistic level. Fig. 65 shows snapshots of the atomic configurations of the NG composites (a) prior to and (b) during deformation. Only atoms that have been inserted as grain boundary reinforcement are shown in Fig. 65(a). Their color coding indicates their atomic structure analyzed through a CNA.[160] Note that the ideal single crystalline lattices, that initially have been introduced in the glass, would all appear in uniform color when analyzed this way. The identification of the C15 Laves phase is possible by calculating the Voronoi indices of the atoms: Cu atoms in a $\langle 0, 0, 12, 0\rangle$ polyhedron as well as Zr atoms that both reside in $\langle 0, 0, 12, 4\rangle$ polyhedra and are neighbors to a Cu-centered icosahedra are marked as yellow in Fig. 65(a).

On the one hand, it is evident that a large quantity of the B2 CuZr crystalline phase amorphizes during equilibration (synthesis of the NG composites), cf. gray atoms in upper row in Fig. 65(a). Only small clusters of crystalline phase, here colored in blue, remain intact. A separate structure analysis of the glassy grains, on the other hand, provides no evidence that the short range order of the glass has been disturbed during equilibration. This has been verified by comparing the fraction of Cu-centered icosahedra among the atoms that initially belonged to the glassy grains before and after equilibration of the NG–composites. These icosahedra are known to be the structural backbone of the glass.[169]

The partial amorphization of the crystalline phases is not completely unexpected, since the width of the NG-interphase is not much larger than 1 nm in parts, and crystalline Cu sheets of a few monolayers, e.g., are known to become unstable in a MG.[9] Furthermore, Fig. 65(a) shows that the fcc Cu-phase contains stacking faults (depicted in red) after equilibration. The strong Laves phase with its high packing

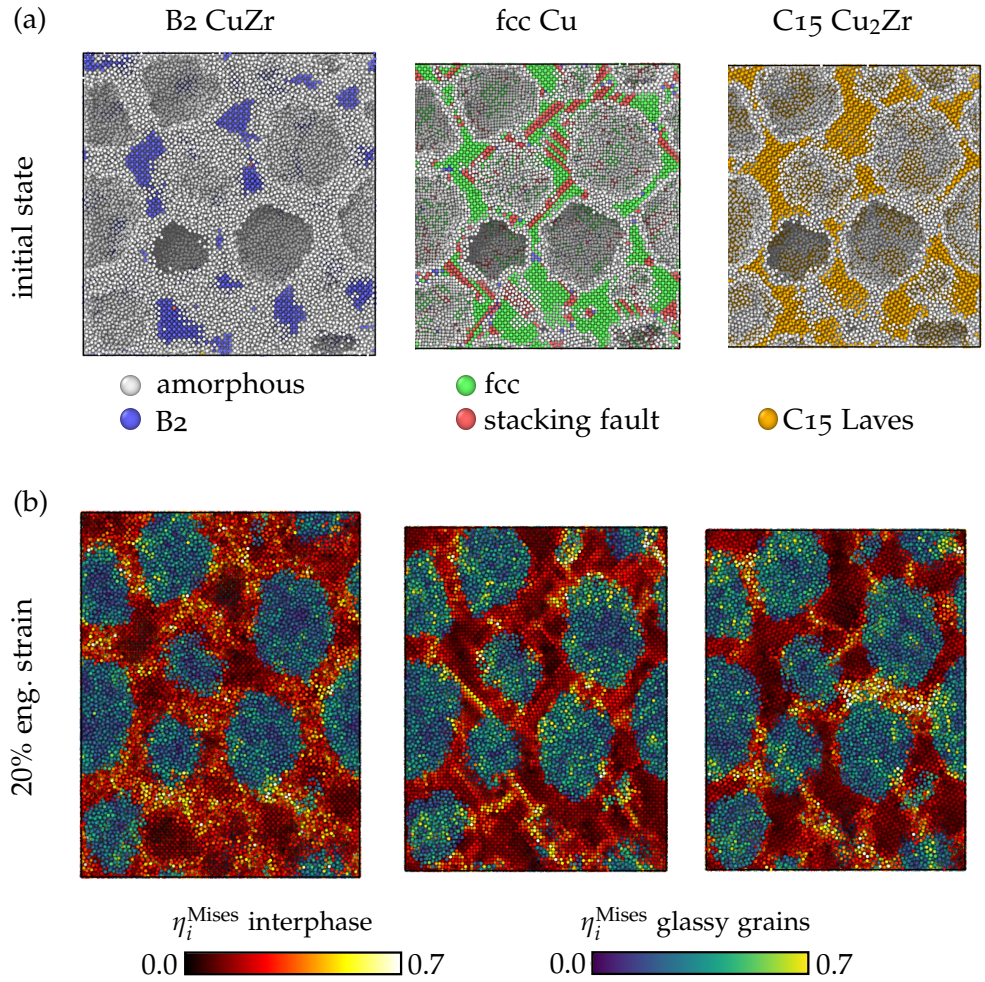

FIGURE 65: Three different types of reinforcement are used as NG interface interphase: B2 CuZr, fcc Cu and C15 Cu_2Zr. (a) NG–composites before tensile testing: The glass atoms have been removed for visualization; the atoms that initially belonged to the single crystalline interphase are color coded according to their atomic structure: blue represents the B2 structure, green fcc, red colored atoms are stacking faults in fcc, yellow are Cu and Zr atoms in the C15 Laves phase and gray means amorphous. (b) Snapshots of the atomic configurations at 20% macroscopic strain show the local atomic von Mises strain. Two different color schemes are used for the glass phase and the interface phase.

density partly amorphizes, but not as much as the inserted B2 CuZr. Another observation is that the equilibrium volumes of the three NG composites differ from another. As a result, the aggregated volume of replaced atoms in the NG composites rises to values between 48% and 58%, while the original NG had an interphase fraction of 37%. This difference in the volume fraction of inserted interphase is, however, diminished again by the fact that large quantities of the inserted phase become amorphous.

We have shown that the yield strength increases when a stable crystalline phase is used as interphase. Snapshots of the atomic configurations of the composites at 20% macroscopic strain with the atoms color coded according to the local atomic von Mises strain, see Fig. 65(b), reveal the difference in strain localization between the reinforcement phases. Two different color schemes are used for the atoms in the glassy grains and in the interphase. Analysis of the time evolution of the Mises strain distribution during deformation showed that for all composites, STZ nucleation is initiated at the interfaces, and in later stages, STZs also nucleate in the interior of the glassy grains. This is independent of the applied boundary conditions (Fig. 66). The yield stress is unaffected by simulating open surfaces and the ductility does not decrease either. In case of almost fully amorphized B2, there also is promotion of STZs inside the interphase, explaining why the mechanical response to straining is very similar to the one of the conventional NG. The remaining CuZr B2 crystalline parts in the reinforcement phase stay intact during deformation, because the surrounding glass phase simply flows around. As for the

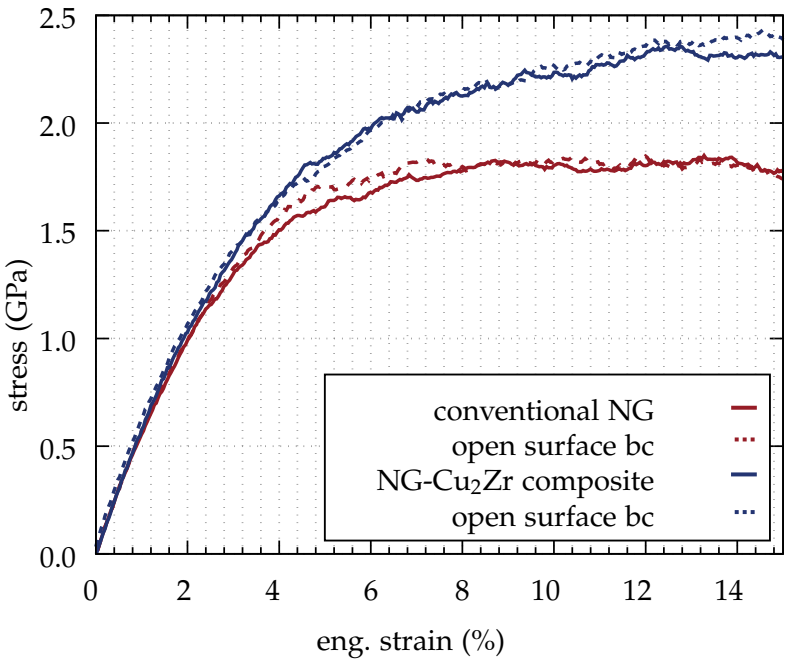

FIGURE 66: Comparison of stress-strain curves of the conventional NG and the reinforced NG studied using 2d-periodic and 3d-periodic boundary conditions.

NG composite with Cu reinforcement, the deformation of the interphase is carried by dislocation activity, visible as slip traces in the von Mises strain field in Fig. 65(b). In the reinforcement phase of type C15 Laves, the nucleation stress for dislocations is higher than in fcc Cu, thus we observe STZs forming in the amorphous parts of the interphase rather than dislocation activity. Like in the conventional NG, shear band formation is suppressed in the NG composites. However, the increase of the strain localization parameter in these structures is due to concentration of the deformation in the interphase. This is especially the case for the fcc Cu reinforcement, where we observe a change in the dominating mechanism from STZ nucleation to dislocation slip, leading to strain hardening, similar to the behavior of a metal matrix composite.

9.3 CREEP BEHAVIOR OF REINFORCED NG

The results presented in this section have been obtained in collaboration with Dr. Omar Adjaoud, who performed the creep simulations of the homogeneous MG and the conventional NG sample.

The 50 K tensile tests showed that the introduction of Laves phase leads to a strong increase in yield strength while the ductility of the NG is maintained. Again, this raises the question if this is still valid at increased temperatures and under an elastostatic load. In contrast to the MG composite models presented before, the continuous phase in the NG composites is now the crystalline phase and the glassy particles are embedded therein. We performed several creep simulations at different temperatures but constant stress with the Laves phase reinforced NG-composite. For comparison, a homogeneous $Cu_{64}Zr_{36}$ glass sample and the cold-compacted NG with the same nominal composition have been probed under creep conditions as well.

Starting with a comparison of the creep behavior of the homogeneous glass and the conventional NG, presented in Figures 68(a) and (b) it is evident, that the NG microstructure promotes creep. Even at room temperature, the conventional NG exhibits viscoelastic creep behavior and reaches a total creep strain of more than 4% after 50 ns elastostatic loading at 750 MPa. Adjaoud and Albe have shown, that the cold-compacted NG used in this study, features a defective short-range order in the interphase.[95] Therefore, it is reasonable to assume a lowered activation energy for creep within the interphase region and thus the increased creep activity. This is also supported by Figures 69(a) and (b) that depict the local von Mises strain field in the homogeneous glass and the conventional NG after 40 ns of creep deformation. Compared to homogeneous MG, there clearly is increased STZ activity in the whole sample, but even more so in the interphase. The homogeneous MG exhibits the behavior already described in Ch. 4. The reasoning behind repeating the study of homogeneous samples is that this specific sample has been used to generate the glassy grains, that were annealed above T_g and then cold compacted to form the segregated NG, as described in Ref. 95.

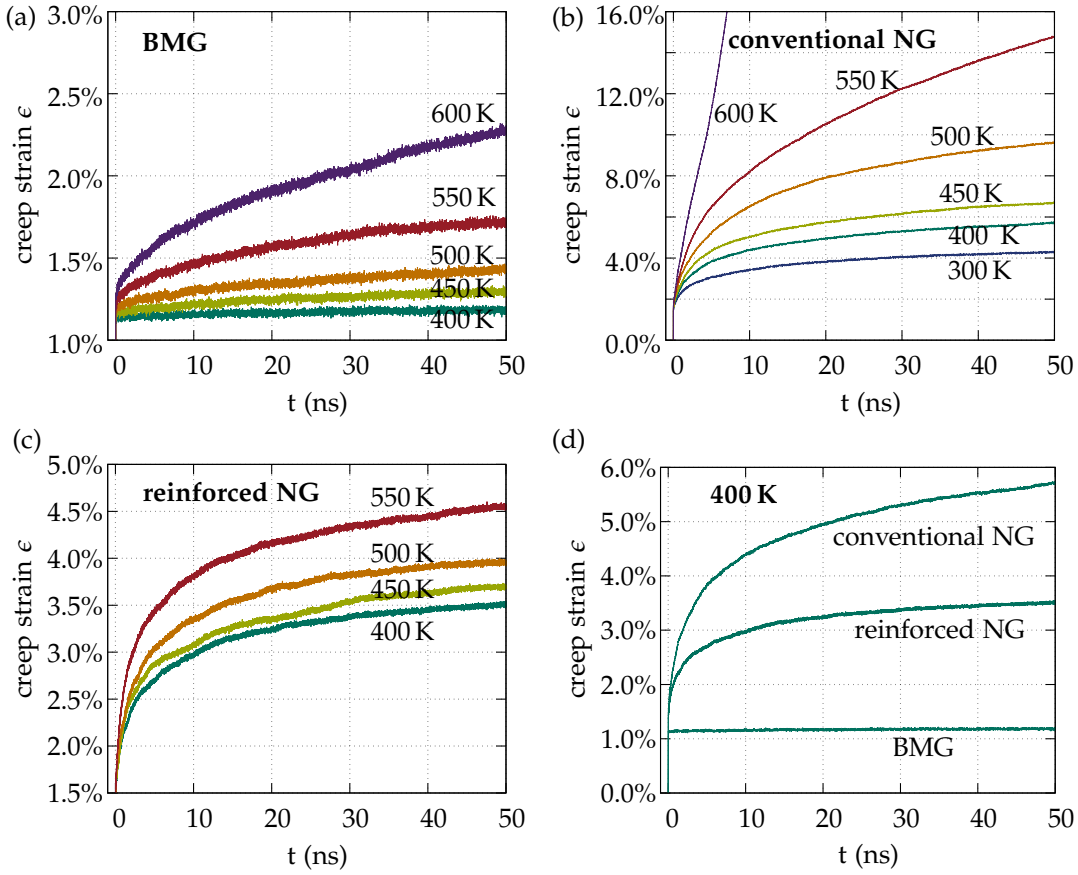

FIGURE 67: Creep curves for uniaxial elastostatic loading at 750 MPa of (a) a homogeneous $Cu_{64}Zr_{36}$ MG, (b) a conventional NG with nominal composition $Cu_{64}Zr_{36}$ and (c) an interphase reinforced NG-composite. (d) For comparison, the 400 K creep curves of the BMG, NG and reinforced NG are shown.

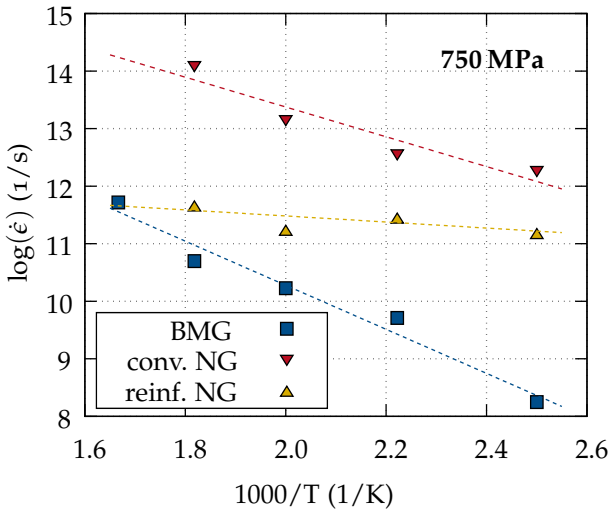

FIGURE 68: Temperature dependence of the creep rates of the BMG, NG and reinforced NG fitted between 25 ns and 50 ns.

Now, the creep compliance of the Laves phase reinforced NG ranges in between those of the homogeneous glass and the conventional NG, see Figure 68(c). The total creep strain reached after 50 ns of creep at $T = 500\,\mathrm{K}$ is 4%, which is less than half the creep strain the conventional NG did reach for that temperature and 2.6% more than observed for the homogeneous glass. The shape of the creep curves of the reinforced NG resemble more closely the shape of the creep curves of the conventional NG, since both feature high creep rates in the initial creep stage.

Analogous, to the analyses performed in previous chapters, we performed linear fits to the creep data between $t = 25\,\mathrm{ns}$ and $t = 50\,\mathrm{ns}$, for comparison of the creep rates in the three different glass types. The data is collected in Figure 68(d), that gives the temperature dependence of the creep rates at constant stress of 750 MPa. As a guide to the eye, a linear fit has been plotted for each data set. For the BMG and the NG, the slopes differ slightly. One reason is that the slope is not simply the activation energy for creep but also includes the stress dependency [cf. Eq. 2.5]. Also, as discussed in the previous chapters, the errorbars of the fitted creep rates are non-negligible. However, since the creep mechanism, more precisely the STZs in the NG and BMG are the same, we can attribute the offset in the creep rates to the different STZ nucleation densities of these two systems.

As for the reinforced NG, it is evident that the temperature dependence of the creep rates fitted between $t = 25\,\mathrm{ns}$ and $t = 50\,\mathrm{ns}$ is not as pronounced as for the other two cases. Especially for higher temperatures, the rates approach the lower limiting case exhibited by the homogeneous glass. An explanation for this can be found in the von Mises strain field of the NG-composite after 40 ns of creep deformation, as shown in Figure 69(c): During creep of the NG-composite, most of the crystalline phase again only responds elastically. But the glassy grains embedded therein start to flow. It seems that, at the temperature of $400\,\mathrm{K} \leq T \leq 550\,\mathrm{K}$, the major fraction of glass phase already participates in the deformation. Thus,

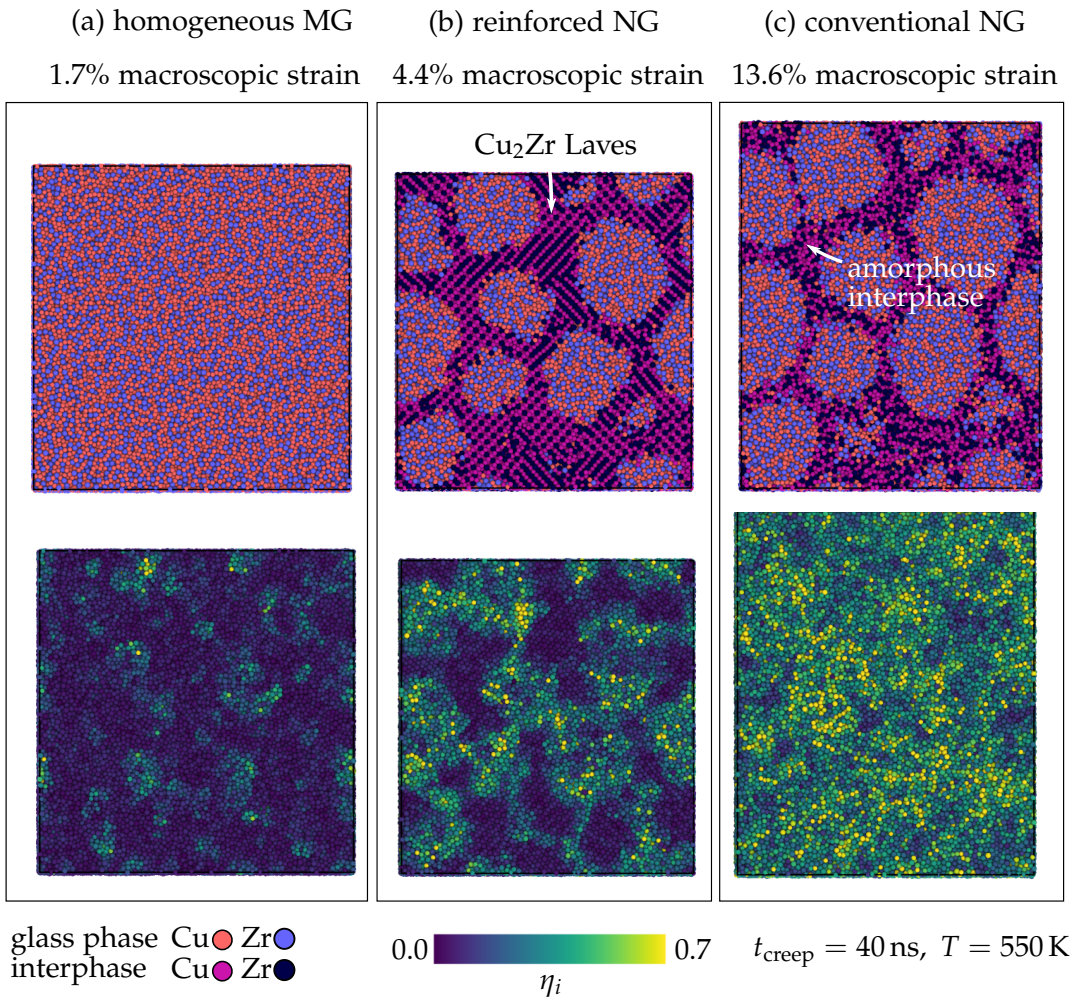

FIGURE 69: Snapshots of the atomic configurations of the (a) homogeneous glass, (b) conventional NG and (c) reinforced NG samples after 40 ns of creep at 550 K, color coded according to their particle type (top row) and according to the local von Mises strain (bottom row).

the weak temperature dependence. Moreover, the elevated temperatures, probably enhances the stabilization of the artificially created Cu_2Zr–MG interfaces. To conclude, the reinforcing effect of the Laves phase still prevails under the here applied creep conditions.

9.4 CONCLUSION

We showed that grain boundary strengthening of NGs is possible by manipulating the amorphous interphase that forms during cold compaction of glassy spheres. In our generic NG models we inserted stronger crystalline phases as grain boundary reinforcement and observed a significant increase in 50 K yield strength when the phase remained stable in the composite. This is because the crystalline interphase network becomes the load bearing component and the yield stress is determined by the nucleation stress of dislocations. The suggested strategy of reinforcing the grain boundary phase in a NG could be a promising way of synthesizing ductile NGs that retain or even exceed the strength of their bulk homogeneous counterparts if, in the future, it becomes possible to selectively manipulate the interface interphase in a NG. In potential experiments this could maybe be realized by surface treatment of the as-prepared glassy nanoparticles.

Concerning the creep behavior of NGs and NG-composites, we could show that the glass-glass interfaces in the cold-compacted NG facilitate STZ activation and thus creep. The crystalline continuous Laves-phase network in the NG-composite, on the contrary, also reinforced the NG-composite against creep at higher temperatures.

Part IV

CONCLUSION

SUMMARY

In this thesis we have studied the low-temperature creep behavior of a homogeneous $Cu_{64}Zr_{36}$ metallic glass, different metallic glass-crystal composites and Cu–Zr nanoglasses by means of molecular dynamics. In the following we would like to summarize the key findings of this work.

HOMOGENEOUS GLASS

- **Creep deformation of MGs can be studied by means of molecular dynamics.** Even in the low-temperature ($0.5T_g \leq T \leq 0.7T_g$) and low-stress ($\sigma < 0.5\ \sigma_y$) regimes creep strains of up to 2% could be observed on timescales of 40 nanoseconds. The propensity to flow is high since a large fraction of the barriers for creep deformation are thermally activated even on the limited time scales studied here.

- **Metallic glasses exhibit viscoelastic creep behavior.** The mechanistic picture behind creep deformation in MGs is the same as for plastic deformation at low-temperatures, i.e. the formation of shear transformation zones. They nucleate homogeneously throughout the sample.

- **The creep rate dependence on temperature and stress can be described by Argon's deformation model for homogeneous deformation.**[65] By fitting Eq. 2.5 to our creep data we obtain a creep activation energy of 0.67 eV and STZ size of approximately 51 atoms.

- **Sub-T_g zero-load annealing yields a deeply relaxed glass**. When probed under conventional tensile tests, these glasses exhibit inhomogeneous deformation through shear bands even at room temperature. Ultimately, these deeply relaxed glasses might be better comparable to the experimental situation.

- **During long-time creep deformation below T_g there is a competition between aging/relaxation and rejuvenation.** Similar to the case of load-free annealing, the energy relaxation follows a stretched exponential function. Applying a constant uniaxial tensile load, however, seems to slightly rejuvenate the sample with respect to the load-free case as visible from the final potential energies of the differently treated samples.

- **Thermo-mechanical pretreatment by uniaxial creep loading causes the metallic glass to exhibit an anisotropic mechanical response.** We did not find structural evidence for this in the form of a bond-length-anisotropy as postulated by others.[11,63,175] Although significant changes in the chemical short range order of the icosahedral units occur during creep, this does not

fully explain the energy difference between the crept and load-free annealed samples.

- **Elasto- and hydrostatic cyclic loading at $0.65T_g$ leads to aging of the $Cu_{64}Zr_{36}$ homogeneous glass accompanied by an increased yield strength.** Opposite to results of studies on network glasses,[176] hydrostatic pressure cycling below the yield, does not accelerate the relaxation process of our metallic glass (compared to load-free annealing at the same temperature). On the contrary, the pressure cycling leads to an energetically rejuvenated sample with respect to a load-free annealed one.

  All these findings give evidence that even in the apparent "elastic" regime, metallic glasses are prone to undergo structural changes, especially when they are not well relaxed as it is the case for computer samples.

GLASS-CRYSTAL COMPOSITES

Secondary phase: CuZr

- **The secondary phase made of bcc-CuZr only reacts elastically at the creep strains attainable in our simulations.** Independent of the shape of the secondary phase, e.g. continuous network phase or spherical precipitates, the plastic creep deformation is carried by the glass phase, which from a simplified viewpoint "flows around" the crystalline phase.

- **Unrelaxed glass–crystal interfaces in our virtual composites become a weakpoint during creep loading.** In computational modeling, the most common route to creating composite models is to “cut” out the desired volume fraction and shape of secondary phase from the glass matrix and "fill" it with crystalline phase. The risk is however, that the resulting glass-crystal interfaces are non-physical. Even after thorough equilibration such artificially created interfaces act as preferential nucleation sites for STZs which leads to increased creep deformation of these composites.

- **The creep compliance of the composites scales with the glass–crystal interface area.** In our virtual models we can vary the interface area of the crystalline secondary phase, but at the same time keep the secondary phase geometry and volume fraction constant. Creep experiments of composites that only differ by their interface area show that the higher the interface area, the higher is the resulting total creep strain and the creep rate.

- **The creep rate of the composite also depends on the secondary phases geometry.** By varying the shape of the secondary phase at both constant volume fraction and interface area, we find that the orientation of the glass-crystal surfaces influences the creep rates. This can be rationalized in terms of a Schmid-like orientation dependence of the resolved shear stresses in the interfaces with respect to the loading direction.

Secondary phase: Cu_2Zr

- **In the case of stable, in-situ formed interfaces, the mechanical properties at elevated temperatures do not deteriorate.** Although Cu_2Zr Laves phases do not appear below T_g in the real equilibrium CuZr phase diagram, it is known that the Mendelev potential is able to stabilize this phase at lower temperatures. These samples serve as generic models of energetically stable and strong composites: As-grown precipitates of *C*15 and *C*14 Laves phases increase the creep resistance of the MG-crystal composite. This is both due to the relaxation of the glass matrix and the beneficial properties of the crystalline phase. The analysis of the atomic Kelvin shear moduli of the three phases - glass matrix, crystal and interface - shows hat the stiffness of the interface ranges in between values found for the glass matrix and those exhibited by the stiff crystallites.

- **The creep rate scales exponentially with the excess energy in the composites' interfaces.** By disturbing the chemical short range order in the stable interfaces between the glass matrix and the Laves phase, we control the interface properties, here characterized in terms of excess energy with respect to the untreated sample. A correlation between the excess energy in the disturbed samples and the relative creep rates is found that resembles models for grain boundary diffusion in nanocrystalline materials.[113,114]

NANOGLASSES AND NANOGLASS-COMPOSITES

- **Glass-glass interfaces in nanoglasses enhance creep.** Due to the defective short range order in the amorphous interface phase present in nanoglasses, the latter are much more prone to creep as their homogeneous counterparts. During room temperature creep deformation a total creep strain of 4% could be reached on timescales of 50 ns.

- **Nanoglasses can be reinforced through their interphase network.** Reinforcement is possible by replacing the continuous amorphous interphase with the strong Cu_2Zr Laves phase, that itself forms stable interfaces with the glassy particles. This type of reinforcement becomes the load-bearing component of the nanoglass-composite and also reinforces the nanoglass-composites against creep.

OUTLOOK

Firstly, to come back again to the simulations performed in this work, several issues have opened the way for further studies:

- The possibility of using cyclic loading in simulations, to drive the MG into a deeply relaxed state should be explored in more detail. In Ch. 6 the cyclic loading procedure has only been performed at a single pressure and temperature (in the elastic limit) but at other stress and temperature ranges the cycling could have a more pronounced effect.

- Further, we have shown that an increase in FI coordination is not always correlated with an potential energy reduction, at least when comparing different samples. Here, the role of the chemical short range order of the coordination polyhedra sharing the same Voronoi indices should be investigated in more detail, especially the distribution of their energies.

- For the creep studies of MG-crystal composites we have explored different ways of constructing computer models of dual-phase structures. By design, the secondary phase only exhibited an elastic response to the elastostatic straining and did not participate in creep deformation. First of all, other crystalline phases than fcc Cu or the B2 CuZr could be considered here. Second, interatomic potentials are needed that not only describe well the glass phase but also more features of crystalline phases, e.g. the experimentally observed martensitic phase transformation of the B2 CuZr since it might lead to strain hardening during creep.

- The NG-composite models were constructed by replacing the grain boundary phase with single crystalline phase. In the case of the stable Cu_2Zr this worked well, however, it might be interesting to also explore polycrystalline interphase structures. This could be for instance realized by repeating our insertion method but starting from a bulk polycrystal instead of a single crystal. An even more elaborate way to simulate realistic interphase structures could also be to selectively melt and quench only the interphase. In this context it might also be worth to consider selective long-time annealing of the interphase close to T_g. In that way, crystallization of the very stable Laves-type within the amorphous interphase could be enforced.

Secondly - viewed from a broader perspective - this work has treated a variety of glass- and glass-crystal composite microstructures, ranging from bulk homogeneous glasses over continuous glassy matrices with secondary phase inclusions to the completely opposite case where glassy nanoparticles were embedded in a rigid

grain boundary phase. While nanoscale heterogeneities in MGs are no new concept, percolating structures like the interpenetrating network phase studied here or the reinforced NG are yet to be realized experimentally. Maybe processes could be imaginable where a metallic glass is cast into a crystalline metallic foam, or where crystallization of the surfaces of the NG precursor particles is induced.

For non-metallic glass-composites these interpenetrating microstructures already exist, e.g. in amorphous silicon-oxycarbide glass-ceramics. Within the silica matrix carbon can exist both in the form of β-SiC nanoparticles or as segregated carbon network formed of graphene-like layers.[130,131] In both cases the amorphous-crystalline interfaces are a key factor in the high-temperature creep behavior.[189,190] The transfer of the present results to this different material system may be difficult, ultimately an interatomic potential is needed that better describes this amorphous glass-ceramic composites, to be able to study the mechanism behind their creep deformation.

ERKLÄRUNG – DISCLAIMER

Hiermit versichere ich, die vorliegende Dissertation ohne Hilfe Dritter nur mit den angegebenen Quellen und Hilfsmitteln angefertigt zu haben. Alle Stellen, die aus Quellen entnommen wurden, sind als solche kenntlich gemacht. Diese Arbeit hat in gleicher oder ähnlicher Form noch keiner Prüfungsbehörde vorgelegen.

Darmstadt, den 9. Oktober 2018

Constanze Kalcher

DANKSAGUNG – ACKNOWLEDGMENTS

First of all I would like to thank Prof. Karsten Albe as well as the project leaders Dr. Alexander Stukowski and Dr. Jochen Rohrer for giving me the opportunity and trust to be part of your team. It has been a privilege to work with and learn from each of you. I would also like to thank Prof. Erik Bitzek, Prof. Martin Heilmaier and Prof. Ralf Riedel for reviewing this thesis.

This research was funded trough Deutsche Forschungsgemeinschaft (DFG) through projects STU 611/1-1 and RO 4542/2-1. Moreover, I would like to acknowledge the funding I received through the Starting Ramp Program of SPP 1594. Calculations for this research were conducted on the Lichtenberg high performance computer of the TU Darmstadt.

I'm deeply grateful for all the help I received from Dr. Omar Adjaoud und Dr. Tobias Brink, the "metallic glass experts". Thank you for providing me with the metallic glass and nanoglass models that are the basis of the composites studied in this thesis. Alex and Tobias, a sincere thank you for all your patience and enthusiasm when it came to teaching about python, c++, and OVITO analysis scripts.
I've always taken pride in being a part of the Materials Modeling Division, the "MM's" and this is due its each and every member I've had the chance to encounter during my education here - whether as a student, teacher or colleague and friend. So instead of giving a lengthy list of names here, please know that I wouldn't have had such a great experience without you.

Bei meiner Familie, insbesondere bei meinen Eltern möchte ich mich für all die liebevolle Unterstützung bedanken ohne die ich heute nicht hier wäre. Danke für eure unendliche Geduld, eine Promotion ist gewiss ein ziemlich egoistisches Abenteuer. Danke Marcus. Einfach für Alles.

Curriculum Vitae

Research Experience

since 06/2014 **Research Associate** (Wissenschaftliche Mitarbeiterin)
Materials Modeling Division of Prof. Dr. rer. nat. Karsten Albe,
Technische Universität Darmstadt, Germany

University Education

06/2014 **M. Sc.** in Materials Science, Technische Universität Darmstadt

08/2012-06/2013 University of Illinois at Urbana-Champaign, USA

09/2011 **B. Sc.** in Materials Science, Technische Universität Darmstadt

Peer Reviewed Articles (related to Thesis)

A1 C. Kalcher, O. Adjaoud, J. Rohrer, A. Stukowski, K. Albe, *Reinforcement of nanoglasses by interface strengthening*, Scripta Materialia **141**, 115–119 (2017)

A2 C. Kalcher, T. Brink, J. Rohrer, A. Stukowski, K. Albe, *Interface-controlled creep in metallic glass composites*, Acta Materialia **141**, 251–260 (2017)

Peer Reviewed Articles (not related to Thesis)

B1 D. Vrankovic, M. Graczyk-Zajac, C. Kalcher, J. Rohrer, M. Becker, C. Stabler, G. Trykowski, K. Albe, Riedel R. *Highly Porous Silicon Embedded in a Ceramic Matrix: A Stable High-Capacity Electrode for Li-Ion Batteries*, ACS Nano **11**, 11409–11416, (2017)

B2 S. Sicolo, C. Kalcher, S. J. Sedlmaier, J. Janek, K. Albe, *Diffusion mechanism in the superionic conductor Li4PS4I studied by first-principles calculations*, Solid State Ionics **319**, 83–91, (2018)

B3 A. Grünebohm, Y.-B. Ma, M. Marathe, B.-X. Xu, K. Albe, C. Kalcher, K.-C. Meyer, V. Shvartsman, D. Lupascu, C. Ederer, *Origins of the inverse electrocaloric effect*, Energy Technology **6**, 1491–1511 (2018)

Oral Presentations at International Conferences

ISAF 2015 Darmstadt, "Electrocaloric effect in model ferroelectrics: Indirect vs. direct analysis of materials with first and second order phase transitions", Constanze Kalcher, and Karsten Albe

DPG 2016 Regensburg, "Creep of Cu-Zr glass composites studied by Molecular Dynamics simulations", Constanze Kalcher, Tobias Brink, Alexander Stukowski, and Karsten Albe

DPG 2016 Regensburg, "Direct vs indirect Monte-Carlo methods for calculating the electrocaloric effect", Constanze Kalcher, Alexander Stukowski, and Karsten Albe

DPG 2016 Regensburg, "Abnormal electrocaloric effect studied by lattice based Monte-Carlo simulations", Kai-Christian Meyer, Constanze Kalcher, Alexander Stukowski, and Karsten Albe

DPG 2017 Dresden, "Interface controlled plasticity in metallic crystal-glass composites", Constanze Kalcher, Tobias Brink, Omar Adjaoud, and Karsten Albe

TMS 2017, San Diego (USA), "Molecular Dynamics Study of the Creep Behavior of Metallic Glasses and Glass-composites", Constanze Kalcher, Tobias Brink, Jochen Rohrer, Alexander Stukowski, and Karsten Albe

DPG 2018 Berlin, "Interface mediated creep behavior of Cu-Zr metallic glass composites", Constanze Kalcher, Tobias Brink, and Karsten Albe

Darmstadt, 2018

BIBLIOGRAPHY

[1] W. Klement, R. H. Willens, and P. Duwez, *Non-crystalline structure in solidified gold–silicon alloys*, Nature **187**, 869–870 (1960).

[2] C. A. Schuh, T. C. Hufnagel, and U. Ramamurty, *Mechanical behavior of amorphous alloys*, Acta Materialia **55**, 4067–4109 (2007).

[3] J. F. Löffler, *Bulk metallic glasses*, Intermetallics **11**, 529–540 (2003).

[4] A. L. Greer, *Metallic glasses... on the threshold*, Materials today **12**, 14–22 (2009).

[5] C. C. Hays, C. P. Kim, and W. L. Johnson, *Microstructure controlled shear band pattern formation and enhanced plasticity of bulk metallic glasses containing in situ formed ductile phase dendrite dispersions*, Physical Review Letters **84**, 2901–2904 (2000).

[6] C. C. Hays, C. P. Kim, and W. L. Johnson, *Improved mechanical behavior of bulk metallic glasses containing in situ formed ductile phase dendrite dispersions*, Materials Science and Engineering A **304–306**, 650–655 (2001).

[7] J. Eckert, J. Das, S. Pauly, and C. Duhamel, *Mechanical properties of bulk metallic glasses and composites*, Journal of Materials Research **22**, 285–301 (2007).

[8] K. Hajlaoui, A. R. Yavari, A. LeMoulec, W. J. Botta, F. G. Vaughan, J. Das, A. L. Greer, and Å. Kvick, *Plasticity induced by nanoparticle dispersions in bulk metallic glasses*, Journal of Non-Crystalline Solids **353**, 327–331 (2007).

[9] T. Brink, M. Peterlechner, H. Rösner, K. Albe, and G. Wilde, *Influence of crystalline nanoprecipitates on shear-band propagation in Cu–Zr-based metallic glasses*, Physical Review Applied **5**, 054005 (2016).

[10] Y. Tong, W. Dmowski, Y. Yokoyama, G. Wang, P. K. Liaw, and T. Egami, *Recovering compressive plasticity of bulk metallic glasses by high-temperature creep*, Scripta Materialia **69**, 570–573 (2013).

[11] Y. Tong, T. Iwashita, W. Dmowski, H. Bei, Y. Yokoyama, and T. Egami, *Structural rejuvenation in bulk metallic glasses*, Acta Materialia **86**, 240–246 (2015).

[12] J. Ding, S. Patinet, M. L. Falk, Y. Cheng, and E. Ma, *Soft spots and their structural signature in a metallic glass*, Proceedings of the National Academy of Sciences **111**, 14052–14056 (2014).

[13] S. V. Ketov, Y. H. Sun, S. Nachum, Z. Lu, A. Checchi, A. R. Beraldin, H. Y. Bai, W. H. Wang, D. V. Louzguine-Luzgin, M. A. Carpenter, and A. L. Greer,

Rejuvenation of metallic glasses by non-affine thermal strain, Nature **524**, 200–203 (2015).

[14] Z. Mahbooba, L. Thorsson, M. Unosson, P. Skoglund, H. West, T. Horn, C. Rock, E. Vogli, and O. Harrysson, *Additive manufacturing of an iron-based bulk metallic glass larger than the critical casting thickness*, Applied Materials Today **11**, 264–269 (2018).

[15] M. D. Ediger, C. A. Angell, and S. R. Nagel, *Supercooled liquids and glasses*, The Journal of Physical Chemistry **100**, 13200–13212 (1996).

[16] R. Busch, A. Masuhr, and W. L. Johnson, *Thermodynamics and kinetics of Zr-Ti-Cu-Ni-Be bulk metallic glass forming liquids*, Materials Science and Engineering: A **304-306**, 97–102 (2001).

[17] A. Inoue, T. Nakamura, N. Nishiyama, and T. Masumoto, *Mg-Cu-Y bulk amorphous alloys with high tensile strength produced by a high-pressure die casting method*, Materials Transactions, JIM **33**, 937–945 (1992).

[18] W. H. Wang, C. Dong, and C. H. Shek, *Bulk metallic glasses*, Modelling and Simulation in Materials Science and Engineering: R: Reports **44**, 45–89 (2004).

[19] A. Peker and W. L. Johnson, *A highly processable metallic glass: $Zr_{41.2}Ti_{13.8}Cu_{12.5}Ni_{10.0}Be_{22.5}$*, Applied Physics Letters **63**, 2342–2344 (1993).

[20] M. Launey, R. Busch, and J. Kruzic, *Influence of structural relaxation on the fatigue behavior of a ZrTiNiCuBe bulk amorphous alloy*, Scripta Materialia, 483–487 (2005).

[21] D. Wang, Y. Li, B. B. Sun, M. L. Sui, K. Lu, and E. Ma, *Bulk metallic glass formation in the binary Cu-Zr system*, Applied Physics Letters **84**, 4029–4031 (2004).

[22] M. I. Mendelev, D. J. Sordelet, and M. J. Kramer, *Using atomistic computer simulations to analyze X-ray diffraction data from metallic glasses*, Journal of Applied Physics **102**, 043501 (2007).

[23] M. I. Mendelev, M. J. Kramer, R. T. Ott, D. J. Sordelet, D. Yagodin, and P. Popel, *Development of suitable interatomic potentials for simulation of liquid and amorphous Cu-Zr alloys*, Philosophical Magazine **89**, 967–987 (2009).

[24] Y. Ritter, *Molecular dynamics simulations of structure-property relationships in Cu-Zr metallic glasses*, Ph.D. thesis, Technische Universität Darmstadt, 2011.

[25] T. Brink, *Heterogeneities in metallic glasses: Atomistic computer simulations on the structure and mechanical properties of copper–zirconium alloys and composites*, Ph.D. thesis, Technische Universität Darmstadt, 2017.

[26] F. Spaepen and D. Turnbull, *Metallic glasses*, Annual Review of Physical Chemistry **35**, 241–263 (1984).

[27] I. Gallino and R. Busch, *Relaxation pathways in metallic glasses*, JOM Journal of the Minerals Metals and Materials Society **69**, 2171–2177 (2017).

[28] C. A. Angell, *Formation of glasses from liquids and biopolymers*, Science **267**, 1924–1935 (1995).

[29] C. A. Angell, *Glass-formers and viscous liquid slowdown since David Turnbull: Enduring puzzles and new twists*, MRS Bulletin **33**, 544 (2008).

[30] Z. Evenson and R. Busch, *Enthalpy recovery and free volume relaxation in a $Zr_{44}Ti_{11}Ni_{10}Cu_{10}Be_{25}$ bulk metallic glass*, Journal of Alloys and Compounds **509**, S38–S41 (2011).

[31] R. Busch and I. Gallino, *Kinetics, thermodynamics, and structure of bulk metallic glass forming liquids*, JOM Journal of the Minerals Metals and Materials Society **69**, 2178–2186 (2017).

[32] G. P. Johari and M. Goldstein, *Viscous liquids and the glass transition. II. secondary relaxations in glasses of rigid molecules*, The Journal of Chemical Physics **53**, 2372–2388 (1970).

[33] F. H. Stillinger, *A topographic view of supercooled liquids and glass formation*, Science **267**, 1935–1939 (1995).

[34] P. G. Debenedetti and F. H. Stillinger, *Supercooled liquids and the glass transition*, Nature **410**, 259–267 (2001).

[35] Y. Fan, T. Iwashita, and T. Egami, *How thermally activated deformation starts in metallic glass*, Nature Communications, 5083 (2014).

[36] J. S. Harmon, M. D. Demetriou, W. L. Johnson, and K. Samwer, *Anelastic to plastic transition in metallic glass-forming liquids*, Physical Review Letters **99**, 135502 (2007).

[37] H.-B. Yu, W.-H. Wang, and K. Samwer, *The β relaxation in metallic glasses: An overview*, Materials Today **16**, 183–191 (2013).

[38] D. Turnbull and M. H. Cohen, *Free-volume model of the amorphous phase: Glass transition*, The Journal of Chemical Physics **34**, 120–125 (1961).

[39] D. Turnbull and M. H. Cohen, *On the free-volume model of the liquid-glass transition*, The Journal of Chemical Physics **52**, 3038–3041 (1970).

[40] Frans Spaepen, *Homogeneous flow of metallic glasses: A free volume perspective*, Scripta Materialia **54**, 363–367 (2006).

[41] T. Egami, *Atomic level stresses*, Progress in Materials Science **56**, 637–653 (2011).

[42] A. Slipenyuk and J. Eckert, *Correlation between enthalpy change and free volume reduction during structural relaxation of $Zr_{55}Cu_{30}Al_{10}Ni_5$ metallic glass*, Scripta Materialia **50**, 39–44 (2004).

[43] T. Egami, *Structural relaxation in metallic glasses*, Annals of the New York Academy of Sciences **371**, 238–251 (1981).

[44] M. R. J. Gibbs, J. E. Evetts, and J. A. Leake, *Activation energy spectra and relaxation in amorphous materials*, Journal of Materials Science **18**, 278–288 (1983).

[45] Y.-Q. Cheng and E. Ma, *Atomic-level structure and structure–property relationship in metallic glasses*, Progress in Materials Science **56**, 379–473 (2011).

[46] L. C. E. Struik, *Physical aging in amorphous glassy polymers*, Annals of the New York Academy of Sciences **279**, 78–85 (1976).

[47] Y. Yokoyama, T. Yamasaki, P. K. Liaw, and A. Inoue, *Study of the structural relaxation-induced embrittlement of hypoeutectic Zr-Cu-Al ternary bulk glassy alloys*, Acta Materialia **56**, 6097–6108 (2008).

[48] G. Kumar, D. Rector, R. D. Conner, and J. Schroers, *Embrittlement of Zr-based bulk metallic glasses*, Acta Materialia **57**, 3572–3583 (2009).

[49] A. Castellero, B. Moser, D. I. Uhlenhaut, F. H. Dalla Torre, and J. F. Löffler, *Room-temperature creep and structural relaxation of Mg-Cu-Y metallic glasses*, Acta Materialia **56**, 3777–3785 (2008).

[50] J. C. Phillips, *Stretched exponential relaxation in molecular and electronic glasses*, Reports on Progress in Physics **59**, 1133 (1996).

[51] R. C. Welch, J. R. Smith, M. Potuzak, X. Guo, B. F. Bowden, T. J. Kiczenski, Douglas C. Allan, E. A. King, A. J. Ellison, and J. C. Mauro, *Dynamics of glass relaxation at room temperature*, Physical Review Letters **110**, 265901 (2013).

[52] B. Ruta, G. Baldi, Y. Chushkin, B. Ruffle, L. Cristofolini, A. Fontana, M. Zanatta, and F. Nazzani, *Revealing the fast atomic motion of network glasses*, Nature Communications **5**, 3939 (2014).

[53] Y. Yu, M. Wang, M. M. Smedskjaer, J. C. Mauro, G. Sant, and M. Bauchy, *Thermometer effect: Origin of the mixed alkali effect in glass relaxation*, Physical Review Letters **119**, 095501 (2017).

[54] B. Ruta, Y. Chushkin, G. Monaco, L. Cipelletti, E. Pineda, P. Bruna, V. M. Giordano, and M. Gonzalez-Silveira, *Atomic-scale relaxation dynamics and aging in a metallic glass probed by X-ray photon correlation spectroscopy*, Physical Review Letters **109**, 165701 (2012).

[55] I. Gallino, D. Cangialosi, Z. Evenson, L. Schmitt, S. Hechler, M. Stolpe, and B. Ruta, *Activation energy spectrum for relaxation and polyamorphism in an ultraviscous metallic glass former*, arXiv:1706.03830 (2017).

[56] I. Gallino, D. Cangialosi, Z. Evenson, L. Schmitt, S. Hechler, M. Stolpe, and B. Ruta, *Hierarchical aging pathways and reversible fragile-to-strong transition upon annealing of a metallic glass former*, Acta Materialia **144**, 400–410 (2018).

[57] F. Zhu, H. K. Nguyen, S. X. Song, D. P. B. Aji, A. Hirata, H. Wang, K. Nakajima, and M. W. Chen, *Intrinsic correlation between beta-relaxation and spatial heterogeneity in a metallic glass*, Nature Communications **7**, 11516 (2016).

[58] D.J. Magagnosc, G. Kumar, J. Schroers, P. Felfer, J.M. Cairney, and D.S. Gianola, *Effect of ion irradiation on tensile ductility, strength and fictive temperature in metallic glass nanowires*, Acta Materialia **74**, 165–182 (2014).

[59] A. L. Greer and Y. H. Sun, *Stored energy in metallic glasses due to strains within the elastic limit*, Philosophical Magazine **96**, 1643–1663 (2016).

[60] J. Saida, R. Yamada, M. Wakeda, and S. Ogata, *Thermal rejuvenation in metallic glasses*, Science and Technology of Advanced Materials **18**, 152–162 (2017).

[61] F. O. Méar, B. Doisneau, A. R. Yavari, and A. L. Greer, *Structural effects of shot-peening in bulk metallic glasses*, Journal of Alloys and Compounds **483**, 256–259 (2009).

[62] W. Dmowski, Y. Yokoyama, A. Chuang, Y. Ren, M. Umemoto, K. Tsuchiya, A. Inoue, and T. Egami, *Structural rejuvenation in a bulk metallic glass induced by severe plastic deformation*, Acta Materialia **58**, 429–438 (2010).

[63] R. T. Ott, M. Heggen, M. Feuerbacher, E. S. Park, D. H. Kim, M. J. Kramer, M. F. Besser, and D. J. Sordelet, *Anelastic strain and structural anisotropy in homogeneously deformed $Cu_{64.5}Zr_{35.5}$ metallic glass*, Acta Materialia **56**, 5575–5583 (2008).

[64] T. C. Hufnagel, C. A. Schuh, and M. L. Falk, *Deformation of metallic glasses: Recent developments in theory, simulations, and experiments*, Acta Materialia **109**, 375–393 (2016).

[65] A. S. Argon, *Plastic deformation in metallic glasses*, Acta Metallurgica **27**, 47–58 (1979).

[66] M. L. Falk and J. S. Langer, *Dynamics of viscoplastic deformation in amorphous solids*, Physical Review E **57**, 7192–7205 (1998).

[67] F. Albano and M. L. Falk, *Shear softening and structure in a simulated three-dimensional binary glass*, The Journal of Chemical Physics **122**, 154508 (2005).

[68] S. G. Mayr, *Activation energy of shear transformation zones: A key for understanding rheology of glasses and liquids*, Physical Review Letters **97**, 195501 (2006).

[69] D. Rodney and C. Schuh, *Distribution of thermally activated plastic events in a flowing glass*, Physical Review Letters **102**, 235503 (2009).

[70] D. Klaumünzer, R. Maaß, and J. F. Löffler, *Stick-slip dynamics and recent insights into shear banding in metallic glasses*, Journal of Materials Research **26**, 1453–1463 (2011).

[71] A. L. Greer, Y. Q. Cheng, and E. Ma, *Shear bands in metallic glasses*, Materials Science and Engineering Reports **74**, 71–132 (2013).

[72] J. H. Perepezko, S. D. Imhoff, M.-W. Chen, J.-Q. Wang, and S. Gonzalez, *Nucleation of shear bands in amorphous alloys*, Proceedings of the National Academy of Sciences **111**, 3938–3942 (2014).

[73] W. L. Johnson and K. Samwer, *A universal criterion for plastic yielding of metallic glasses with a* $(T/T_g)^{2/3}$ *temperature dependence*, Physical Review Letters **95**, 195501 (2005).

[74] D. Şopu, A. Stukowski, M. Stoica, and S. Scudino, *Atomic-level processes of shear band nucleation in metallic glasses*, Physical Review Letters **119**, 195503 (2017).

[75] H.-B. Yu, W.-H. Wang, H. Y. Bai, Y. Wu, and M. W. Chen, *Relating activation of shear transformation zones to β-relaxations in metallic glasses*, Physical Review B **81**, 220201(R) (2010).

[76] D. B. Miracle, *A structural model for metallic glasses*, Nature **10**, 786–787 (2004).

[77] H. W. Sheng, E. Ma, H. Z. Liu, and J. Wen, *Pressure tunes atomic packing in metallic glass*, Applied Physics Letters **88**, 171906 (2006).

[78] Y. Q. Cheng, A. J. Cao, H. W. Sheng, and E. Ma, *Local order influences initiation of plastic flow in metallic glass: Effects of alloy composition and sample cooling history*, Acta Materialia **56**, 5263–5275 (2008).

[79] Y. Zhang, C. Z. Wang, M. I. Mendelev, F. Zhang, M. J. Kramer, and K. M. Ho, *Diffusion in a Cu-Zr metallic glass studied by microsecond-scale molecular dynamics simulations*, Physical Review B **91**, 180201(R) (2015).

[80] J. Ding, M. Asta, and R. O. Ritchie, *Anomalous structure-property relationships in metallic glasses through pressure-mediated glass formation*, Physical Review B **93**, 140204(R) (2016).

[81] J. Ding, Y.-Q. Cheng, H. Sheng, M. Asta, R. O. Ritchie, and E. Ma, *Universal structural parameter to quantitatively predict metallic glass properties*, Nature Communications **7**, 13733 (2016).

[82] S. Pauly, S. Gorantla, G. Wang, U. Kuehn, and J. Eckert, *Transformation-mediated ductility in CuZr-based bulk metallic glasses*, Nature Materials **9**, 473–477 (2010).

[83] K. Albe, Y. Ritter, and D. Şopu, *Enhancing the plasticity of metallic glasses: Shear band formation, nanocomposites and nanoglasses investigated by molecular dynamics simulations*, Mechanics of Materials **67**, 94–103 (2013).

[84] S.-W. Lee, M.-Y. Huh, E. Fleury, and J.-C. Lee, *Crystallization-induced plasticity of Cu–Zr containing bulk amorphous alloys*, Acta Materialia **54**, 349–355 (2006).

[85] G. Wu, K.-C. Chan, L.Zhu, L. Sun, and J. Lu, *Dual-phase nanostructuring as a route to high-strength magnesium alloys*, Nature **545**, 80–83 (2017).

[86] J. Jing, A. Krämer, R. Birringer, H. Gleiter, and U. Gonser, *Modified atomic structure in a Pd-Fe-Si nanoglass*, Journal of Non-Crystalline Solids **113**, 167 – 170 (1989).

[87] H. Gleiter, *Nanocrystalline solids*, Journal of Applied Crystallography **24**, 79–90 (1991).

[88] J. Weissmüller, R. Birringer, and H. Gleiter, *Nanostructured crystalline and amorphous solids*, Key Engineering Materials **77-78**, 161–170 (1992).

[89] O. Franke, D. Leisen, H. Gleiter, and H. Hahn, *Thermal and plastic behavior of nanoglasses*, Journal of Materials Research **29**, 1210–1216 (2014).

[90] J. X. Fang, U. Vainio, W. Puff, R. Würschum, X. L. Wang, D. Wang, M. Ghafari, F. Jiang, J. Sun, H. Hahn, and H. Gleiter, *Atomic structure and structural stability of $Sc_{75}Fe_{25}$ nanoglasses*, Nano Letters **12**, 458–463 (2012).

[91] N. Chen, R. Frank, N. Asao, D. V. Louzguine-Luzgin, P. Sharma, J. Q. Wang, G. Q. Xie, Y. Ishikawa, N. Hatakeyama, Y. C. Lin, M. Esashi, Y. Yamamoto, and A. Inoue, *Formation and properties of Au-based nanograined metallic glasses*, Acta Materialia **59**, 6433–6440 (2011).

[92] M. Ghafari, H. Hahn, R. A. Brand, R. Mattheis, Y. Yoda, S. Kohara, R. Kruk, and S. Kamali, *Structure of iron nanolayers embedded in amorphous alloys*, Applied Physics Letters **100**, 203108 (2012).

[93] T. Brink, D. Şopu, and K. Albe, *Solid-state amorphization of Cu nanolayers embedded in a $Cu_{64}Zr_{36}$ glass*, Physical Review B **91**, 184103 (2015).

[94] D. Şopu, Y. Ritter, H. Gleiter, and K. Albe, *Deformation behavior of bulk and nanostructured metallic glasses studied via molecular dynamics simulations*, Physical Review B **83**, 100202 (2011).

[95] O. Adjaoud and K. Albe, *Microstructure formation of metallic nanoglasses: Insights from molecular dynamics simulations*, Acta Materialia **145**, 322–330 (2018).

[96] D. Şopu and K. Albe, *Influence of grain size and composition, topology and excess free volume on the deformation behavior of Cu–Zr nanoglasses*, Beilstein Journal of Nanotechnology **6**, 537–545 (2015).

[97] S. Adibi, P. S. Branicio, and S. P. Joshi, *Suppression of shear banding and transition to necking and homogeneous flow in nanoglass nanopillars*, Scientific Reports **5**, 15611 (2015).

[98] O. Adjaoud and K. Albe, *Interfaces and interphases in nanoglasses: Surface segregation effects and their implications on structural properties*, Acta Materialia **113**, 284–292 (2016).

[99] S. J. Dillon, M. Tang, W. C. Carter, and M. P. Harmer, *Complexion: A new concept for kinetic engineering in materials science*, Acta Materialia **55**, 6208 – 6218 (2007).

[100] S. J. Dillon, M. P. Harmer, and J. Luo, *Grain boundary complexions in ceramics and metals: An overview*, JOM Journal of the Minerals Metals and Materials Society **61**, 38–44 (2009).

[101] X. Shi and J. Luo, *Developing grain boundary diagrams as a materials science tool: A case study of nickel-doped molybdenum*, Physical Review B **84**, 014105 (2011).

[102] P. R. Cantwell, M. Tang, S. J. Dillon, J. Luo, G. S. Rohrer, and M. P. Harmer, *Grain boundary complexions*, Acta Materialia **62**, 1 –48 (2014).

[103] T. J. Rupert, *The role of complexions in metallic nano-grain stability and deformation*, Current Opinion in Solid State and Materials Science **20**, 257–267 (2016).

[104] S. Takeuchi and A. S. Argon, *Steady-state creep of single-phase crystalline matter at high temperature*, Journal of Materials Science **11**, 1542–1566 (1976).

[105] O. D. Sherby and P. M. Burke, *Mechanical behavior of crystalline solids at elevated temperature*, Progress in Materials Science **13**, 323–390 (1968).

[106] A. Orlová and J. Čadek, *Dislocation structure in the high temperature creep of metals and solid solution alloys: A review*, Materials Science and Engineering **77**, 1–18 (1986).

[107] M. E. Kassner and M.-T. Pérez-Prado, *Five-power-law creep in single phase metals and alloys*, Progress in Materials Science **45**, 1–102 (2000).

[108] M. E. Kassner and M.-T. Perez-Prado, *Fundamentals of creep in metals and alloys*, Elsevier Science, 2004.

[109] H. J. Frost and M. F. Ashby, *Deformation-mechanism maps: The plasticity and creep of metals and ceramics*, Pergamon Press, 1982.

[110] F. R. N. Nabarro, *Report of a conference on the strength of solids*, Physical Society, London, 1948, p. 75.

[111] C. Herring, *Diffusional viscosity of a polycrystalline solid*, Journal of Applied Physics **21**, 437–445 (1950).

[112] R. L. Coble, *A model for boundary diffusion controlled creep in polycrystalline materials*, Journal of Applied Physics **34**, 1679–1682 (1963).

[113] V. Borisov, V. Golikov, and G. Scherbedinskiy, , Physics of Metals and Metallography **17**, 80 (1964).

[114] D. Gupta, *Influence of solute segregation on grain-boundary energy and self-diffusion*, Metallurgical Transactions A, 1431–1438 (1977).

[115] S.-C. Lee, C.-M. Lee, J.-C. Lee, H.-J. Kim, Y. Shibutani, E. Fleury, and M. L. Falk, *Structural disordering process of an amorphous alloy driven by the elastostatic compression at room temperature*, Applied Physics Letters **92**, 151906 (2008).

[116] B. Zhang, R. J. Wang, D. Q. Zhao, M. X. Pan, and W. H. Wang, *Properties of Ce-based bulk metallic glass-forming alloys*, Physical Review B **70**, 224208 (2004).

[117] J. C. Gibeling and W. D. Nix, *A study of the creep properties of a Ni–Fe metallic glass.*, Scripta Metallurgica **12**, 919–926 (1978).

[118] J. P. Patterson and D. R. H. Jones, *Creep of amorphous $Fe_{40}Ni_{40}P_{14}B_6$*, Acta Metallurgica **28**, 675–681 (1980).

[119] V. Ocelik, Yu. V. Fursova, V. A. Khonik, and K. Csach, *Non-newtonian deformation of Co-based metallic glass at low stresses*, Physics of the Solid State **42**, 697–700 (2000).

[120] B.-G. Yoo, J.-H. Oh, Y.-J. Kim, K.-W. Park, J.-C. Lee, and J. Jang, *Nanoindentation analysis of time-dependent deformation in as-cast and annealed Cu-Zr bulk metallic glass*, Intermetallics **18**, 1898–1901 (2010).

[121] B.-G. Yoo, K.-S. Kim, J.-H. Oh, U. Ramamurty, and J.-I. Jang, *Room temperature creep in amorphous alloys: Influence of initial strain and free volume*, Scripta Materialia **63**, 1205–1208 (2010).

[122] W. H. Li, K. Shin, C. G. Lee, B. C. Wei, T. H. Zhang, and Y. Z. He, *The characterization of creep and time-dependent properties of bulk metallic glasses using nanoindentation*, Materials Science and Engineering A **478**, 371–375 (2008).

[123] Y. J. Huang, J. Shen, Y. L. Chiu, J. J. J. Chen, and J. F. Sun, *Indentation creep of an Fe-based bulk metallic glass*, Intermetallics **17**, 190–194 (2009).

[124] M. Heggen, F. Spaepen, and M. Feuerbacher, *Creation and annihilation of free volume during homogeneous flow of a metallic glass*, Journal of Applied Physics **97**, 033506 (2005).

[125] F. Li, Y. Xie, M. Song, S. Ni, S. Guo, and X. Liao, *A detailed appraisal of the stress exponent used for characterizing creep behavior in metallic glasses*, Materials Science and Engineering A **654**, 53–59 (2016).

[126] A. S. Argon and L. T. Shi, *Development of visco-plastic deformation in metallic glasses*, Acta Metallurgica **31**, 499–507 (1983).

[127] S. X. Song, Y. H. Lai, J. C. Huang, and T. G. Nieh, *Homogeneous deformation of Au-based metallic glass micropillars in compression at elevated temperatures*, Applied Physics Letters **94**, 061911 (2009).

[128] J. M. Hutchinson, *Physical aging of polymers*, Progress in Polymer Science **20**, 703–760 (1995).

[129] T. Rouxel, G.-D. Soraru, and J. Vicens, *Creep viscosity and stress relaxation of gel-derived silicon oxycarbide glasses*, Journal of the American Ceramic Society **84**, 1052–1058 (2001).

[130] B. Papendorf, E. Ionescu, H.-J. Kleebe, C. Linck, O. Guillon, K. Nonnenmacher, and R. Riedel, *High-temperature creep behavior of dense SiOC-based ceramic nanocomposites: Microstructural and phase composition effects*, Journal of the American Ceramic Society **96**, 272–280 (2012).

[131] E. Ionescu, C. Balan, H.-J. Kleebe, M. M. Müller, O. Guillon, D. Schliephake, M. Heilmaier, and R. Riedel, *High-temperature creep behavior of SiOC glass-ceramics: Influence of network carbon versus segregated carbon*, Journal of the American Ceramic Society **97**, 3935–3942 (2014).

[132] A. Saha, R. Raj, and D. L. Williamson, *A model for the nanodomains in polymer-derived SiCO*, J. Am. Ceram. Soc. **89**, 2188–2195 (2006).

[133] M. L. Lee, Y. Li, and C. A. Schuh, *Effect of a controlled volume fraction of dendritic phases on tensile and compressive ductility in La-based metallic glass matrix composites*, Acta Materialia **52**, 4121–4131 (2004).

[134] X. L. Fu, Y. Li, and C. A. Schuh, *Temperature, strain rate and reinforcement volume fraction dependence of plastic deformation in metallic glass matrix composites*, Acta Materialia **55**, 3059–3071 (2007).

[135] J. Eckert, A. Kübler, and L. Schultz, *Mechanically alloyed $Zr_{55}Al_{10}Cu_{30}Ni_5$ metallic glass composites containing nanocrystalline W particles*, Journal of Applied Physics **85**, 7112–7119 (1999).

[136] S. H. Hong, J. T. Kim, S. C. Mun, Y. S. Kim, H. J. Park, Y. S. Na, K. R. Lim, J. M. Park, and K. B. Kim, *Influence of spherical particles and interfacial stress distribution on viscous flow behavior of Ti-Cu-Ni-Zr-Sn bulk metallic glass composites*, Intermetallics **91**, 90–94 (2017).

[137] M. P. Allen and D. J. Tildesley, *Computer simulation of liquids*, Oxford Science Publications, Clarendon Press, 1989.

[138] D. Frenkel and B. Smit, *Understanding molecular simulation: From algorithms to applications*, Computational Science Series, Academic Press, 2001.

[139] S. Plimpton, *Fast parallel algorithms for short-range molecular dynamics*, Journal of Computational Physics **117**, 1–19 (1995).

[140] P. Hohenberg and W. Kohn, *Inhomogeneous electron gas*, Physical Review **136**, B864–871 (1964).

[141] W. Kohn and L. J. Sham, *Self-consistent equations including exchange and correlation effects*, Physical Review A **140**, 1133–1138 (1965).

[142] P. M. Morse, *Diatomic molecules according to the wave mechanics. II. Vibrational levels*, Physical Review **34**, 57–64 (1929).

[143] M. S. Daw and M. I. Baskes, *Embedded-atom method: Derivation and application to impurities, surfaces, and other defects in metals*, Physical Review B **29**, 6443–6453 (1984).

[144] M. W. Finnis and J. E. Sinclair, *A simple empirical N-body potential for transition metals*, Philosophical Magazine A **50**, 45–55 (1984).

[145] T. Germann and K. Kadau, *Trillion-atom molecular dynamics becomes a reality*, International Journal of Modern Physics C **19**, 1315–1319 (2008).

[146] W. Shinoda, M. Shiga, and M. Mikami, *Rapid estimation of elastic constants by molecular dynamics simulation under constant stress*, Physical Review B **69**, 134103 (2004).

[147] E. Polak and G. Ribière, *Note sur la convergence de méthodes de directions conjugués*, Revue française d'informatique et de recherche opérationnelle. Série rouge **3**, 35–43 (1969).

[148] A. Stukowski, *Visualization and analysis of atomistic simulation data with OVITO-The Open Visualization Tool*, Modelling and Simul.ation in Materials Science and Engineering **18**, 015012 (2010).

[149] B.-N. Dinh Ngô, A. Stukowski, N. Mameka, J. Markmann, K. Albe, and J. Weissmüller, *Anomalous compliance and early yielding of nanoporous gold*, Acta Materialia **93**, 144–155 (2015).

[150] D. P. Landau and K. Binder, *A guide to Monte Carlo simulations in statistical physics*, Cambridge University Press, 2000.

[151] *Crossing the mesoscale no-man's land via parallel kinetic Monte Carlo*, Sand2009-6226, Sandia report, oct 2009.

[152] M. A. Gibson and J. Bruck, *Efficient exact stochastic simulation of chemical systems with many species and many channels*, The Journal of Physical Chemistry A **104**, 1876–1889 (2000).

[153] J. Zemp, M. Celino, B. Schönfeld, and J. F. Löffler, *Icosahedral superclusters in $Cu_{64}Zr_{36}$ metallic glass*, Physical Review B **90**, 144108 (2014).

[154] J. Zemp, M. Celino, B. Schönfeld, and J. F. Löffler, *Crystal-like rearrangements of icosahedra in simulated copper–zirconium metallic glasses and their effect on mechanical properties*, Physical Review Letters **115**, 165501 (2015).

[155] D. Arias and J. P. Abriata, *Cu-Zr (copper–zirconium)*, Journal of Phase Equilibria **11**, 452–459 (1990).

[156] N. Wang, C. Li, Z. Du, F. Wang, and W. Zhang, *The thermodynamic reassessment of the Cu–Zr system*, Calphad **30**, 461–469 (2006).

[157] C. Tang and P. Harrowell, *Predicting the solid state phase diagram for glass-forming alloys of copper and zirconium*, Journal of Physics: Condensed Matter **24**, 245102 (2012).

[158] C. C. Hays, C. P. Kim, and W. L. Johnson, *Large supercooled liquid region and phase separation in the Zr-Ti-Ni-Cu-Be bulk metallic glasses*, Applied Physics Letters **75**, 1089–1091 (1999).

[159] J. D. Honeycutt and H. C. Andersen, *Molecular dynamics study of melting and freezing of small Lennard-Jones clusters*, The Journal of Physical Chemistry **91**, 4950–4963 (1987).

[160] A. Stukowski, *Structure identification methods for atomistic simulations of crystalline materials*, Modelling and Simulation in Materials Science and Engineering **20**, 045021 (2012).

[161] F. Shimizu, S. Ogata, and J. Li, *Theory of shear banding in metallic glasses and molecular dynamics calculations*, Materials Transcations **48**, 2923–2927 (2007).

[162] H. Edelsbrunner and E. P. Mücke, *Three-dimensional alpha shapes*, ACM Transactions on Graphics **13**, 43–72 (1994).

[163] A. Stukowski, *Computational analysis methods in atomistic modeling of crystals*, JOM Journal of the Minerals Metals and Materials Society **66**, 399–407 (2014).

[164] G. Taubin, *A signal processing approach to fair surface design*, Proceedings of the 22nd Annual Conference on Computer Graphics and Interactive Techniques, SIGGRAPH '95, 1995, pp. 351–358.

[165] A. S. Argon and H. Y. Kuo, *Free-energy spectra for inelastic deformation of five metallic-glass alloys*, Journal of Non-Crystalline Solids **37**, 241–266 (1980).

[166] M. E. Kassner, K. Smith, and V. Eliasson, *Creep in amorphous metals*, Journal of Materials Research and Technogloy **4**, 100–107 (2015).

[167] Y. Fan, T. Iwashita, and T. Egami, *Energy landscape-driven non-equilibrium evolution of inherent structure in disordered material*, Nature Communications **8**, 15417 (2017).

[168] T. Brink and K. Albe, *From metallic glasses to nanocrystals: Molecular dynamics simulations on the crossover from glass-like to grain-boundary-mediated deformation behaviour*, Acta Materialia **156**, 205–214 (2018).

[169] Y. Q. Cheng, A. J. Cao, and E. Ma, *Correlation between the elastic modulus and the intrinsic plastic behavior of metallic glasses: The roles of atomic configuration and alloy composition*, Acta Materialia **57**, 3253–3267 (2009).

[170] Y. Q. Cheng and E. Ma, *Intrinsic shear strength of metallic glass*, Acta Materialia **59**, 1800–1807 (2011).

[171] K.-W. Park, C.-M. Lee, J. Wakeda, Y. Shibutani, M. L. Falk, and J.-C. Lee, *Elastostatically induced structural disordering in amorphous alloys*, Acta Materialia **56**, 5440–5450 (2008).

[172] H. B. Ke, P. Wen, H. L. Peng, W. H. Wang, and A. L. Greer, *Homogeneous deformation of metallic glass at room temperature reveals large dilatation*, Scripta Materialia **64**, 966–969 (2011).

[173] F. Wang, J. M. Li, P. Huang, W. L. Wang, T. J. Lu, and K. W. Xu, *Nanoscale creep deformation in Zr-based metallic glass*, Intermetallics **38**, 156–160 (2013).

[174] Y. Suzuki, J. Haimovich, and T. Egami, *Bond-orientational anisotropy in metallic glasses observed by X-ray diffraction*, Physical Review B **35**, 2162–2168 (1987).

[175] W. Dmowski and T. Egami, *Observation of structural anisotropy in metallic glasses induced by mechanical deformation*, Journal of Materials Research **22**, 412–418 (2007).

[176] Y. Yu, M. Wang, D. Zhang, B. Wang, G. Sant, and M. Bauchy, *Stretched exponential relaxation of glasses at low temperature*, Physical Review Letters **115**, 165901 (2015).

[177] C. Kalcher, T. Brink, J. Rohrer, A. Stukowski, and K. Albe, *Interface-controlled creep in metallic glass composites*, Acta Materialia **141**, 251 – 260 (2017).

[178] D. C. Hofmann, J.-Y. Suh, A. Wiest, G. Duan, M.-L. Lind, M. D. Demetriou, and W. L. Johnson, *Designing metallic glass matrix composites with high toughness and tensile ductility*, Nature **451**, 1085 (2008).

[179] F. Jiang, Z. B. Zhang, L. He, J. Sun, H. Zhang, and Z. F. Zhang, *The effect of primary crystallizing phases on mechanical properties of $Cu_{46}Zr_{47}Al_7$ bulk metallic glass composites*, Journal of Materials Research **21**, 2638–2645 (2006).

[180] F. Jiang, D. H. Zhang, L. C. Zhang, Z. B. Zhang, L. He, J. Sun, and Z. F. Zhang, *Microstructure evolution and mechanical properties of $Cu_{46}Zr_{47}Al_7$ bulk metallic glass composite containing CuZr crystallizing phases*, Materials Science and Engineering A **467**, 139–145 (2007).

[181] S. Pauly, J. Das, C. Duhamel, and J. Eckert, *Martensite formation in a ductile $Cu_{47.5}Zr_{47.5}Al_5$ bulk metallic glass composite*, Advanced Engineering Materials **9**, 487–491 (2007).

[182] S. Pauly, J. Das, J. Bednarcik, N. Mattern, K. B. Kim, D. H. Kim, and J. Eckert, *Deformation-induced martensitic transformation in Cu–Zr–(Al,Ti) bulk metallic glass composites*, Scripta Materialia **60**, 431–434 (2009).

[183] E. Ma, *Tuning order in disorder*, Nature Materials **14**, 547–552 (2015).

[184] S. Pauly, G. Liu, S. Gorantla, G. Wang, U. Kühn, D. H. Kim, and J. Eckert, *Criteria for tensile plasticity in Cu–Zr–Al bulk metallic glasses*, Acta Materialia **58**, 4883–4890 (2010).

[185] P. M. Derlet, R. Maaß, and J. F. Löffler, *The boson peak of model glass systems and its relation to atomic structure*, The European Physical Journal B **85**, 148 (2012).

[186] J. Schäfer, Y. Ashkenazy, K. Albe, and R. S. Averback, *Effect of solute segregation on thermal creep in dilute nanocyrstalline Cu alloys*, Materials Science and Engineering: A **546**, 307–313 (2012).

[187] Y. Ashkenazy and R. S. Averback, *Irradiation induced grain boundary flow–A new creep mechanism at the nanoscale*, Nano Letters, 4084–4089 (2012).

[188] C. Kalcher, O. Adjaoud, J. Rohrer, A. Stukowski, and K. Albe, *Reinforcement of nanoglasses by interface strengthening*, Scripta Materialia **141**, 115–119 (2017).

[189] C. Stabler, F. Roth, M. Narisawa, D. Schliephake, M. Heilmaier, S. Lauterbach, H.-J. Kleebe, R. Riedel, and E. Ionescu, *High-temperature creep behavior of a SiOC glass ceramic free of segregated carbon*, Journal of the European Ceramic Society **36**, 3747–3753 (2016).

[190] C. Stabler, D. Schliephake, M. Heilmaier, T. Rouxel, H.-J. Kleebe, M. Narisawa, R. Riedel, and E. Ionescu, *Influence of SiC/silica and carbon/silica interfaces on the high-temperature creep of silicon oxycarbide-based glass ceramics: A case study*, Advanced Engineering Materials, 1800596 (2018).